Eruptive Rates and Volatile Emissions of the Deccan Large Igneous Province and Environmental Consequences

by

Isabel Fendley

A dissertation submitted in partial satisfaction of the

requirements for the degree of

Doctor of Philosophy

in

Earth and Planetary Science

in the

Graduate Division

of the

University of California, Berkeley

Committee in charge:

Professor Paul R. Renne, Chair
Professor Stephen S. Self
Professor Seth Finnegan

Summer 2020

Abstract

Eruptive Rates and Volatile Emissions of the Deccan Large Igneous Province and Environmental Consequences

by

Isabel Fendley

Doctor of Philosophy in Earth and Planetary Science

University of California, Berkeley

Professor Paul R. Renne, Chair

The end-Cretaceous mass extinction resulted in the demise of the dinosaurs and many other plant and animal species, irrevocably changing Earth's ecosystems. The environmental changes which influenced the mass extinction and recovery were most likely caused by a combination of the Chicxulub impact and Deccan Traps Large Igneous Province volcanism. The climate and ecological effects of the Deccan Traps remain ambiguous, due in part to a paucity of constraints on eruption rates and frequency. I have addressed this by using mercury concentration as an indicator of eruptions and combining these chemostratigraphic records with mercury box models to estimate eruptive rate and emissions rate of climate-altering gases. Additionally, the timing of the largest known Deccan eruptions, the Rajahmundry Traps, was unclear with respect to the extinction event. As the largest eruptions have been hypothesized to have the most significant climate impact, knowing the timing of these eruptions allows for direct comparison with climate records. Using a combination of geochronological techniques, I found that all three subaerially exposed Rajahmundry Traps lava flows erupted after the Cretaceous-Paleogene boundary. I then used scalings from the LOSCAR carbon cycle model along with paleoclimate records and found that these eruptions most likely did not cause multi-degree warming. However, they could have contributed to ongoing carbon cycle perturbations during the recovery interval. I then investigated the nature of these carbon cycle perturbations by creating a new high-resolution carbon isotope record from terrestrial organic material. I specifically addressed the discrepancy between terrestrial carbon isotope records, which have been interpreted as containing short ($<$10 ka) excursions, and marine records, which contain a much longer ($\sim$ 1.5 Ma) excursion linked to decreased export productivity in the surface ocean. My new record shows that, contrary to previously thought, terrestrial records also show a long duration excursion during this time interval. However, while the duration of the excursions is now known to be similar between terrestrial and marine realms, the shape of the excursion is different. The different trends indicate that the open ocean DIC pool and marine CO_2 were possibly in disequilibrium during parts of the recovery interval.

Contents

Acknowledgments

I would like to thank Prof. Paul Renne for supervision, ideas, and support. I strongly appreciate him providing me the freedom to explore my interests and work on a variety of topics in addition to my primary thesis work. Thanks also to Courtney Sprain, Elizabeth Niespolo, and Andy Tholt for significant help and support. Thanks to the faculty, staff, postdocs, PhD students, and undergraduates at UC Berkeley and everyone at the Berkeley Geochronology Center. Thanks to the many people who helped with field work in Montana and India. Finally, thanks to my family and Tushar for many discussions and constant support.

Chapter 1

Introduction

The Cretaceous-Paleogene (K-Pg) mass extinction witnessed the extinction of non-avian dinosaurs and many other species, which significantly altered ecosystems around the world. The K-Pg extinction is the most recent mass extinction, leading to a greater understanding of environmental conditions and biodiversity than for any other mass extinction. The exact cause of the environmental and ecological changes is unclear, as two catastrophic events could have influenced the extinction and recovery intervals.

The Chicxulub bolide impact occurred ca. 66.052 Ma, approximately simultaneous with the K-Pg extinction in the marine environment. At the same time, the majority of the Deccan Traps large igneous province erupted over a $\sim$ 1 Ma period spanning the extinction. The impact generated a layer of debris, known as the impact claystone, within which there is an elevated concentration of the element iridium. This layer is a world-wide marker bed that enables direct temporal comparison between the Chicxulub impact and environmental and ecological events recorded in sedimentary records. On the other hand, there are no such markers of Deccan Traps activity, so it is more difficult to understand the relationship between the volcanic eruptions and the environmental changes.

Both these events had the potential to alter the environment and ecosystems significantly. The Chicxulub bolide impact likely ejected rock dust and soot high into the atmosphere, blocking out light. This "impact winter" has been linked to ocean acidification, global cooling, and the sudden extinction of many species of marine nannoplankton. On the other hand, the Deccan Traps erupted $\sim$ 1 million km^3 of basaltic lava and emitted large quantities of climate-altering gases such as sulfur dioxide (SO_2, leads to sulfate aerosol cooling) and carbon dioxide (CO_2, greenhouse warming). The climate effects of these gases occur on different timescales and may be directly related to the eruptive flux. Deccan CO_2 emissions have been tentatively linked to a warming event in the late Maastrichtian, as well as more gradual warming through the first half million years of the Paleocene.

In this thesis, I address the role of the Deccan Traps in the Cretaceous-Paleogene extinction and recovery. In particular, I investigate the potential of Deccan Traps eruptions to have caused climate or other environmental change, and assess the dynamics of these changes.

In Chapter 1, I examine the eruptive rate and duration of Deccan eruptions close to the Cretaceous-Paleogene boundary. At the scale of individual eruptions, the eruption rate deter-

mines whether eruptive emission of SO_2 is sufficient to cause global cooling. Additionally, the frequency and duration of eruptions controlled how often these colder periods would have occurred and how long they lasted. I use mercury concentration records to estimate these parameters for Deccan eruptions within $\sim$ 100 ka of the Cretaceous-Paleogene boundary, and discuss the implications for climate perturbations during this critical interval.

In Chapter 2, I determine the timing of the Rajahmundry Traps eruptions, potentially the most voluminous Deccan eruptions. These eruptions may have correlated with higher rates of both eruptive and non-eruptive volatile emissions. However, previous age constraints on the Rajahmundry eruptions were not sufficient to clarify their timing with respect to the Cretaceous-Paleogene boundary. I use a variety of geochronological techniques to determine the eruption timing, and then I use a carbon cycle model to evaluate whether the Rajahmundry eruptions could have caused significant global climate change.

In Chapter 3, I investigate the global carbon cycle perturbation after the extinction, and determine the duration and timing of the carbon isotope excursion in terrestrial records. Records from terrestrial and marine environments disagree on the duration of the carbon isotope excursion: most marine records suggest a long (100s of ka) excursion, correlated by a decrease in export productivity, while terrestrial records indicate a very brief ($\leq$ 10 ka) excursion. I create a new terrestrial carbon isotope record and evaluate the relationship between terrestrial and marine records, and discuss implications for atmospheric carbon isotope composition and overall carbon cycle dynamics.

Chapter 2

Constraints on the volume and rate of Deccan Traps flood basalt eruptions using a combination of high-resolution terrestrial mercury records and geochemical box models

2.1 Introduction

The end of the Cretaceous Period was a time of profound environmental change, which culminated in the extinction of all non-avian dinosaurs among many other organisms (e.g., Schulte et al., 2010). Two catastrophic events were coeval with the extinction – the Chicxulub bolide impact and Deccan Traps continental flood basalt eruptions (e.g., Renne et al., 2013). Both the impact and the Deccan eruptions had the potential to cause global climate change, releasing thousands of Tg of climatically active gases such as sulfur dioxide (SO_2, leads to sulfate aerosol driven cooling) and carbon dioxide (CO_2, greenhouse warming) (e.g., Self, Widdowson, Thordarson, & Jay, 2006).

The climate effects of these gases occur on different timescales and are directly related to the eruptive flux, neglecting the contributions of volatiles emitted during quiescent intervals (e.g., Black et al., 2018; Self, Schmidt, & Mather, 2014). Deccan eruptive events are hypothesized to have emitted enough SO_2 to cause significant and rapid global cooling, whereby the duration of the cold interval is proportional to the duration of the eruption, as SO_2's lifetime in the atmosphere is short: weeks in the troposphere, a few years in the stratosphere (e.g., Schmidt et al., 2016). In contrast, carbon cycle models indicate that CO_2 pulses persist for thousands of years in the atmosphere (e.g., Zeebe, 2012). Consequently, CO_2 may accumulate through multiple eruptive events and lead to greenhouse warming on longer timescales (e.g., Archer et al., 2009; Self et al., 2006; Tobin, Bitz, & Archer, 2016). The extent of these climate effects depends on both the quantity and rate at which volcanogenic CO_2 and SO_2 is released, as well as the length of hiatuses between eruptions (Black et

al., 2018). Therefore in order to determine the climatic effects of Deccan volcanism, it is necessary to understand the eruptive rate at a resolution comparable to individual eruptions (Self et al., 2014). While the main Deccan eruptive sequence lasted for approximately a million years, active eruptions potentially occurred only a few percent of the time (Self et al., 2014). Dates of Deccan basalts place the Cretaceous-Paleogene boundary near the beginning of the most voluminous eruptive interval, the Wai subgroup (Schoene et al., 2019; Sprain et al., 2019). The current maximum level of precision for any radioisotopic dating technique on Cretaceous-age basalt is tens of thousands of years; however, individual eruptive events for flood basalts have been hypothesized to be ten to hundreds of years in duration based on physical and petrologic properties of lava flows (Self et al., 2006; Thordarson & Self, 1996). Consequently, while radioisotopic dates are an essential tool in determining cumulative eruptive rates throughout the entire Deccan sequence, they cannot presently provide sub-ten thousand year eruptive records as required.

Mercury is used as a tracer of flood basalt eruptions, as volcanogenic mercury is deposited into sediments geologically rapidly (Percival et al., 2015; Sanei, Grasby, & Beauchamp, 2012). Volcanism is a major natural source of mercury to the environment, and it is recycled through different environmental reservoirs (e.g., Fitzgerald & Lamborg, 2014). The residence time for gaseous mercury is $\sim$9 months in the atmosphere, which is long enough to be distributed globally, though not necessarily homogeneously (Chen et al., 2018). Atmospheric mercury gas can be oxidized, dissolved into water vapor and rained out, or directly taken up by biota. Aqueous or biotic mercury on continents frequently accumulates in rivers and lakes, and a significant fraction is adsorbed onto sediment or particulate material (e.g., Driscoll et al., 2007). Mercury in continental waterways either reaches the ocean or is buried in fluvial or lacustrine sediment. In sediment, the mercury may be associated with organic carbon or sulfur, and it is important to consider interactions with these species. Models indicate that although the time between the emission of gaseous mercury and final burial in sediment ranges from almost immediate to several thousand years, the majority is buried within a thousand years (Amos et al., 2014).

The abundance of sedimentary mercury has previously been used as an indicator of Deccan volcanic eruptions (e.g., Font et al., 2016; Keller et al., 2018; Percival et al., 2018; Sial et al., 2016). However, the interpretation has focused primarily on the presence or absence of mercury concentration peaks at a particular time interval. Most records display increases in mercury concentration in the vicinity of the Cretaceous-Paleogene boundary, indicating a potential increase of the global mercury budget. Comparison of these records from multiple locations indicates variation in peak sizes and timing, possibly due to uncertainty in chronology, sediment accumulation rate (SAR), and lithologic changes (Percival et al., 2018). Well-characterized environmental mercury box models present an opportunity to investigate and compare these records quantitatively, and to estimate the eruptive flux required to produce a mercury concentration peak. Herein we present a high-resolution terrestrial mercury record with precise chronologic constraints to improve understanding of volcanism around the Cretaceous-Paleogene boundary. Then, we describe a model framework for assessing global mercury cycle change indicated by a concentration change in sedimentary records.

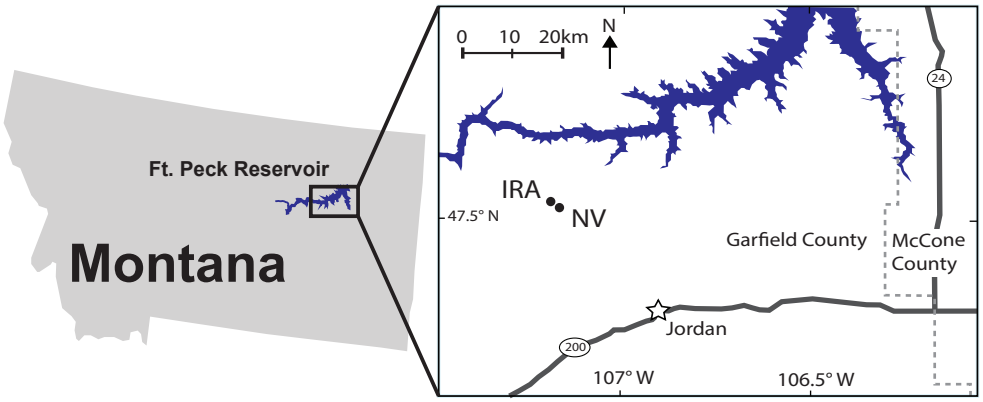

Figure 2.1: Map of the studied localities in eastern Montana, USA. The star indicates the town of Jordan, MT. The Nirvana locality is labeled as NV; Iridium Hill Annex is labeled as IRA.

2.2 Geologic Setting

2.2.1 Hell Creek and Fort Union Formations

This study examines the mercury record around the Cretaceous-Paleogene boundary from two terrestrial sites, Iridium Hill Annex and Nirvana, within the Cretaceous Hell Creek Formation and the Paleogene Tullock Member of the Fort Union Formation in northeastern Montana (Fig. 2.1). These units are composed of fluvial and floodplain deposits, mainly claystones to siltstones, with occasional crossbedded sandstones and lignite seams within the more finely bedded Tullock Member. Rivers transport mercury from continental biomass and sediments to the ocean, dominantly as particulate mercury species (Amos et al., 2014; Cossa, Coquery, Gobeil, & Martin, 1996). Fluvial sediments are therefore likely to increase in mercury concentration following an increase in mercury within proximal soils or biomass. This conclusion is corroborated by an increase in mercury concentrations in modern fluvial sediments due to anthropogenic mercury release (e.g., Amos et al., 2014; Fitzgerald & Lamborg, 2014).

The Hell Creek and Fort Union formations have been extensively studied, and a detailed chronostratigraphy has been established based on radioisotopically dated volcanic tephra layers and magnetostratigraphy (e.g., Fastovsky & Bercovici, 2016; Sprain, Renne, Wilson, & Clemens, 2015; Sprain, Renne, Clemens, & Wilson, 2018). The Cretaceous-Paleogene boundary is recognized here by an impact ejecta claystone and iridium anomaly within the "Iridium Z" coal seam (L. W. Alvarez, 1983), and a tephra layer within a few centimeters of the claystone has been radioisotopically dated in both sites examined in this study with a pooled date of 66.052 Ma (Renne et al., 2013; Sprain et al., 2018). The boundary between the Hell Creek and Fort Union formations is approximately correlated with the Cretaceous-Paleogene boundary (e.g., Fastovsky & Bercovici, 2016).

2.2.2 Site Descriptions

2.2.2.1 Iridium Hill Annex

Iridium Hill Annex (47°31'36.23"N 107°12'36.76"W) is a hill adjacent to the (<100 m) Iridium Hill (L. W. Alvarez, 1983; Swisher III, Dingus, & Butler, 1993) and the (∼200 m) Hauso Flats sites, and in some cases the names have been used interchangeably (Sprain et al., 2015). These sites (Hauso Flats, Iridium Hill, and Iridium Hill Annex) record the same stratigraphy, as evidenced by laterally continuous lithologic units, although Iridium Hill Annex also exposes material of younger age than the other adjacent hills. An iridium anomaly has been recorded within the IrZ coal at the Iridium Hill/Hauso Flats site (L. W. Alvarez, 1983).

Both the HFZ and IrZ coal tephra layers have been dated in multiple locations. For Iridium Hill Annex's age model we utilize pooled dates for both tephra layers (IrZ, 66.052 ± 0.008 Ma, from Sprain et al. (2018) and HFZ, 65.973 ± 0.020 Ma, from Sprain et al. (2015)), and linearly interpolate between them, resulting in a sedimentation rate of 40 years/cm, or 25 cm/ka.

2.2.2.2 Nirvana

Nirvana is ∼1.75 km from Iridium Hill Annex (47°31'37.1"N, 107°11'10.98"W, WGS84). It is a smaller butte with an IrZ coal and tephra layer present, at which we have placed the Cretaceous-Paleogene boundary. The IrZ tephra layer here has been dated (Sprain et al., 2015) and chemically correlated to the tephra layer at Hauso Flats and other IrZ localities in the region (Ickert, Mulcahy, Sprain, Banaszak, & Renne, 2015). The MCZ is another small coal/carbonaceous shale with a tephra layer. Although the tephra layer has not been dated at Nirvana specifically, it has been chemically correlated with other locations where the MCZ has been dated (Ickert et al., 2015). For Nirvana's age model, we linearly interpolate between the IrZ (66.052 ± 0.008 Ma) and MCZ (66.024 ± 0.014 Ma) pooled ages (Sprain et al., 2018), resulting in a sedimentation rate of 68 years/cm, or 14.75 cm/ka.

2.3 Methods

2.3.1 Chemical Analyses

2.3.1.1 Sample Preparation

Samples were collected from trenches exposing visibly unweathered rock, wrapped in aluminum foil and placed into plastic bags. Samples which contained any roots or traces of modern plant/fungal material were not analyzed. Stratigraphic sections were recorded simultaneously with sample collection. Samples were crushed to a fine powder using a ceramic mortar and pestle, then freeze-dried and stored in a desiccator prior to mercury concentration (THg) analysis. An aliquot was retained for organic carbon concentration (TOC) analysis.

We sieved some initial crushed sediment samples at 75 microns (μm), and the < 75 μm and > 75 μm size fractions were analyzed for THg separately. For those samples, the final THg concentration

is a weighted average of the two measurements. Three samples were analyzed both as non-sieved bulk material and as the weighted average of the two size fractions (< 75 μm and > 75 μm), to assess potential differences in these approaches. As both size fractions contained measurable THg, going forward, we analyzed only the bulk (unsieved) powdered sample. The average ($\pm$ standard error) percent deviation in measured THg concentration between these two preparation types was 13% $\pm$ 6.5% (Duplicates spreadsheet). All TOC analyses were done on the bulk, non-sieved, aliquots of samples.

2.3.1.2 THg Analysis

All analyses were performed at the USGS in Menlo Park following standard methods for solid phase samples (Olund, DeWild, Olson, & Tate, 2004). Samples were initially digested at room temperature with aqua regia (3:1, concentrated HCl:HNO_3), then further oxidized by adding 5% bromium monochloride and heated in an oven at 50 °C overnight. Samples were then analyzed with an automated Total Mercury analyzer (Tekran, Model 2600) with cold vapor atomic fluorescence spectrophotometric (CVAFS) detection. Analytical duplicates of homogenized samples yielded a mean ($\pm$ standard error) percent deviation of 2.6% $\pm$ 0.6% (N=12) (Duplicates sheet). Certified reference material (PACS-3, marine sediment, certified value 3.0 μg/g) recoveries were 95.3 $\pm$ 2.5% (mean $\pm$ standard error, N=11).

2.3.1.3 TOC Analysis

Carbonate was removed from a 70 mg sample aliquot through acidification for 24 hours using 3 mL 1M HCl (e.g., Arens, Jahren, & Kendrick, 2014). The samples were then rinsed three times with 5mL MilliQ water, freeze-dried, and packed into tin capsules. They were analyzed for carbon concentration using a CHNOS Elemental Analyzer (Elementar, Hanau, Germany) at the UC Berkeley Center for Stable Isotope Biogeochemistry. The percent calibration was based in the National Institute of Standards and Technology (Gaithersburg, MD, USA) reference materials. The carbon concentrations of two laboratory quality control standards (soil materials with certified low and high organic content from Elemental Microanalysis, Devon, UK) reproduced their accepted values of 1.61% and 9.20% respectively to 3.7 $\pm$ 1.4% (mean $\pm$ standard error, N=7). Duplicates of samples, acidified separately, had a mean percent deviation of 4.2 $\pm$ 1.9% ($\pm$ standard error, N=8).

2.3.2 Stratigraphy & Age Model

The chronologies of Iridium Hill Annex and Nirvana localities (Fig. 2.1) are both constrained by ^{40}Ar/^{39}Ar dating (Sprain et al., 2018). The age model for each locality is determined by linearly interpolating between dated coal seams, and the two records are correlated using the Cretaceous-Paleogene boundary. Each locality contains the Cretaceous-Paleogene boundary within the Iridium Z (IrZ) coal and tephra layer (66.052 $\pm$ 0.008 Ma, Sprain et al. (2018)) and an additional dated horizon: the top of the Iridium Hill Annex section is the Hauso Flats Z (HFZ) coal, which contains

two dated tephra layers (65.973 $\pm$ 0.020 Ma, Sprain et al. (2015)) and Nirvana contains the McGuire Creek Z (MCZ) coal seam and tephra layer (66.024 $\pm$ 0.014 Ma, Ickert et al. (2015); Sprain et al. (2018)).

Linear interpolation between dates yields mean sediment accumulation rates (SARs) of 25 cm/ka for Iridium Hill Annex and 14.75 cm/ka for Nirvana. Both localities are entirely within magnetochron C29R, and although paleomagnetic sampling has not been done at these sites, the C29R/C29N reversal has been documented $\sim$15 m higher than the top of the Iridium Hill Annex section at the nearby Hell Hollow locality (Sprain et al., 2018). Utilizing the mean SARs both records have $\sim$2 ka resolution on average, $<$1 ka resolution close to the boundary, and combined they span 40 ka pre- and 80 ka post-impact.

Each of the coals used to calculate the SARs are in the Paleogene, in addition to the IrZ coal at the boundary. Given the lack of any other age constraints in these localities, we continue to utilize the same SAR in the Cretaceous portion of the sections. This extrapolation is justified given the average late Maastrichtian age SAR of 19 $\pm$ 4 cm/ka in several Hell Creek Formation localities approximately 50 km from IRA and NV, where a tephra layer in the late Maastrichtian is dated in addition to the MCZ (Sprain et al., 2015).

We acknowledge that in a fluvial/floodplain system, the SAR may not be constant. Nevertheless, it is impossible to determine the SAR more accurately in this interval given the current chronostratigraphic constraints. We note that there are no large channels within these sections and no evidence of prolonged hiatuses in sedimentation. Hiatuses may decrease mercury concentrations in the exposed sediment surface due to dissolution into river water or runoff, which in a fluvial system may be greater magnitude than adsorption of dissolved mercury. The mercury concentration would then presumably return to background levels in overlying sediment.

2.3.3 Mercury Box Model

2.3.3.1 Box Model Parameters

A box model for modern mercury cycling (Fig. 2.2) was used to predict when gaseous mercury from a subaerial volcanic eruption is ultimately deposited, as well as estimate the size of atmospheric mercury pulse required to create the peaks in our record (Amos, Jacob, Streets, & Sunderland, 2013; Amos et al., 2014, 2015) (https://github.com/SunderlandLab/gbc-boxmodel). This model approximates the global mercury cycle as an exchange between seven reservoirs: three terrestrial sediment pools (fast, slow, armored), three ocean water pools, and the atmosphere. The model also incorporates coastal and deep marine sediments as sinks. All rate coefficients and initial/steady state reservoir sizes are based on extensive analysis and calibration with detailed models and observations of the modern mercury cycle (Amos et al., 2015). The box model can produce a good agreement with observed anthropogenic mercury increases in terrestrial peats and lake sediments (Amos et al., 2015).

The lack of detailed spatial or climate parameterization make the box model general enough to extrapolate back to the Cretaceous. However, the rate coefficients may not accurately reflect

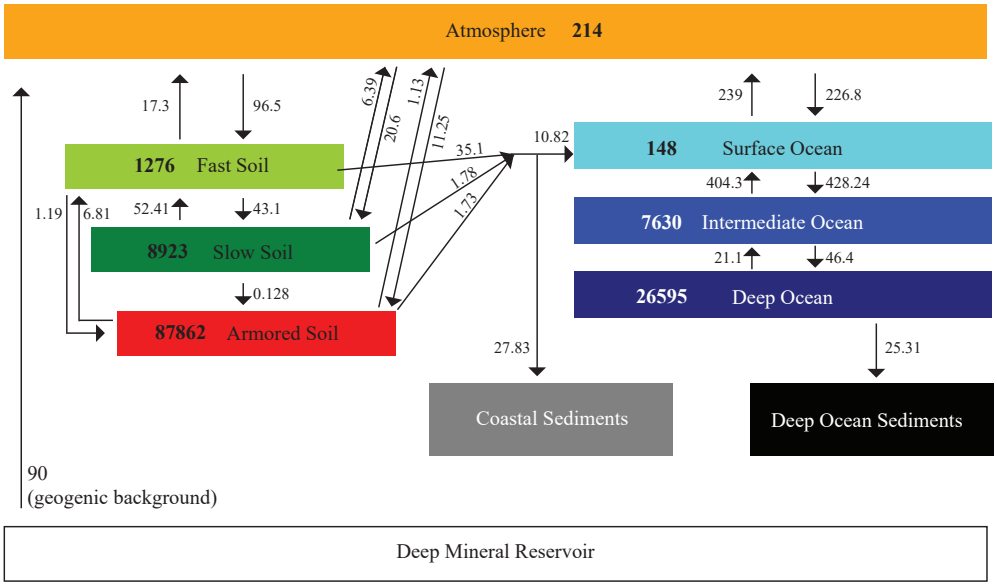

Figure 2.2: Schematic for the modern mercury box model utilized in this study (Amos et al., 2013). Steady-state reservoir sizes used are from the most recent model version (Amos et al., 2015) and are reported in Mg and Mg/a respectively. Both reservoir sizes and fluxes will change in response to a perturbation, as fluxes are scaled to the reservoir sizes. Marine sediment and the deep mineral reservoirs do not have steady state sizes, as they are solely sinks and a source respectively. Enrichment factors for marine sediment reservoirs are therefore calculated with respect to the flux. In this model, all input to coastal marine sediment is assumed to be suspended sediment from rivers, deposited on the continental shelf.

Cretaceous mercury cycle conditions. There are critical differences between late Cretaceous, early Paleogene, and modern environments. The most important factors for the global mercury cycle are potentially the lack of ice caps and permafrost, a generally warmer global climate, and the runoff and ocean circulation changes that may have accompanied the mass extinction. Ice and snowpack are already not explicitly included in the model (Amos et al., 2013). The potential increase in runoff at the Cretaceous-Paleogene boundary, plus rapid temperature fluctuations, may increase the transfer rate from terrestrial sediments to the ocean. However, the amplitude of these effects is presently not well constrained, even for modern global warming scenarios (Lugato et al., 2018). Lastly, the disturbance of the biological pump due to the mass extinction will presumably have changed mercury cycling between the surface and deeper ocean reservoirs, though it is unlikely to have affected terrestrial reservoirs significantly.

We therefore used the rate constants and initial reservoir sizes from Amos et al. (2015) and introduced pulses of atmospheric mercury via the model's anthropogenic input parameter. We set

the background geogenic (volcanic, hydrothermal, and other natural background sources) mercury input at 90 megagrams per year (Mg/a), consistent with recent estimates of volcanogenic mercury (Amos et al., 2013; Bagnato et al., 2011, 2014). The geogenic background is the primary source of uncertainty in the model, as background mercury flux from volcanism and weathering during this interval is unknown and may include smaller magnitude Deccan eruptions and any persistent non-eruptive volcanic gas release. An increase in the geogenic background would increase the size of all the box model reservoirs; for example, a significantly larger geogenic background of 200 Mg/a leads all reservoirs to increase by a factor of $\sim$2.2. Consequently, a more massive volcanic pulse is required to enhance the mercury concentrations for geogenic emissions of 200 Mg/a compared to 90 Mg/a. Another critical assumption in the model is the absence of a terrestrial sediment sink. In this study, we assume that the terrestrial sediments sample the concentration of the various terrestrial mercury reservoirs and that the amplitude of any terrestrial sediment sink is small compared to the other fluxes.

For each model run, we calculate an enrichment factor for each of the terrestrial pools and ocean sediment pools. The model enrichment factor is simply the reservoir size at any time-step divided by the initial reservoir size. These terrestrial pools of the mercury model (Smith-Downey, Sunderland, & Jacob, 2010) are based on terrestrial carbon cycle pools using the framework of the CASA carbon biogeochemical model (Potter et al., 1993). They are each defined by their residence times: the fast terrestrial carbon pool (primarily organic litter) turns over in about a year, the slow (topsoil) does so in decades, and the armored (deeper soil, sediment) pool in hundreds to thousands of years (Potter et al., 1993). To approximate a fluvial sediment enrichment factor, we calculate a combination of 10% fast, 80% slow, and 10% armored enrichment factors. This combination of fast-slow-armored is because rivers source sediment from topsoil or upper sediment horizons, which generally have appropriate turnover times for the slow pool (Mathieu, Hatté, Balesdent, & Parent, 2015). Rivers also incorporate organic litter and deeper sediment, so we include 10% fast and armored reservoirs respectively. This choice affects the response rate of the modeled record to the mercury pulse.

Fluid infiltration diffuses mercury concentration over the top few centimeters of riverine wetland sediment at the time of deposition (e.g., Goulet et al., 2007). Iridium Hill Annex and Nirvana have SARs of $\sim$25 cm/ka and $\sim$14 cm/ka respectively, and thus with 2 cm of equilibration each sample averages over $\sim$80-142 years of mercury deposition. To approximate this diffusion, we apply a moving smoothing window with a width of 125 years. This also accounts for the size of samples, which are homogenized during preparation. Changing the SAR in the model affects the peak size and duration of mercury enrichment in response to an atmospheric pulse (Fig. 2.3). This is illustrated by the lower peak enrichment factor for a wider smoothing window (625 years).

In coastal ocean sediment, bioturbation can lead to mixing on vertical scales of order 5 cm, and potentially much larger. Conservatively, we apply smoothing windows averaging over widths of 2500 years and 5000 years to represent SARs of a few cm/ka (Fig. 2.3). We report the enrichments in terrestrial and marine reservoirs for a variety of pulse sizes, durations, and smoothing window widths (Model tables and Fig. 2.4).

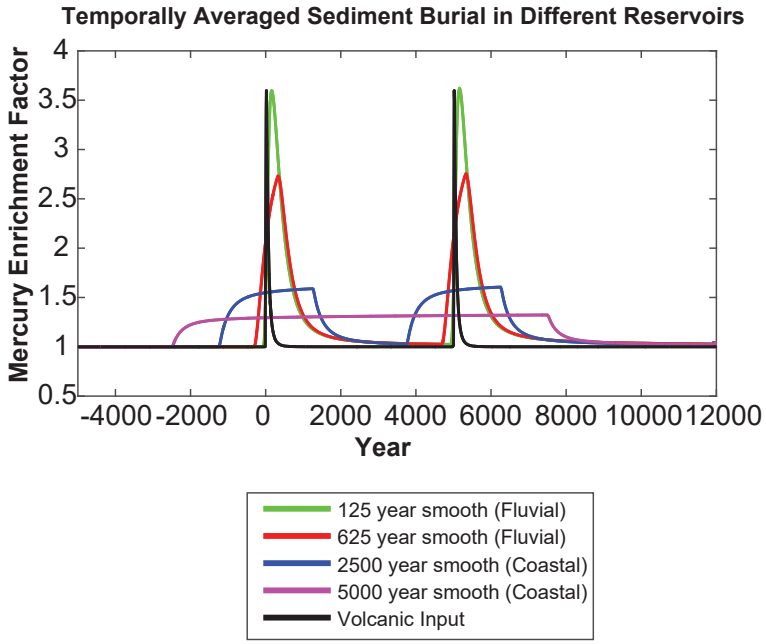

Figure 2.3: Modelled mercury enrichment factors for fluvial and coastal marine sediments for typical ranges of sediment accumulation rates, before, during, and after two 2000 Mg/a, 100-year atmospheric Hg pulses. The fluvial sediment is assumed to be dominantly sampling the slow soil reservoir of the box model (Amos et al. 2014).

2.4 Results

2.4.1 Mercury Concentration Chemostratigraphy

Both Iridium Hill Annex (IRA) and Nirvana (NV) have elevated mercury concentration 1000 years (15 cm) of the Cretaceous-Paleogene boundary (177 ng/g at IRA, 252 ng/g at NV), and there are additional mercury peaks both above and below the boundary (Fig. 2.5). The background mercury concentration in this interval is approximately 30-50 ng/g at both localities, similar to those predicted by pre-anthropogenic mercury budgets (e.g., Fitzgerald & Lamborg, 2014). The peaks correspond to enrichment factors of 3-5 with respect to this background. As the interval analyzed is entirely within the Deccan eruptive period, it is possible that this background is elevated during this entire interval due to smaller ongoing Deccan eruptions or any non-eruptive persistent mercury degassing, including from intrusive magmas via fumaroles (e.g., Witt, Fischer, Pyle, Yang, & Zellmer, 2008). If this is the case, larger quantities of mercury are required to cause the observed enrichment factors. (Fig. 2.3).

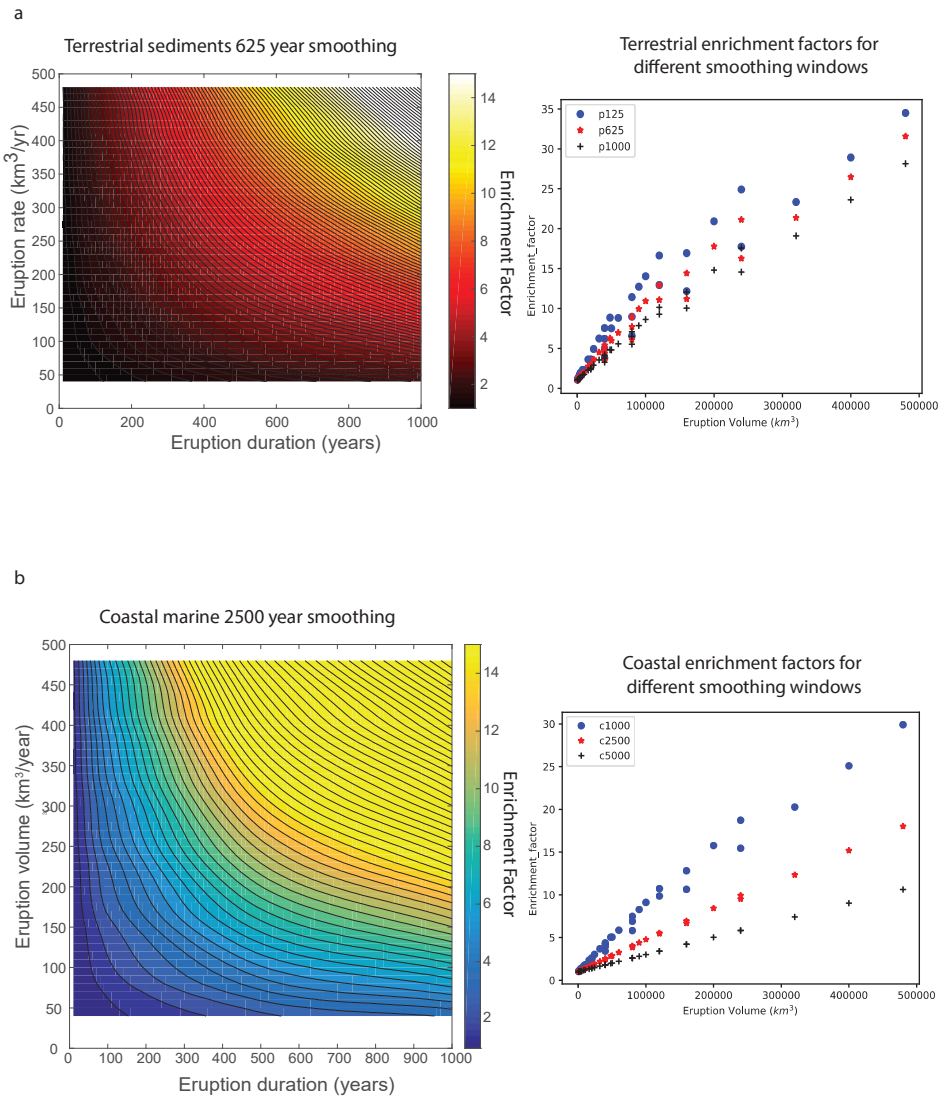

Figure 2.4: **a)** Peak enrichment factors in terrestrial sediment with 625 year smoothing window following a mercury pulse for a range of eruption rates, and durations. On the right, terrestrial enrichment factors utilizing 3 different smoothing windows (125, 625, and 1000) following a range of eruptive volumes. Multiple peak enrichment factors are possible per eruptive volume as enrichment is not symmetric with respect to rate and duration (so there are multiple paths to the same volume). **b)** Peak enrichment factors in coastal marine sediment with 2500 year smoothing window following a mercury pulse for a range of eruption rates, and durations. On the right, coastal marine enrichment factors utilizing 3 different smoothing windows (1000, 2500, 5000) following a range of eruptive volumes.

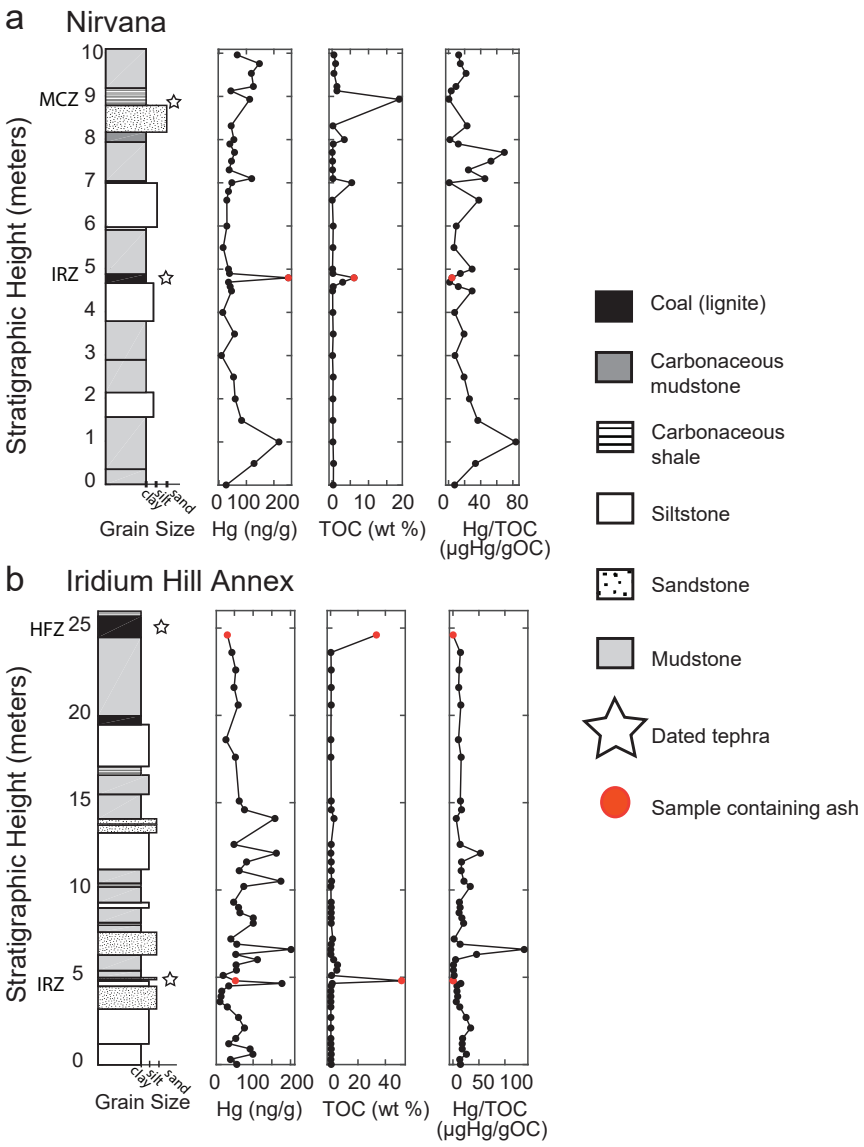

Figure 2.5: Stratigraphic sections, mercury (Hg), total organic carbon (TOC), and Hg/TOC data for both localities analyzed in this study.

2.4.2 Mercury and Total Organic Carbon

There is not generally a strong relationship between mercury and organic carbon in our data (Fig. 2.6 a). Thus the estimated enrichment factors remain ∼3-5 when normalized to TOC, with respect to a background of ∼15μg Hg/g OC. While at lower TOC there is a vague relationship between mercury and TOC (Fig. 2.6 b), there is a point at which increasing TOC does not increase mercury deposition, and samples with high TOC (>1%) do not have consistently higher mercury concentrations. The relationship between mercury and TOC, particularly in the geologic record, is known to be complex (e.g., Grasby, Sanei, Beauchamp, & Chen, 2013; Percival et al., 2018; Sanei et al., 2012) and presumably a function of the type of organic material in addition to the availability of sulfides, clays, or other materials with which mercury can be deposited. These factors lead to some unquantifiable uncertainty in our enrichment factors.

2.4.3 Box Model Eruption Size Estimates

Eruptions are modeled as mercury pulses using a modern mercury cycle box model (Amos et al., 2013, 2014). These pulses cause inflation of the modeled global mercury budget and an increase in each of the modeled reservoirs. We also apply a smoothing window to the modeled terrestrial record, based on SAR. High enrichment factors are caused by a high rate of mercury emission, long duration of a pulse, or both. A range of mercury pulse sizes could cause terrestrial enrichment factors of 3-5: ∼2000-3000 Mg/a for ∼100-year eruptions, or longer events of smaller magnitude, e.g. a 500 Mg/a pulse for ∼1000 years.

To further constrain the eruptive duration, we consider how much time is needed for an individual pulse of atmospheric mercury to be completely deposited into sediment. Using the same box model, we plot the total environmental enrichment for 1500 years, during and after a century-long 2000 Mg Hg/a eruption, along with the proportion of the enrichment in each reservoir (Fig. 2.7 a, b, c). It can be seen that increased mercury deposition in terrestrial systems lasts a maximum of a thousand years post eruption (Fig. 2.7 c). As consecutive samples with elevated mercury are rare within the 1-2 ka resolution record, we infer that these individual eruptions lasted a few centuries, and no longer than ∼500 years. At a 500 year duration or longer, one would expect the eruption to cause elevated mercury concentrations in multiple consecutive samples. This additional constraint now limits the range to 100-year events emitting pulses of 2000-3000 Mg/a to 500-year events emitting 500-1000 Mg/a.

Approximately 12.5 Mg mercury is released per cubic kilometer of basalt erupted, using an average volcanic mercury to sulfur ratio (Bagnato et al., 2014; Fitzgerald & Lamborg, 2014) along with estimates of Deccan sulfur content from melt inclusions (Schmidt et al., 2016; Self, Blake, Sharma, Widdowson, & Sephton, 2008). Peak terrestrial enrichment factors of 3-5 then suggest eruptive rates of ∼40-80 km^3/a for 500-year events and ∼160-240 km^3/a for 100-year events (Fig. 2.8), resulting in maximum eruptive volumes of 16,000-40,000 km^3. There are ∼10 peaks in our record, resulting in a cumulative 160,000-400,000 km^3 of basalt, which is within an order of magnitude of the independent estimate of ∼150,000-200,000 km^3 of basalt emplaced in the first ∼100 ka of the Paleocene (Jay & Widdowson, 2008; Schoene et al., 2019; Sprain et al., 2019).

a

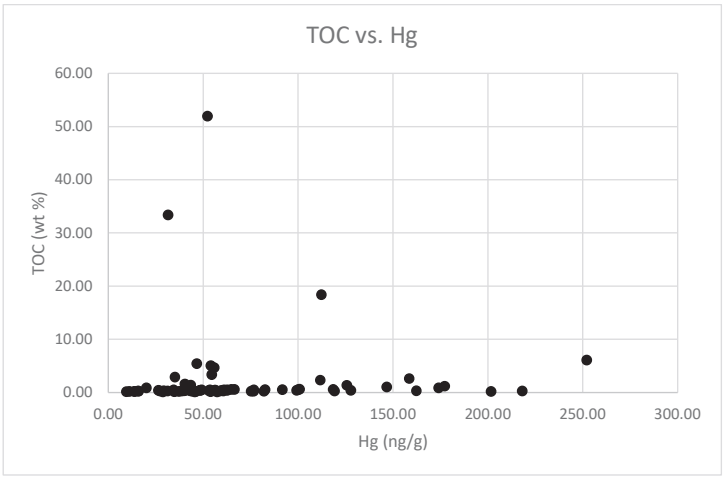

b

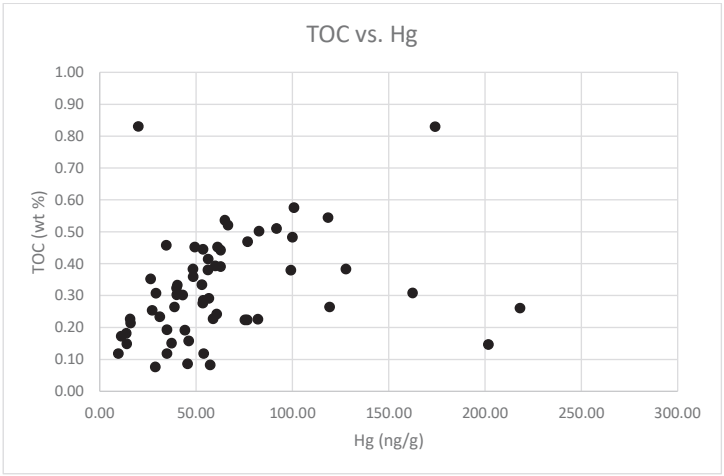

Figure 2.6: **a)** Mercury (Hg) vs. total organic carbon (TOC) plotted for all samples **b)** Mercury (Hg) vs. total organic carbon (TOC) plotted for all samples for which TOC is less than 1%

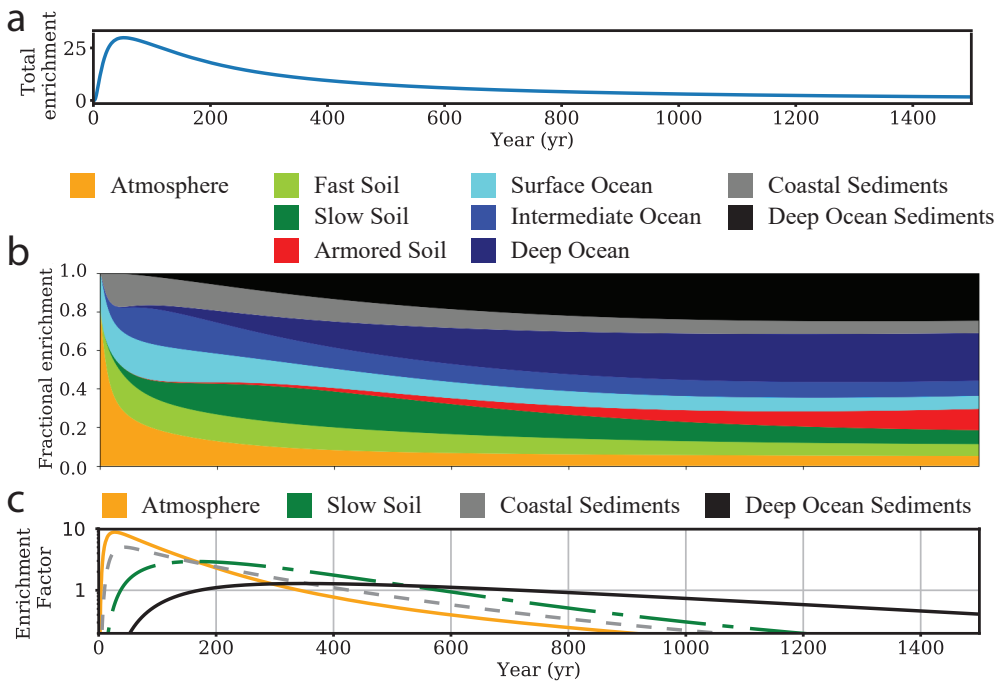

Figure 2.7: **a)** Total environmental mercury enrichment (above background) summed over all reservoirs through time following a Deccan-scale 2000 Mg/a, 100-year atmospheric mercury pulse input into a modern mercury box model (Amos et al. 2014). **b)** The proportion of the total enrichment within each reservoir following the same atmospheric mercury pulse. **c)** The enrichment factors (above background) in the atmospheric reservoir, terrestrial fast and slow soil reservoirs, and marine coastal and deep ocean sediment reservoirs following the same atmospheric mercury pulse.

These field-based volume estimates are likely lower bounds since an uncertain, but presumably large, amount of Deccan Traps basalt has been eroded in India's tropical environment over the last 66 Ma.

2.5 Discussion

2.5.1 Potential Mercury Sources

There are a few non-Deccan potential mercury sources: a) sedimentary (fluid remobilization) effects, b) local volcanism, or re-mobilization of sedimentary/biomass mercury due to c) wildfires, or d) via changes in weathering. We do not believe these are the dominant mercury sources for the following reasons:

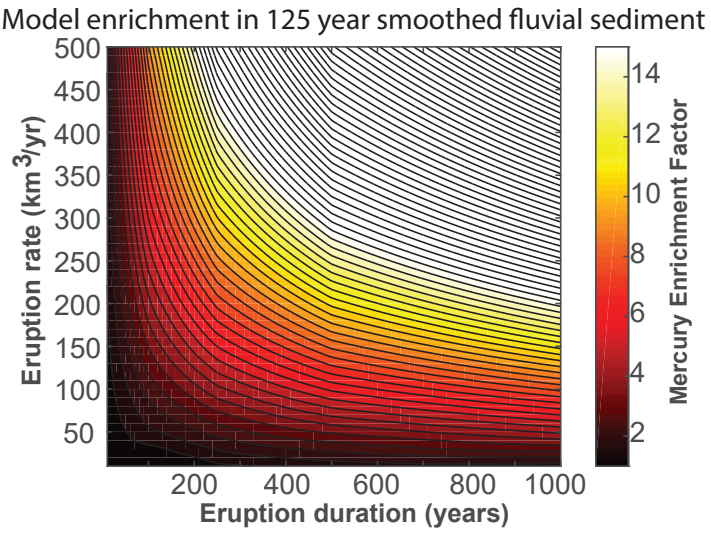

Figure 2.8: Mercury enrichment factors in the terrestrial reservoir, with 125 years sediment averaging, for a range of eruptive volumes and durations.

2.5.1.1 Sedimentary Effects

The presence of similar size mercury concentration peaks at both localities demonstrates that these are at least regional signals, rather than due to any local sedimentary/fluid remobilization effect. Additionally, we have ruled out variation due to changes in organic carbon concentration, and there is no visible pyrite, including within lignites, suggesting that sulfides are not the primary control on mercury concentrations.

2.5.1.2 Local Volcanic Eruptions

Local volcanic eruptions, from the Bitterroot Lobe of the Idaho Batholith (Ickert et al., 2015), frequently occur during the Cretaceous and Paleocene. Several samples contain tephra from these eruptions, as well as immediately surrounding sediment. However, these samples do not record elevated mercury concentrations (Fig 2.5). The only exception is the Nirvana sample, which contains the IrZ tephra layer as well as the Cretaceous-Paleogene boundary clay.

We believe this lack of signal to be due to the short duration of the local eruptions. As mercury equilibrates over a few centimeters of sediment post-deposition (e.g., Goulet et al., 2007), short duration pulses in atmospheric mercury are only likely to be preserved if they are very large, the SAR is very high, and/or the record is sampled at a resolution within about an order of magnitude of the duration of the pulse. This is apparent when examining Quaternary records. Mercury peaks caused by arc volcanism and local wildfires (presumably all $<$ 1-year duration events) have been found in recent lake sediments with an average SAR of 37.5 cm/ka, sampled at a resolution of every $\sim$20 years (Daga et al., 2016). Conversely, a Quaternary marine sedimentary mercury record with

an average SAR of 7 cm/ka, sampled at a 1000-2000 year resolution (Kita et al., 2016), does not record the large volume, but short duration, Toba (5300 km^3, $\sim$74 ka; (Costa, Smith, Macedonio, & Matthews, 2014)) and Bishop Tuff ($\sim$600 km^3, $\sim$760 ka; (Hildreth & Wilson, 2007)) eruptions.

While the terrestrial sediment records compiled in this study have high average SARs (14, 25 cm/ka), we are sampling them at a resolution of every 1000-2000 years. The local arc volcanic eruptions did not last longer than a few days to months, and the frequency of very large ($>$100 km^3) eruptions likely did not exceed once every several thousand years (e.g., Papale, 2018). In order to be preserved as significant anomalies at this resolution, eruptions need to be at least $\sim$100 years in duration, longer than the $<$1 year local eruptions.

2.5.1.3 Wildfires

Fires remobilize mercury taken up by biomass from the atmosphere and redistribute it (Friedli, Arellano, Cinnirella, & Pirrone, 2009). Similar to the local volcanic eruptions, wildfires are likely to be short duration events ($<$1 year) and as such are smoothed out over centuries once deposited in the sedimentary record. These small local events are not likely to cause significant perturbations in a 1000-2000 year resolution record. It is possible that peaks correspond with much larger fire events. However, western North America does not record a strong/visible presence of charcoal in this time interval (Belcher, Collinson, Sweet, Hildebrand, & Scott, 2003), and the Cretaceous-Paleogene boundary does not record polycyclic aromatic hydrocarbons (PAH) indicative of massive wildfires (Belcher, Finch, Collinson, Scott, & Grassineau, 2009). Additionally, there is no indication of globally significant wildfires in the earliest Paleocene in PAH records from Europe (Arinobu, Ishiwatari, Kaiho, & Lamolda, 1999).

2.5.1.4 Weathering

Changes in weathering can also redistribute sedimentary mercury (e.g., Them et al., 2019). While changes in weathering may contribute to aggregate effects, particularly in oceans where the sediment and mercury are tied to continent-scale sources, our sediment catchment is comparatively small. In order to increase the concentration of mercury via increased weathering, a substantial amount of the mercury in weathered rock would need to be rapidly dissolved, and re-deposited locally. This process is most efficient when the rock fragments are entirely in suspension and even then only a fraction (generally <20% in 24 hours) of the mercury is re-dissolved (Gibson, Ptacek, Blowes, & Daugherty, 2015). Therefore in order to cause a factor of 3-5 increase in mercury for 100 years, the amount of material weathered is required to at least triple, and more likely increase by 15 times or more. While that may be the case right at the boundary, coincident with destabilization of floral ecosystems (Vajda & McLoughlin, 2004), there is no evidence of strongly enhanced weathering occurring thousands of years into the Paleogene.

2.5.2 Box Model Assumptions

The modeling framework we have utilized has a combination of strengths and drawbacks. One major strength is that the box model incorporates biogeochemical recycling instead of assuming that sediments are passively collecting mercury from the atmosphere and retaining all of it. The model results demonstrate that even though volcanogenic mercury may not be immediately deposited in the sediment, large pulses do cause increases in mercury concentration in all reservoirs on a timescale that should be capable of preservation in the geologic record.

A significant assumption in the model framework is the use of a constant SAR, which may not be the case in a terrestrial floodplain environment. The dependency on this assumption is due to using a moving average to approximate equilibration of mercury over 2 cm of sediment, to simulate both in-lab sample homogenization and fluid infiltration at the time of deposition. This results in the same mercury pulse causing a smaller enrichment in environments with lower SARs, and vice versa (Fig. 2.3). This effect is also crucial for marine records, where the deposition process of mercury can be complicated due to ocean currents, water depth, and ocean mixing time (e.g., Lamborg et al., 2014).

Another complicating factor is that although large emissions of gaseous mercury are distributed globally, they are distributed unevenly (e.g., Chen et al., 2018). This contributes to differences between mercury records from different locations, and uncertainty in eruption size estimates. Therefore perhaps less Deccan mercury was deposited in Montana than predicted by the box model, as Montana and India are on opposite sides of the globe and were in opposite hemispheres during the Cretaceous.

2.5.3 Comparison of Cretaceous-Paleogene Mercury Records

The mercury enrichment factors (multiple of locality-specific background Hg/TOC) calculated for each record are used to test consistency between different mercury records as well as with the estimated eruption sizes. Our modeling framework illustrates that the SAR and sampling resolution must be explicitly considered when comparing mercury records. The response time to a mercury pulse is similar for both coastal marine sediments and terrestrial sediments (Fig. 2.7 c). However, SARs are frequently lower in marine environments, leading to a lower expected enrichment factor for a given eruption size. Sampling resolution is equally important, as mercury tends to be deposited rapidly into sediments – within about an order of magnitude of the pulse duration (Fig. 2.7 a). Therefore records sampled at millennial scale resolution have the highest likelihood of capturing eruptions which each lasted several hundred to a thousand years. Eruptive events of the proposed scale may be captured in records with lower sampling resolution, but they are likely to have smaller enrichment factors and fewer peaks, as the odds of sampling the moment of peak enrichment decrease. Most mercury records show higher enrichment factors when the sampling resolution is higher (Font et al., 2016; Keller et al., 2018; Percival et al., 2018; Sial et al., 2016).

The peak enrichment factors are similar between the Nirvana and Iridium Hill Annex localities, which supports the interpretation that they are caused by eruptive events of similar magnitude (Fig.

2.9). These estimates of eruption size are also generally consistent with the mercury enrichment factors of other Cretaceous-Paleogene mercury chemostratigraphies. The Seymour Island record, which has a comparable SAR of 20 cm/ka and sampling resolution of ∼2500 years, has Hg/TOC enrichment factors of ∼3 in peaks close to the boundary (Percival et al., 2018). The Gilbert Creek locality within the Hell Creek Formation presumably has a similar SAR, although the exact chronology is uncertain (Percival et al., 2018). Peak Hg/TOC enrichment factors at Gilbert Creek are 5-6 in the late Cretaceous, with smaller peaks closer to the boundary, although the lack of a definitive IrZ tephra layer makes correlation with our records uncertain (Percival et al., 2018).

Coastal marine sediments with SARs of a few cm/ka, utilizing a smoothing window of 2500 years, are expected to have enrichment factors of 2-3 for the estimated eruption volumes (Fig. 2.4 b). This is consistent with observed Hg/TOC enrichments in marine localities. Bass River (ODP Leg 174AX) has SAR of ∼ 1 cm/ka, a sampling interval of ∼ 7500 years, and correspondingly low enrichment factors of 1.5 to 2 (Percival et al., 2018). Elles, El Kef, and Bidart have enrichment factors of 2-4, SARs of approximately 1- 4 cm/ka, and sampling resolutions of ∼ 2000-5000 years (Font et al., 2016; Keller et al., 2018; Vonhof & Smit, 1997). Bottaccione and Stevns Klint have SARs of approximately 1 and 4 cm/kyr respectively, and enrichment factors of perhaps 3, however the limited datasets make determining the background Hg/TOC difficult (Gilleaudeau et al., 2018; Sial et al., 2016; Sinnesael et al., 2016). Bottaccione has frequently low (<1 ng/g) mercury concentrations, which suggests availability in the water column may not control preservation. These comparisons exclude peaks at the boundary, and enrichment factors are calculated with respect to Deccan interval background for each locality. We have excluded records lacking TOC measurements or without robust age models, as well as Zumaia, where mercury deposition is strongly linked with sediment fluxes (Percival et al., 2018).

These records differ with respect to the timing of mercury peaks because it is unlikely that every record is capturing the same specific eruptions. This is true even for the Nirvana and Iridium Hill Annex records, despite their close proximity, comparable SARs, and sampling resolutions. The average time between the emission of a gaseous mercury pulse and ultimate burial in sediment is approximately 1000 years, and the peak enrichment factor in the modeled slow soil and coastal marine reservoirs is only reached for less than 500 years (Fig. 2.7). Thus, unless the time interval captured in each sample is synchronous between localities to within 500 years, the records will not be identical. Additionally, due to the inherently discontinuous nature of the sedimentary record at the century scale, even continuously sampled records from different localities would be unlikely to record the same eruptions. The stochasticity of sedimentation and the aliasing effects of sampling ensure that no two records would correlate perfectly.

2.5.4 Mercury Released by the Chicxulub Impact

Although we attribute the majority of our peaks to Deccan volcanism, we suggest that the mercury peak very close to the Cretaceous-Paleogene boundary, which is the largest in nearly every mercury record for this time interval (e.g., Keller et al., 2018; Percival et al., 2018; Sial et al., 2016), is at least partly due to the Chicxulub impact. At both localities in this study, this peak (4-6

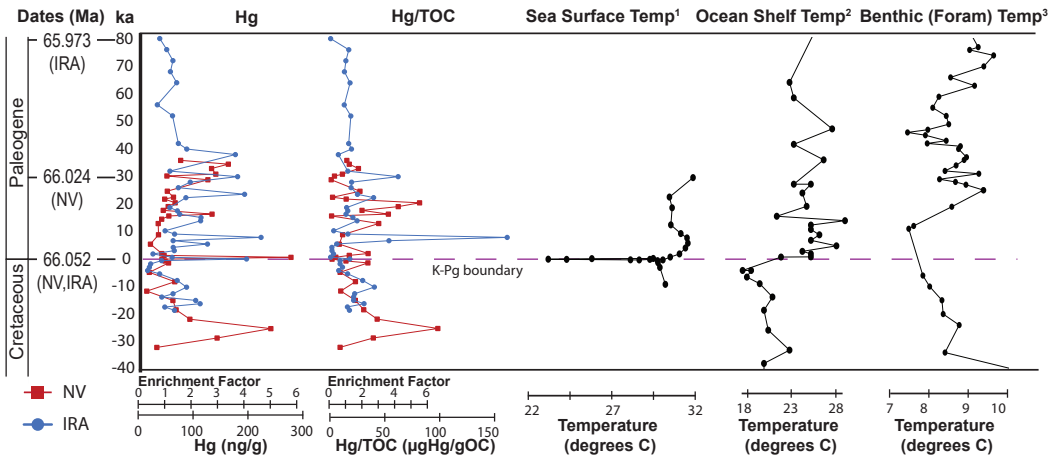

Figure 2.9: Mercury (Hg) and mercury/total organic carbon (Hg/TOC) for Iridium Hill Annex (IRA) and Nirvana (NV) Cretaceous-Paleogene boundary localities compared to several high-resolution temperature records. Dates for IRA and NV from Sprain et al. (2015, 2018). 1: Tex86 derived sea surface temperature from Brazos River, USA (Vellekoop et al., 2014). 2: Temperature derived from oxygen isotope composition of fish debris from El Kef, Tunisia (MacLeod et al., 2018). 3: Temperature derived from oxygen isotope composition of benthic foraminifers (*Nuttallides*) from IODP 1262 (J. S. K. Barnet et al., 2017).

x background) falls within a coal seam, so it is not visible when normalized to TOC. However, we do not see similarly high values in either of two other coal seams within our sections, and as other mercury records also have high values coincident with the boundary, this peak is most likely due to atmospheric mercury increase. An increase in weathering at the boundary may also contribute to this peak, or local sedimentary effects in sections where the boundary is coincident with a significant lithology change (Percival et al., 2018).

We calculate a potential amount of Hg release by the Chicxulub impact, and input it into the Hg box model as a 1-year atmospheric pulse. The actual impact would have released Hg presumably much faster than the smallest time step of the model, but given the response timescales of each sediment reservoir there is little difference between instantaneous or a single year pulse. The actual amount of Hg released is highly uncertain as are post-Chicxulub Hg dispersal patterns. Additionally, as sedimentation rates in the boundary horizon are partially determined by impact ejecta dispersal patterns, the reservoir enrichment factor may not precisely reflect concentrations, and the best choice of smoothing window is uncertain. We present two potential end-member scenarios.

2.5.4.1 Low Hg Release

The Chicxulub impact is estimated to have released 425 $\pm$ 60 Gt CO_2 and 325 $\pm$ 60 Gt S (Artemieva & Morgan, 2017). We calculate that this corresponds with 93927 Mg of mercury, assuming 40 ng/g Hg in calcite and anhydrite (Fitzgerald & Lamborg, 2014).

Enrichment factors:

1. Coastal marine: 19.5 with no smoothing window, 15 with 10 year window, and 2 with 1000 year smoothing. The enrichment factor remains above 1 for 500-1000 years.
2. Deep ocean: 1.64 with 1000 year smoothing window, 1.44 with 2000 year smoothing, and signal remains above 1.1 for $\sim$ 3000 years.
3. Terrestrial (same 10-80-10 mixture used previously): 3.8 for no smoothing, 3.5 with 10 year smoothing window, and 3.0 with 125 year smoothing. The signal is above 1.1 for 1500 years.

2.5.4.2 High Hg Release

If all 12,000 Gt of sediment which is ejected to high altitude releases its Hg, we calculate a total release of 480,000 Mg. Again we input it into the atmospheric box over 1 year.

Enrichment factors:

1. Coastal marine: 96 with no smoothing window, 73 with 10 year window, and 5.7 with 1000 year smoothing. The enrichment factor remains above 1 for 3000-4000 years.
2. Deep ocean: 4.3 with 1000 year smoothing window, 3.2 with 2000 year smoothing. The signal remains above 1.1 for $\sim$ 5000 years.
3. Terrestrial (same 10-80-10 mixture used previously): 15 for no smoothing, 14 with 10 year smoothing window, and 11.3 with 125 year smoothing. The signal is above 1.1 for 2000 years.

In summary, the Chicxulub impact likely released $\sim$94,000-480,000 Mg mercury instantaneously, based on the mass of evaporites vaporized and an assumed concentration of 40 ng/g mercury (Artemieva and Morgan, 2017; Fitzgerald and Lamborg, 2014). This mercury release could result in enrichment factors of at least 20 in coastal marine sediments and 4-15 in terrestrial sediments, consistent with the 4-6 x background peak we observe (excluding TOC normalization).

2.5.5 Implications for Deccan Volcanism and Climate

We have estimated, based on our mercury analyses, that these Deccan eruptions consisted of basalt fluxes between $\sim$40-80 km^3/a for 500-year events and $\sim$160-240 km^3/a for 100-year events (Fig. 2.8). Flood basalt eruptions have been independently hypothesized to be of the order of 103-104 km^3 in volume (Self et al., 2006) therefore we believe our mercury-based estimates of

16,000-40,000 km^3 per eruption (or series of closely spaced individual eruptions) to be reasonable. Additionally, there likely were more eruptions within this time interval than peaks in the records. Although biogeochemical recycling of mercury does extend the deposition time of pulses, shorter duration ($\leq$100 years) events of smaller magnitude may not be captured at our 1000-2000 year sampling resolution or will correspond to low enrichment factors. While it is thus difficult to estimate the minimum hiatus duration, these records indicate a maximum of 10,000 years between each eruption for the interval spanning 30 ka prior to and post-Cretaceous-Paleogene boundary.

The Deccan eruptions of the size indicated by the mercury peaks have the potential to cause sulfate aerosol driven climate cooling. A mercury pulse of 500-3000 Mg/a (240 km^3/a basalt) corresponds to a release of 200-1200 Tg/a SO_2, using, as before, an average volcanic Hg/S ratio of 5 x 10-6 by weight (Fitzgerald & Lamborg, 2014). Climate models indicate that similar rates of sulfur release would cause cooling of $\sim$1-6°C for the duration of the eruption (Schmidt et al., 2016). This model estimate assumes all SO_2 emitted enters the stratosphere, although this may be an overestimate (Glaze, Self, Schmidt, & Hunter, 2017). This cooling may contribute to variability in climate records and to the immediate post boundary cool period. However, it is not clearly seen (Fig. 2.9), consistent with the eruptions being less than 500 years in duration. Despite the lack of geologic preservation, several centuries of cooling at least every 10,000 years may be sufficient to perturb ecological and climatological systems significantly.

Other studies demonstrate that eruptions of approximately this size are not likely to have caused CO_2 driven warming individually, but with less than 10,000-year hiatuses between them could have cumulatively contributed to warming (e.g., Tobin et al., 2016). The timing of these eruptions indicates that eruptive CO_2 likely contributed to the immediate post-boundary warming seen in several records (Fig. 2.9) (MacLeod, Quinton, Sepúlveda, & Negra, 2018; Vellekoop et al., 2014), however, it is unlikely that the eruptions were large enough to be the primary cause. There is, therefore, no clear correlation between Deccan Traps eruptions and climate records on a sub-100 ka scale, even during the interval hypothesized to contain the largest volume Deccan eruptions (Schoene et al., 2019; Sprain et al., 2019). Sub-1000 year resolution climate records have the potential to record these brief colder periods and address this inconsistency.

2.6 Conclusions

Periods of higher mercury concentration indicative of Deccan eruptions occur within 30 ka both prior to and post the Cretaceous-Paleogene boundary in sedimentary sequences in Montana. Utilizing a global mercury box model, we estimate that the mercury peaks correspond to eruptions with magma output fluxes of 40-240 km^3/a, which lasted 100-500 years, and occurred at least every 10,000 years. This demonstrates that mercury chemostratigraphy can be used as a tool to quantitatively assess flood basalt eruptive dynamics. Deccan eruptions of the estimated size are hypothesized to have released enough SO_2 to cause significant ($\sim$1-6°C) cooling for their duration. However, with a duration of less than 1000 years, these cooler periods are not long enough to be unambiguously preserved in most available climate records. Higher resolution climate records, or statistical analyses of existing records, are needed in order to evaluate whether these cool periods

occurred. Nevertheless, if the cooler periods occurred as hypothesized, the repeated significant climatic perturbations within 50 ka of the Cretaceous-Paleogene boundary may have contributed to ecological changes.

2.7 Data Availability

Data including mercury and carbon concentration data are available in the supplementary materials of the published version (https://doi.org/10.1016/j.epsl.2019.115721).

Chapter 3

No Cretaceous-Paleogene boundary in exposed Rajahmundry Traps: A refined chronology of the longest Deccan lava flows from ^{40}Ar/^{39}Ar dates, magnetostratigraphy, and biostratigraphy

3.1 Introduction

The Deccan Traps continental flood basalt eruptions spanned the Cretaceous-Paleogene boundary mass extinction event, with >90% of the volume emplaced in approximately 1 million years (e.g., Courtillot et al., 1986; Schoene et al., 2019; Sprain et al., 2019). It is estimated that at least 1 million km^3 of basalt was erupted, forming the Main Deccan Volcanic Province (MDVP, Fig. 3.1a), best exposed in the Western Ghats, along with several other smaller provinces including the Mandla Lobe and Malwa Plateau (e.g., Mahoney, 1988). The periods of largest eruptive flux are hypothesized to correspond to the most significant climate effects, via eruptive CO_2 and SO_2 release (e.g., Self et al., 2006). Understanding of eruptive timing and flux is required to estimate eruptive CO_2 emissions and hence directly compare eruptive history, hypothesized climate effects, and climate records. Consequently, constraining the timing and volume of the largest eruptions is one crucial part of understanding and testing the mechanisms through which Deccan eruptions impacted the environment. In particular, these constraints can help us assess the importance of eruptive versus non-eruptive degassing of magmatic volatiles for Deccan-associated climate change (e.g., Hull et al., 2020; Sprain et al., 2019).

The exposed Rajahmundry Traps (RT) in eastern India potentially represent some of the largest volume Deccan Traps eruptions as they are ∼1000 km from the hypothesized Deccan eruptive centers near the present-day east coast of India, and ∼400 km from any other exposures of Deccan basalt (Fig. 3.1) (e.g., Baksi, 2001; Baksi, Byerly, Chan, & Farrar, 1994; Self, Jay, Widdowson,

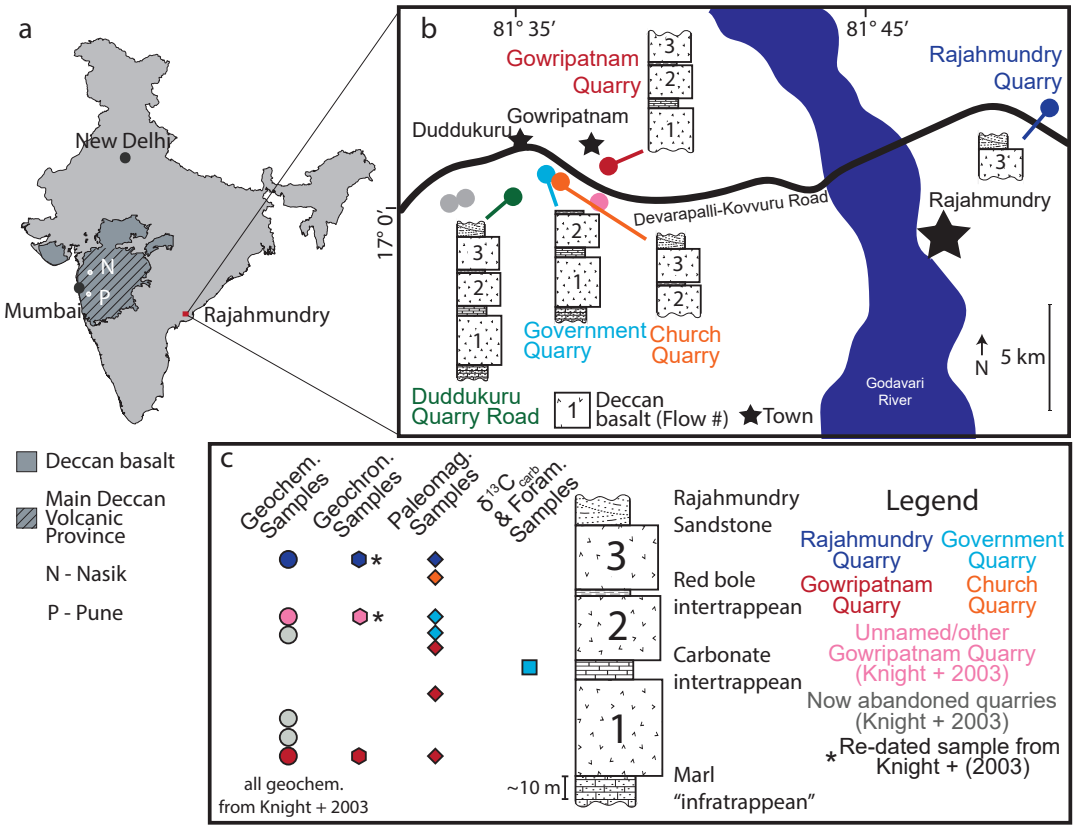

Figure 3.1: **a** Map of India showing the location of the Rajahmundry Traps (RT) as well as the Main Deccan Volcanic Province (MDVP), adapted from Kale et al. (2020). MDVP eruptive centers are hypothesized to be between Mumbai, Nasik (N), and Pune (P), based on occurrence of feeder dikes (e.g., Vanderkluysen et al., 2011). **b** Map of study localities, including which lava flows and sedimentary units are exposed at each site. **c** Schematic stratigraphic section with samples indicated. Quarry for each sample is indicated by color. For several of the Knight et al. (2003) samples, the quarry is now flooded and abandoned.

& Keszthelyi, 2008; Vanderkluysen, Mahoney, Hooper, Sheth, & Ray, 2011). Each Rajahmundry flow therefore corresponds with an erupted volume of ∼1000-6000 km^3 (length of 1000 km, width of 50-200 km and thickness of 20-30 m). This is comparable to the largest flow fields of the Siberian Traps flood basalts and the Columbia River Basalts (Krivolutskaya & Kedrovskaya, 2020; Vye-Brown, Self, & Barry, 2013).

Despite the great distance between them, the RT outcrops have long been associated with the Deccan Traps due to their geochemical and temporal similarity (Baksi et al., 1994; Blandford, 1867; Jay & Widdowson, 2008; Keller, Adatte, Gardin, Bartolini, & Bajpai, 2008; Knight, Renne, Halkett, & White, 2003). Some previous work suggested that the RT basalts span the Cretaceous-

Paleogene boundary and the C29r/C29n magnetic reversal. Previous $^{40}Ar/^{39}Ar$ dates indicated the RT are late Cretaceous to early Paleocene in age ($\sim$63-67 Ma) (Knight et al., 2003), and paleomagnetic analyses found that flows with normal magnetic polarity overlie reversely magnetized flows (Baksi, 2001; Vandamme & Courtillot, 1992). Additionally, Danian fossils found in a carbonate sequence between the lower two flows (e.g., Baksi et al., 1994; Keller et al., 2008; Sen & Sabale, 2011), and Maastrichtian fossils in the sediments below the lowest flow (e.g., Keller et al., 2008; Mukherjee, Bardhan, Mallick, Paul, & Das, 2013) suggested that the lowest flow was emplaced in the latest Cretaceous. These chronologic constraints led to the hypothesis that the lowest flow is part of an extremely voluminous Deccan eruptive episode just prior to the mass extinction and Cretaceous-Paleogene boundary (Keller et al., 2008, 2012; Lakshminarayana, Manikyamba, Khanna, Kanakdande, & Raju, 2010).

However, there has been no high-resolution and consistent chronostratigraphic framework for the region. One of the primary reasons for this is that exposures in the Rajahmundry area are only in active quarries - meaning that sampling locations, plus which lava flows are exposed, and even quarry names, are constantly changing over time. Consequently, it is challenging to assemble literature data, collected over decades, into a consistent chronostratigraphic framework. For instance, earlier studies describe the RT as having either two or three exposed flows depending on the sampling locality (e.g., Baksi et al., 1994; Keller et al., 2008; Sen & Sabale, 2011). Thus, for example, the precise stratigraphic location of the reverse to normal polarity transition is unclear due to these sampling uncertainties (Baksi, 2001; Knight et al., 2003; Subbarao & Pathak, 1993).

To ascertain potential climate or ecological impacts of the RT and Deccan eruptions more broadly, there is a need to determine a more precise timing of these large eruptions. In one commonly used stratigraphic scheme, the Deccan Traps basalts are divided into formations based on their chemistry, and these formations are assumed to be isochronous throughout the Main Deccan Volcanic Province (Beane, Turner, Hooper, Subbarao, & Walsh, 1986). Determining the timing of the RT eruptions is necessary in order to evaluate whether the RT are compatible with the contemporaneous MDVP geochemical formations. The RT have previously been shown to be most geochemically similar to the Ambenali and Mahabaleshwar Formations (Baksi, 2001).

However, the previous dates on the RT failed to demonstrate more than broad agreement with this assignment, since with an age uncertainty of $\sim$0.5 -1 Ma, the RT flows coincide with a large fraction of the main Deccan Traps eruptive period (Knight et al., 2003). With a refined chronostratigraphic framework for the RT, we can test whether the RT flows are still consistent with new high-resolution age constraints for these formations from the Western Ghats (Schoene et al., 2019; Sprain et al., 2019).

In this study, new geochronology for the RT refines their relationship with up to date geochemical stratigraphy and geochronology from the Western Ghats. This new chronostratigraphic framework refines the timing and eruptive rate of the RT eruptions, particularly with respect to the Cretaceous-Paleogene boundary. The updated framework allows us to assess the potential of the RT flows to have perturbed climate during the mass extinction and recovery.

3.2 Methods and Data

3.2.1 Geologic setting: Volcanology and Site Descriptions

The RT consist of a set of lava flows that have sediment beds between them (termed intertrappean sediments) and just below them (infratrappean sediments). This package is bounded by unconformities: the uppermost lava flow is directly overlain by the Eocene Rajahmundry sandstone, and the approximately conformable infratrappean sediments are underlain by the early to mid-Cretaceous Tirupati Formation (Bhalla, 1966; Geological Survey of India, 2000a, 2000b). Three lava flows and the overlying Rajahmundry sandstone are exposed in two quarries on the western side of the Godavari River, leaving no uncertainty with respect to their relative stratigraphy (Fig. 3.1 b, Fig. 3.2 a). Only one flow is exposed on the eastern side of the Godavari, which we and others parsimoniously interpret to be the uppermost flow from the western side, as it is overlain directly by an erosive contact with the Rajahmundry sandstone (Baksi, 2001; Fig. 3.2 b). This assignment is corroborated by our geochronology and magnetostratigraphy. The lowermost exposed flow is underlain by a highly fossiliferous marine marl to sandstone infratrappean unit which is potentially Maastrichtian in age (e.g., Sen & Sabale, 2011). While only three flows are exposed at the surface, several more, of unknown age, are documented in sub-surface drill cores (Keller et al., 2011) , and there is no exposed contact between the infratrappean sediments (or lowest exposed lava flow) and the underlying Tirupati Formation (Bhalla, 1966). We logged five quarry exposures, four on the western side of the Godavari River and one on the eastern side, all of which display fresh material and near vertical sections. After accounting for the relative location of the quarries, and factoring in the slight regional tilt to the south/south east towards the coast (e.g., Sahu, Raab, Kohn, Gleadow, & Bal, 2013), we conclude that the exposed Rajahmundry Traps comprise three lava flows, formed by three separate eruptions, consistent with some previous work (e.g., Lakshminarayana et al., 2010; Sen & Sabale, 2011). Reports of different numbers of lava flows in previous studies were most likely due to limited exposure caused by regional tilt and the presence of water tables at the base of flows. We here designate the lower, middle, and upper of the three flows as Flows 1, 2, and 3, respectively.

The lowest and thickest of the three lava flows (Flow 1) is approximately 30 m thick. Its base shows evidence for water-rock interaction such as rootless cones and entablature exhibiting fine columnar and radial jointing. It is a compound flow, with at least three or four thick inflated sheet lobes which display entablature, and the top of the flow forms a colonnade .

Flow 1 is separated from the Flow 2 by a sedimentary intertrappean bed which was deposited in a near coastal marine setting (e.g., Mallick, Bardhan, Das, Paul, & Goswami, 2014). The middle of this unit is generally highly fossiliferous limestone to marl, with more clay and silt towards the top. In one exposure (Government Quarry) there is a charcoal layer at the top, suggesting that Flow 2 erupted onto a layer of terrestrial vegetation. The thickness of the entire unit is between 3 and 5 m depending on location, and the lower part generally shows evidence of recrystallization and hydrothermal alteration (Keller et al., 2008). Flow 2 and Flow 3 are both $\sim$20 m thick and have columnar jointing throughout. They generally possess no fluid-lava interaction features, indicating

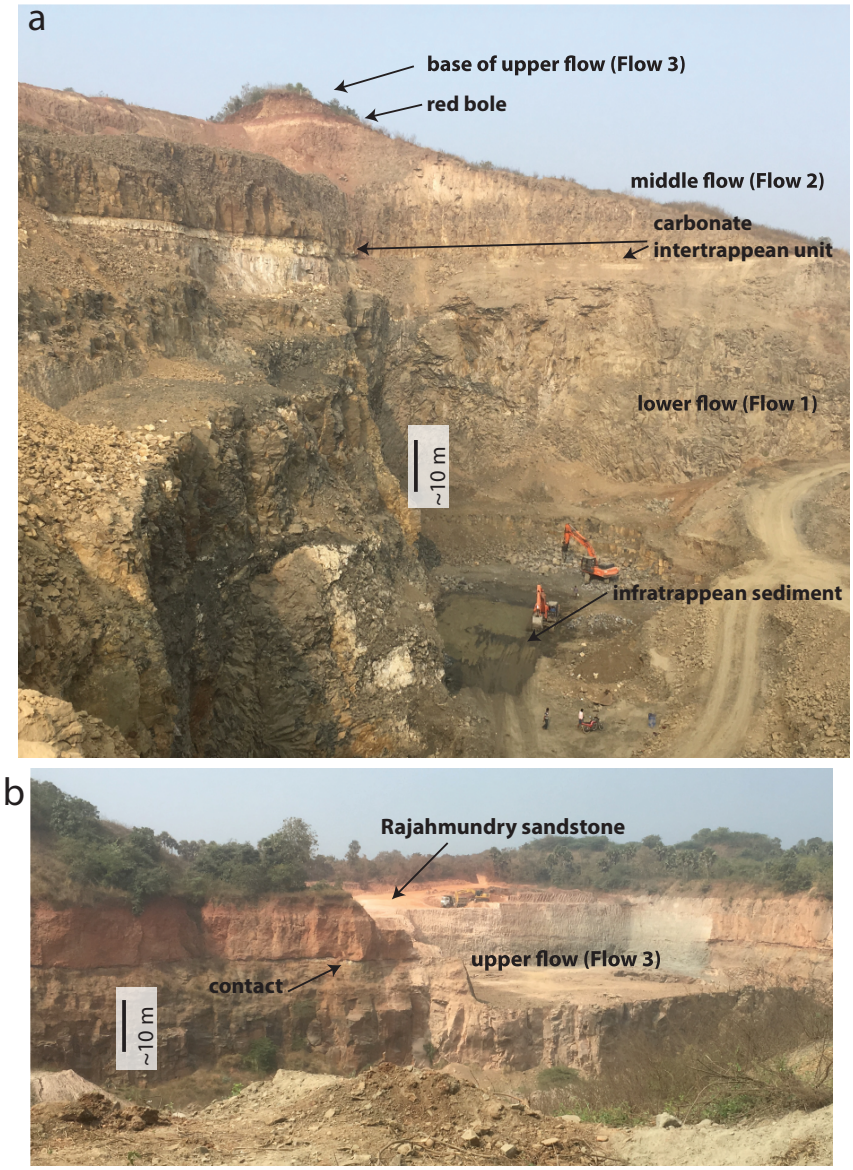

Figure 3.2: **a** Image showing all three flows exposed in the Gowripatnam Quarry. The finely spaced, irregular, columnar joints exhibited in Flow 1 are typical of water-cooled lavas. Note the water at the base of Flow 1 - the water table causes quarries to be flooded and consequently abandoned after they are excavated to the base of a lava flow. This leads to quarries exposing only one or two of the three flows. **b** Image showing the Rajahmundry sandstone and Flow 3 contact from the Duddukuru Quarry Road section on the western side of the Godavari River.

they were emplaced onto land or into extremely shallow water. However, in Gowripatnam Quarry Flow 2 has a second thin (1-2 m) lobe at the base with a finely jointed and highly vesicular texture, indicating rapid cooling . Flows 2 and 3 are separated by a 1-2 m thick sediment layer which is formed of red clay and is extremely similar in appearance to a very thick "red bole" of the main Deccan province (e.g., Ghosh, Sayeed, Islam, & Hundekari, 2006; Sen & Sabale, 2011; Widdowson, Walsh, & Subbarao, 1997). There are no fossils of any kind, suggesting negligible marine influence.

Our observations are in agreement with the previous conclusion that the first lava flow was emplaced into shallow water, corroborated by the shallow marine infratrappean and carbonate intertrappean units, whereas the upper two flows and the red bole were emplaced subaerially (e.g., Keller et al., 2008; Self, Jay, et al., 2008; Sen & Sabale, 2011). We interpret the Knight et al. (2003), Self, Jay, et al. (2008), and Keller et al. (2008) "upper flow" to be equivalent to our Flow 2 on the western side of the river, as there is limited exposure of the Flow 3 in those quarries, and Flow 1 is easily distinguished from Flow 2 because of the highly visible carbonate intertrappean unit at the top of Flow 1. On the eastern side of the river we have assigned the "upper flow" to Flow 3, as it is the only flow exposed in that area and it is overlain by the Rajahmundry sandstone.

3.2.2 Paleomagnetic Analyses

Samples for paleomagnetic analysis were selected from seven horizons, two from Flow 1, three from Flow 2, and two from Flow 3, collected from the Gowripatnam, Government, Church, and Rajahmundry Quarries (Fig. 3.1 b). At least three oriented blocks were collected from each horizon. One to three oriented 10-cm^3 specimen cubes were cut out of each block sample using a wet tile saw. After cutting, samples were sanded and blown with pressurized air to remove extraneous material from saw blades. All three lava flows had dips of only a few degrees, due to the regional tilt of $\leq 5^\circ$ to the south-southeast (Baksi, 2001). Tilt corrections were not performed, as they would alter the absolute direction by only a few degrees and all flows were similarly oriented. Flow 1: Two horizons (RJ17-1 and RJ17-2) from Flow 1 were sampled from the Gowripatnam Quarry. RJ17-1 was collected from the bottom of Flow 1, within 3-5 meters of the base of the flow and $\sim$25 m from the intertrappean. Here, the lava flow displays closely spaced columnar jointing/entablature. RJ17-2 was collected from the top of Flow 1, roughly 5 m below the intertrappean. Samples were collected within the upper colonnade/top of the entablature. Flow 2: Three horizons were sampled from Flow 2. One horizon from the base of the flow (RJ17-3), $\sim$ 2 m above the intertrappean, was collected from the Gowripatnam Quarry. The other two were collected from the Government Quarry (RJ17-6 and RJ17-7). RJ17-7 was collected from the lower columnar jointed portion of Flow 2, $\sim$ 4-5 m above the top of the intertrappean. RJ17-6 was collected from the middle part of Flow 2, $\sim$ 7-10 m below the red bole topping Flow 2. Samples were collected at the top of coarsely spaced columnar joints ($\sim$ 1 m spacing), close to the top of the core of the flow. Flow 3: One horizon (RJ17-5) from Flow 3 was collected at the Church Quarry from the basal portion of the flow, $\sim$ 2 m above the red bole horizon. The samples were collected from the basal columnar jointed region of the flow. There is abundant spheroidal weathering on exposed surfaces, but

samples look unaltered when broken open. Across the Godavari River, one horizon (RJ17-4) was collected from Flow 3 within the Rajahmundry Quarry. RJ17-4 was collected $\sim$ 1 m from the base of the Quarry within the lower part of the core of the flow, $\sim$ 20 m below the contact with the Rajahmundry Formation sandstone.

We performed demagnetization experiments at the Berkeley Geochronology Center (BGC). At least six specimens per horizon were demagnetized. We used a combination of stepwise alternating field (AF) and thermal demagnetization techniques. For stepwise demagnetization, samples underwent alternating field demagnetization using an in-line 2-axis static degausser associated with the 2G-755R cryogenic magnetometer, starting at fields $\sim$ 3 mT and going up to fields of 100 mT, in 3-10 mT steps. Following AF demagnetization, samples underwent two thermal demagnetization steps at temperatures of 80°C and 130°C, to confirm that samples were not biased by a remanence held by goethite. Samples were heated in a non-inductively wound ASC 48 specimen resistance furnace, housed within a magnetically shielded room at the BGC. In addition to stepwise AF demagnetization, we subjected at least one sample per horizon to a stepwise thermal demagnetization protocol. Before heating, samples were treated with low AF fields in steps of $\sim$3 mT from 0-16 mT to remove viscous overprints. Samples were subsequently heated in 13 thermal steps starting at 100°C and ending at 580°C, with step sizes ranging from 100°C to 10°C near the magnetite Curie temperature. Susceptibility was measured after every thermal step to check for alteration. All samples were measured using the 2G-755R cryogenic magnetometer.

We determined the characteristic remanent magnetization (ChRM) directions of samples using linear trends toward the origin on Zijderveld plots using principal component analysis (Kirschvink, 1980). We selected best-fit lines from a minimum of three consecutive demagnetization steps, where the maximum angle of deviation (MAD) was < 20 degrees (most MAD values were $<$10). Best-fit lines were not anchored to the origin so as to not bias directions by unremoved overprints. For one horizon, RJ17-6, we additionally determined ChRM directions using great circle analysis as the demagnetization data lay in a plane between the characteristic remanence and a secondary overprint. We performed data analysis using Demag GUI within the PmagPy software package (Tauxe et al., 2016). We calculated flow means using Fisher statistics (Fisher, 1953). Only samples with directions determined via principal component analysis were used for flow mean calculations. To determine flow means, mean directions were determined at the sample level for each block (taking the Fisher mean of specimen-level results), and these block sample means were combined to determine flow mean directions. All flows passed Watson's test for randomness at the 95% confidence level (Watson, 1956).

In total, we determined ChRM directions for 55 specimens from three flows. Secondary overprints were commonly removed in low AF demagnetization steps (between 3-16 mT) and in thermal steps below 200°C. Secondary directions fall into three groups. A majority of secondary overprints are similar in direction to the present local field and most likely represent a recent viscous overprint. Within site RJ17-6, we observed an additional secondary overprint consistent in direction with the overlying flow direction. This component is held by a phase that has low unblocking temperature (<400°C), but higher coercivity that the ChRM and may be held by a titanomaghemite phase. It is most clearly removed during thermal demagnetization. Lastly, some

samples have spurious random secondary overprints that were likely obtained due to blasting in the quarry, or stray fields during shipping. Characteristic directions were often constrained by 20 mT, or by 200°C. A majority of samples altered during heating and resulted in spurious directions in high-T steps but this did not impede the determination of ChRM directions. This alteration is associated with an increase in susceptibility starting ∼300°C and is most likely associated with low-T oxidation and the presence of titanomaghemite. All specimens were completely demagnetized by 100 mT and 580°C, and do not show evidence of a high-coercivity, high-unblocking phase. Based on the polarity and geochronologic results, we assign Flows 1 and 2 to C29r and Flow 3 to C29n (Fig. 3.3 b, Table 2). Looking at each flow's mean directions, Flow 1 has reverse polarity with a Dec = 158.7° and Inc = 78.6 °. Flow 2 also has reverse polarity with Dec = 162.5° and Inc = 39.1°. Although Flow 1 and Flow 2 both have reverse polarity, their directions do not overlap within 95% confidence intervals, suggesting that some time passed between the eruption of these flows, consistent with the observed deposition of the intertrappean. Flow 2 is more closely associated with the expected direction at that time with Dec = 163.5° and Inc = 49.7° (calculated using the apwp.py function of PmagPy, which is based on the plate reconstruction model from Besse and Courtillot (2002)). Flow 1 is much further from the expected direction and could be interpreted as a transitional field. However, based on its age and the fact that lava flows record a snapshot of the field and not a time-average, it is more likely that Flow 1 is recording a period of spurious secular variation during a stable chron. Flow 3 has normal polarity with Dec = 301.1° and Inc = -43.5°. This direction is similar but does not quite overlap with the expected direction at the time of emplacement of Dec = 343.5° and Inc = -49.8°. Again, this discrepancy is likely due to secular variation. Both samples from Flow 3 (from the Church and Rajahmundry Quarries) overlap in direction within 95% confidence windows, demonstrating that the flow exposed on the eastern side of the Godavari is most likely the same flow as the uppermost flow on the western side of the river . Directions from Flow 2 and Flow 3 do not pass Watson's V reversal test or the McFadden and McElhinny (1990) reversal test. This failure suggests that significant time has passed between the eruption of the two flows and this is consistent with geochronologic analysis.

3.2.3 ^{40}Ar/^{39}Ar Dating

Samples of the three exposed flows were subjected to ^{40}Ar/^{39}Ar analysis of plagioclase separates at the BGC using facilities and methods described by Sprain et al. (2019). We sampled the lowest flow (sample RJ17-1) in 2017 and separated 297-595 μm plagioclase crystals; the middle (RA99.23) and upper (RA99.14) flows were splits (63-125 μm plagioclase crystals) of the same samples analyzed by Knight et al. (2003). In hand sample, plagioclase crystals from all flows were up to ∼300-500 μm, so the grain sizes analyzed for the upper two flows are very likely groundmass plagioclase. A few tens of milligrams of plagioclase from the middle and upper flows were irradiated in the same batch and analyzed in four replicate incremental heating experiments, whereas a similar amount from the lower flow was irradiated separately and analyzed in only two incremental heating experiments (see Table S1 for complete data including J values, and Text S1 for detailed methods).

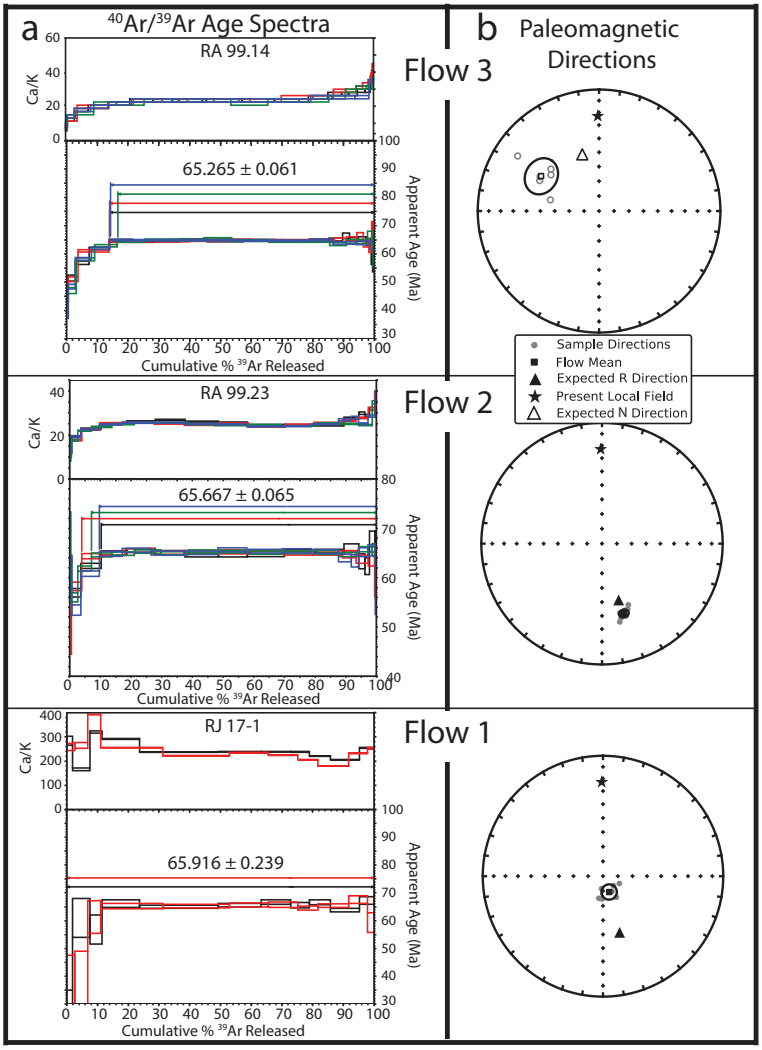

Figure 3.3: **a)** Age spectra for each of the three RT flows. Uncertainties are at the 1σ level and only analytical uncertainty is shown. **b)** Paleomagnetic polarity diagrams for each of the three flows, also indicating the present normal field as well as Cretaceous reverse and Cretaceous normal directions. Open (closed) symbols indicate data plotting in the upper (lower) hemisphere. Note, at the time of eruption, India was in the southern hemisphere.

Table 3.1: Summary of Paleomagnetic Results

Flow ID	Lat (°N)	Long. (°E)	Geo. Dec (°)	Geo. Inc (°)	α95	n
Flow 1	17.0310	81.6345	158.7	78.6	5.2	7
Flow 2	17.0270	81.6141	162.5	39.2	2.9	8
Flow 3	17.0364	81.7146	301.1	-43.5	11.5	6

	k	R	Lat (°)	Lon (°)	Chron
Flow 1	137.6	6.91	-3.5	89.5	C29r
Flow 2	358.1	7.98	-47.2	105.8	C29r
Flow 3	34.7	5.86	18.7	316.5	C29n

Note: Latitude and Longitude are the average Lat/Lon from samples locations of each flow based on the World Geodetic System 1984 (WGS84) datum. Geo. dec/inc indicate declination/inclination of characteristic remanent directions in geographic coordinates determined using Fisher statistics (Fisher, 1953). R is resultant vector; k is the precision parameter; α95 is the 95% confidence interval of the Fisher mean; VGP lat/lon are the latitudes and longitudes of the virtual geomagnetic poles.

Apparent age spectra (Fig. 3.3a) for all samples yielded well-developed and concordant plateaux over >85% of the 39Ar released. The lower flow (RJ17-1) yielded significantly higher and less consistent Ca/K values, >150 for all steps, whereas the middle and upper flows (RA99.23 and RA99.14, respectively) have Ca/K values that vary more consistently throughout the age spectra and are less than 50 in all steps (Fig. 3.3a).

Weighted (by inverse variance) mean plateau ages for the three flows based on our analyses are shown in Table 1. These new results are more precise than those reported by Knight et al. (2003), largely due to more precisely and accurately determined J-values obtained by densely bracketing unknowns with standards during irradiation. The previous results contribute negligibly to weighted mean ages (pooling our new data with those of Knight et al. (2003)), hence we refrain from combining results. Our ages preserve stratigraphic order, although the ages of the lower and middle flows are indistinguishable at the 1σ level. All ages were determined using the optimization model of Renne, Mundil, Balco, Min, and Ludwig (2010) and the calibration of Renne, Balco, Ludwig, Mundil, and Min (2011), and age uncertainties are reported at the 1σ level stated as $\pm$x/y, where x indicates analytical uncertainty and y indicates systematic uncertainty. Corrections were applied for mass discrimination, decay constants, and atmospheric argon (Lee et al., 2006; Renne, Cassata, & Morgan, 2009; Renne & Norman, 2001; Stoenner, Schaeffer, & Katcoff, 1965). Based on these dates, the lower flow (65.916 $\pm$ 0.239/0.245 Ma) postdates the Cretaceous-Paleogene boundary as dated by ^{40}Ar/^{39}Ar at 66.052 $\pm$ 0.008/0.043 Ma (Sprain et al., 2018), although the

Table 3.2: Summary of $^{40}Ar/^{39}Ar$ dates

Flow	Sample	Age (Ma)	$\pm\sigma$ (analytical)	$\pm\sigma$ (systematic)
Upper	RA99.14	65.265	0.061	0.076
Middle	RA99.23	65.667	0.065	0.079
Lower	RJ17-1	65.916	0.239	0.245

dates are not distinguishable at the 1σ level . The poor age precision on this flow is due to its high Ca/K ratio, and we further constrain its chronology relative to the Cretaceous-Paleogene boundary using its geochemical formation assignment. The lower flow date is also not distinguishable with high confidence from the $^{40}Ar/^{39}Ar$ age for the end of geomagnetic polarity chron C29r (65.724 $\pm$0.013/0.044 Ma; Sprain et al. (2018)). At the 95% confidence level, the lower flow could have erupted as much as $\sim$50 ka after the end of chron C29r, but the most probable inference is that it was emplaced in chron C29r, due to its reverse polarity. The date for the middle flow (65.667 $\pm$ 0.065/0.079 Ma) is definitively younger than the Cretaceous-Paleogene boundary (separated by more than 2σ) (Fig. S10). Its reverse polarity constrains it to within chron C29r, and its date is not distinguishable from the chron C29r/C29n boundary at the 1σ level, despite the most likely age falling within C29n. Our age for the upper flow (65.265 $\pm$ 0.061/0.076 Ma) is well within the age span of chron C29n, consistent with its normal polarity (as reported in the Geologic Time Scale 2012; Ogg (2012)). It is noteworthy that the age of the upper flow is younger than any of the dated lava flows in the Western Ghat sequence (Sprain et al., 2019).

3.2.4 Micropaleontology and Biostratigraphy

3.2.4.1 Sampling Procedures and Identification of Foraminifera

For micropaleontological analysis, 17 samples across the carbonate intertrappean unit were collected and studied in the Government Quarry section (Fig. 3.1; see Fig. 3.6 for detailed stratigraphic placement of samples). Because all the samples were very lithified, to extract foraminiferal specimens, we disaggregated around 200 grams per sample, using a solution with 80% acetic acid and 20% H_2O for 4 hours. Samples were dried at $\leq 50^{\circ}$C and then sieved into 38-63 μm and $\leq$63μm size fractions. All specimens were identified, sorted, and fixed on standard 60-square micropaleontological slides. We picked planktic foraminiferal specimens and photographed them under the scanning electron microscopes Zeiss MERLIN FE-SEM at the Electron Microscopy Service of the Universidad de Zaragoza (Spain). They are illustrated in Fig. 3.4. For the biostratigraphic determinations, we have used the biozonations of Berggren and Pearson (2005).

Micropaleontological assemblages of the carbonate intertrappean unit are composed of marine to freshwater taxa, such as charophyte fructifications (gyrogonites), ostracods, gastropods, bivalves, fish teeth, and foraminifers. Planktic/Benthic foraminiferal ratio is very low in all the samples, around 1%. Benthic foraminifera include *Nonion, Cibicides, Dentalina, Protelphidium* and miliolids. These and other genera have been previously reported in this outcrop by Malarkodi, Keller,

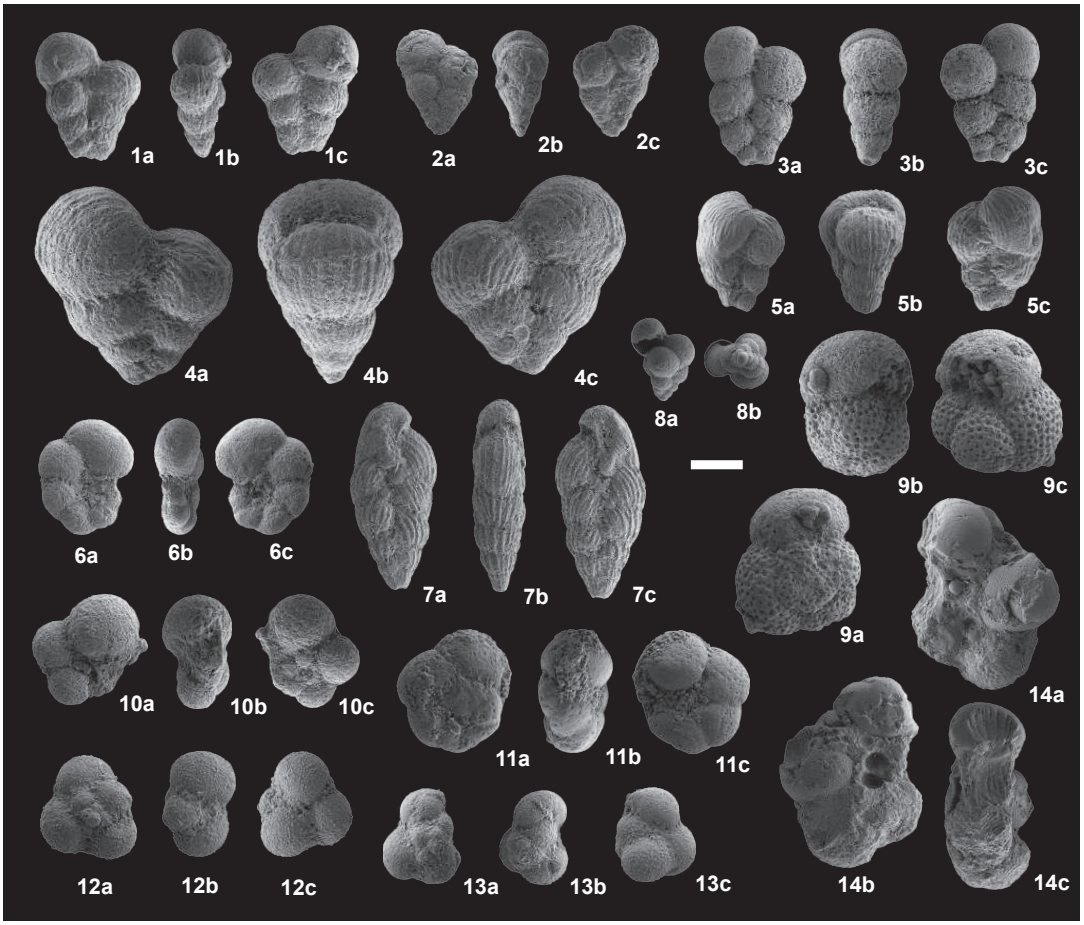

Figure 3.4: SEM images of the planktic foraminiferal specimens identified in the carbonate intertrappean unit of the Government Quarry section (scale bar = 100 μm). 1. *Heterohelix globulosa*, sample GQN3; 2. *Heterohelix globulosa*, sample GQN7; 3. *Heterohelix globulosa*, sample GQN10; 4. *Heterohelix* aff. *globulosa* (transitional to *Heterohelix punctulata*), sample GQN3; 5. *Heterohelix* aff. *globulosa* (transitional to *Heterohelix punctulata*), sample GQN9; 6. *Globigerinelloides rosebudensis*, sample GQN3; 7. *Pseudoguembelina costulata*, sample GQN4; 8. *Guembelitria cretacea*, sample GQN12; 9. *Eoglobigerina trivialis* (with inflated chambers) or *Subbotina triloculinoides* (with the last broken underdeveloped chamber), sample GQN10; 10. *Parasubbotina varianta*, sample GQN13; 11. *Praemurica inconstans*, sample GQN3; 12. *Globoconusa* aff. *daubjergensis*, sample GQN3; 13. *Globoconusa daubjergensis*, sample GQN10; 14. *Parasubbotina pseudobulloides* (internal mold), sample GQN11.

Fayazudeen, and Mallikarjuna (2010), who estimated environments ranging from shallow marine to brackish estuarine based on benthic foraminiferal and ostracode assemblages. The planktic foraminifera are almost absent in our samples, and the preservation of tests is generally very poor. Despite an intensive search, we could only find 14 specimens in the 17 samples studied (specifically in samples GQN3, 4, 7, 10, 11 and 12).

The identified Cretaceous species include *Heterohelix globulosa* (Figs. 3.4.1-3), *Heterohelix* aff. *globulosa* (transitional to *Heterohelix punctulata*; Figs. 3.4.4-5), *Globigerinelloides rosebudensis* (Fig. 3.4.6), *Pseudoguembelina costulata* (Fig. 3.4.7), and probably *Guembelitria cretacea* (Fig. 3.4.8). Among the Danian species, the following stand out: *Eoglobigerina trivialis* or *Subbotina triloculinoides* (Fig. 3.4.9), *Parasubbotina varianta* (Fig. 3.4.10), *Praemurica inconstans* (Fig. 3.4.11), and *Globoconusa* aff. *daubjergensis* (Figs. 3.4.12-13). A probable specimen (internal mold) of *Parasubbotina pseudobulloides* was also found (Fig. 3.4.14). These specimens belong to mixed assemblages of upper Cretaceous and Danian planktic foraminifera, and hence suggest an early Danian age for the carbonate intertrappean unit. Given the mixed assemblage, and that nearshore environments such as these are not inhabited by planktic foraminifera, we conclude the Cretaceous specimens must be considered reworked and that Danian specimens, if *in situ*, had to be transported from open ocean by postmortem displacement of tests due to surface water currents.

3.2.4.2 Biostratigraphic Placement

Indubitable specimens of Danian index-species have not been identified. Nevertheless, although its gross morphology does not fit strictly, the *Eoglobigerina* or *Subbotina* specimen (Fig. 3.4.9) found in GQN10 could belong to *S. triloculinoides*, which is the index-species of Subzone P1b of Berggren and Pearson (2005). Its lowest occurrence is close to the C29r/C29n boundary (Berggren & Pearson, 2005) and, according to Arenillas, Arz, and Molina (2004), in the uppermost part of C29r. The lowest occurrence of *Gc. daubjergensis* is at the Subzone P1a (Arenillas et al., 2004), and its abundance is high in relatively shallow outer neritic environments (Olsson, Berggren, Hemleben, & Huber, 1999), mainly from the Subzone P1b. The identification of specimens closely related to this species (*Gc.* aff. *daubjergensis*) in GQN3 and GQN10 indicates that the carbonate intertrappean unit could belong to Subzone P1a, but more likely to Subzone P1b. No species typical of the Zone Pα, such as *Parvularugoglobigerina eugubina*, and/or Subzone P1c, as *Globanomalina compressa*, have been found in the Government Quarry section.

The triserial specimen identified in GQN12 is poorly preserved but seems to belong to *G. cretacea*. *Guembelitria* might be the only surviving planktic foraminiferal genus of the end-Cretaceous mass extinction (Smit, 1982; Arenillas & Arz, 2017). Nevertheless, the highest occurrence of the genus *Guembelitria* is in the lower part of Zone Pα, as has been recently proposed by Arenillas, Arz, and Gilabert (2018), and it is subsequently replaced by species of the genus *Chiloguembelitria* (Arenillas, Arz, & Gilabert, 2017). If the carbonate intertrappean unit belongs to Subzone P1b, then the *G. cretacea* specimen found in GQN12 is reworked and probably Cretaceous in age.

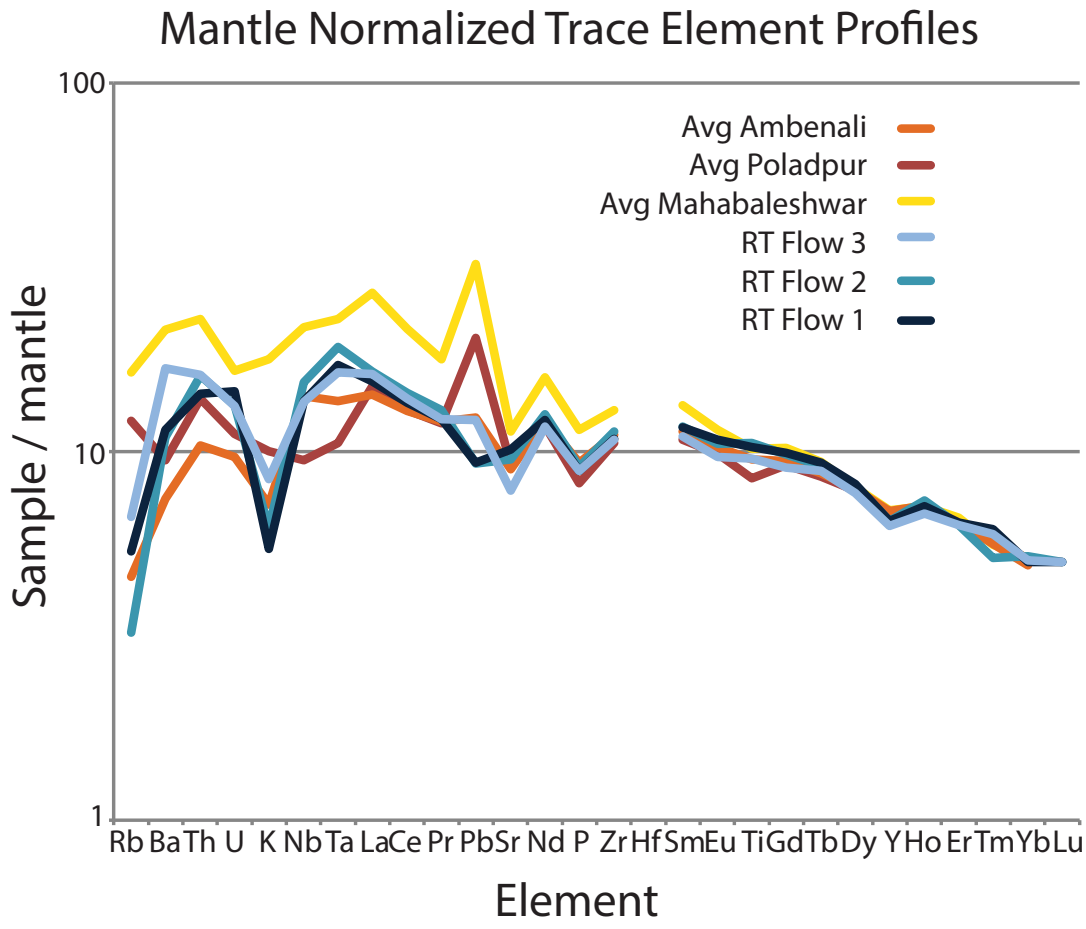

Figure 3.5: Mantle-normalized trace element profiles for each of the three RT flows (geochemical data from Knight et al. 2003) compared with current reference average compositions for the three Deccan formations closest in age to the RT flows: the Ambenali, Mahabaleshwar, and Poladpur Formations (Vanderkluysen et al., 2011). Mantle values are from McDonough and Sun (1995), with a Lu=5 normalization. Note the upper Mahabaleshwar Fm. is more like Ambenali than like average Mahabaleshwar. The upper Mahabaleshwar is not plotted, as a full suite of trace element data is not available.

3.2.5 Geochemistry of RT Basalts and Intertrappean Sediments

Comparison of trace element data from previous studies of RT basalts including identified flows (Knight et al., 2003) with compiled chemical data for the main Deccan province (Vanderkluysen et al., 2011) indicates all of the RT flows are consistent with the Ambenali geochemical formation (Fig. 3.5, McDonough and Sun (1995)), as previous studies have suggested (e.g., Baksi, 2001). However, the upper Mahabaleshwar Formation has previously been noted to have similar chemical characteristics to the Ambenali Formation (Cox & Hawkesworth, 1985; Devey & Lightfoot, 1986). For instance, lower to middle Mahabaleshwar flows have Zr/Nb ratios of 9-10, whereas Ambenali and upper Mahabaleshwar flows have Zr/Nb $\geq$ 11 (Jay, 2005). All three Rajahmundry flows have Zr/Nb $\geq$ 11 (Baksi, 2001; Knight et al., 2003). Therefore, given the uppermost flow's chemistry, normal polarity, and younger age, it is better assigned to the Mahabaleshwar Fm. rather than the Ambenali. The Panhala Formation also has somewhat similar geochemistry and normal polarity, but its known spatial extent is restricted to a relatively small area within the Western Ghats (Lightfoot, Hawkesworth, Devey, Rogers, & Calsteren, 1990). Consequently, it is more likely that RT Flow 3 represents a distal exposure of the Mahabaleshwar Formation. Barium concentration in all three flows is high compared to Western Ghats Ambenali compositions, but this is presumably due to post-eruption interaction with seawater or marine sediments. This is corroborated by a covariation observed between strontium and oxygen isotope composition in Rajahmundry basalt samples, which indicates the strontium composition has been altered by seawater (Baksi, 2001). Baksi (2001) accounted for this relationship, calculating a primary $^{87}Sr/^{86}Sr$ value of 0.7040. This is consistent only with the values expected for the Ambenali and Mahabaleshwar Formations (0.7038-0.7044 and 0.7040-0.7055 respectively, Vanderkluysen et al. (2011)). In summary, Flows 1 and 2 are most consistent with the Ambenali Formation, and Flow 3 with the upper Mahabaleshwar Formation.

We have analyzed the carbon isotope composition ($\delta^{13}C_{\mathrm{VPDB}}$) of the carbonate intertrappean sediments between flows 1 and 2 (Fig. 3.6) in the Government Quarry section. We collected samples from fresh quarry exposures and stored them in plastic bags. In the lab, we drilled each sample to collect powder from carbonate matrix, taking care to avoid large fossils. We determined $\delta^{13}C$ and $\delta^{18}O$ values using a MultiCarb system in line with a GV IsoPrime mass spectrometer in Dual Inlet at the Center for Stable Isotope Biogeochemistry at UC Berkeley. NIST standard 8544 (NBS19) was analyzed (N=3, within 1% of accepted value, standard deviation of 0.025‰), as well as internal standards (N=4, standard deviation of 0.055‰).

The $\delta^{13}C_{\mathrm{VPDB}}$ values of the intertrappean carbonate unit are between 1 and -7‰. Marine carbonates in the Cretaceous and Paleocene have a composition of approximately 0 to 2.5‰, thus the two points (samples GQN 5 and 8) in the interior of the carbonate unit which have $\delta^{13}C$ values within that range are broadly consistent with deposition in a shallow marine environment or near-shore carbonate platform (e.g., Lerman & Clauer, 2014). However, the majority of the unit, especially near the base and top, has more negative $\delta^{13}C$ values of -4 to -7‰, indicating the carbon source may have been the cooling and degassing basalt, which presumably had a composition similar to the mantle (-5 to -7‰) (e.g., Lerman & Clauer, 2014). The top of the intertrappean, which is independently hypothesized to be altered and recrystallized due to the overlying basalt flow (e.g.,

Keller et al., 2008), also has a of $\delta^{13}C$ value of $\sim$-7‰. Overall, it is likely that the carbon isotope composition of the carbonate unit dominantly reflects that of the basalt composition, whether due to post-depositional alteration or composition at time of formation.

3.3 Chronostratigraphy of Rajahmundry Traps

We conclude that all three exposed flows of the Rajahmundry Traps were emplaced in the Danian (Fig. 3.6). The reverse polarity of Flows 1 and 2 require emplacement during chron C29r, and the radioisotopic dates of 65.916 $\pm$ 0.239 Ma and 65.667 $\pm$ 0.065 Ma ($\pm 1\sigma$, analytical) constrain them to post-Cretaceous-Paleogene boundary (66.052 $\pm$ 0.008 Ma, Sprain et al. (2018)) in age. The date for Flow 1 is within uncertainty of the Cretaceous-Paleogene boundary, however its geochemical assignment to the Ambenali Formation also requires post-boundary emplacement (e.g., Schoene et al., 2019; Sprain et al., 2019). This is corroborated by the foraminifera in the carbonate intertrappean, which most closely align to Danian planktic foraminiferal Subzone P1b, consistent with deposition near the C29r/C29n boundary. Flow 3, the uppermost flow, has a normal polarity, and a date of 65.265 $\pm$ 0.061 Ma, both of which are consistent with emplacement within chron C29n.

We can more precisely determine the timing of the lower two flows by combining the new RT $^{40}Ar/^{39}Ar$ dates and paleomagnetic constraints with the date of the C29r/C29n transition from Sprain et al. (2018). The convolution of the magnetic reversal age distribution (65.724 $\pm$ 0.044 Ma, Sprain et al. (2018)) results in ages for Flow 1 of 65.916 $\pm$ 0.210 Ma and for Flow 2 of 65.706 $\pm$ 0.043 Ma (Text S2 and Fig. S8). These ages require that the carbonate intertrappean unit be deposited over a period of $\sim$250 ka at most and the red bole over a period of $\sim$400 ka. While $\sim$2 m is a relatively small amount of alteration and/or sediment accumulation for $\sim$400 ka, the red bole here is thicker than most boles within the Western Ghats (e.g., Widdowson et al., 1997). These ages are consistent with modern $^{40}Ar/^{39}Ar$ dates for the Ambenali and Mahabaleshwar Formations from the main Deccan province (Sprain et al., 2019). The RT have previously been geochemically correlated to these formations (Baksi, 2001; Jay & Widdowson, 2008; Knight et al., 2003; Manikyamba, Ganguly, Santosh, Saha, & Lakshminarayana, 2015). Comparison of RT trace element data with a recent Deccan geochemistry compilation from Vanderkluysen et al. (2011) yields the same result (Fig. 3.5). As the Ambenali-Mahabaleshwar transition is within chron C29r in the MDVP (Vandamme & Courtillot, 1992), our chronostratigraphy - with the lower two flows belonging to the Ambenali Formation and the upper flow to the upper Mahabaleshwar Formation - demonstrates that the RT basalts are compatible with contemporaneous MDVP chemostratigraphy and magnetostratigraphy.

Given this compatibility, we can further constrain the timing of Flow 1 using its assignment to the Ambenali Formation. As Flow 1 cannot be older than the Poladpur to Ambenali composition transition, we convolve the age for Flow 1 with the youngest date for the Poladpur Formation from the Sprain et al. (2019) MDVP chronostratigraphy (65.940 $\pm$ 0.092 Ma). This calculation results in a most likely age for Flow 1 of 65.916 $+0.096$, -0.202 Ma (Fig. S8b). We emphasize that this is dependent on the assumption that the RT basalts are an extension of MDVP flows and that the

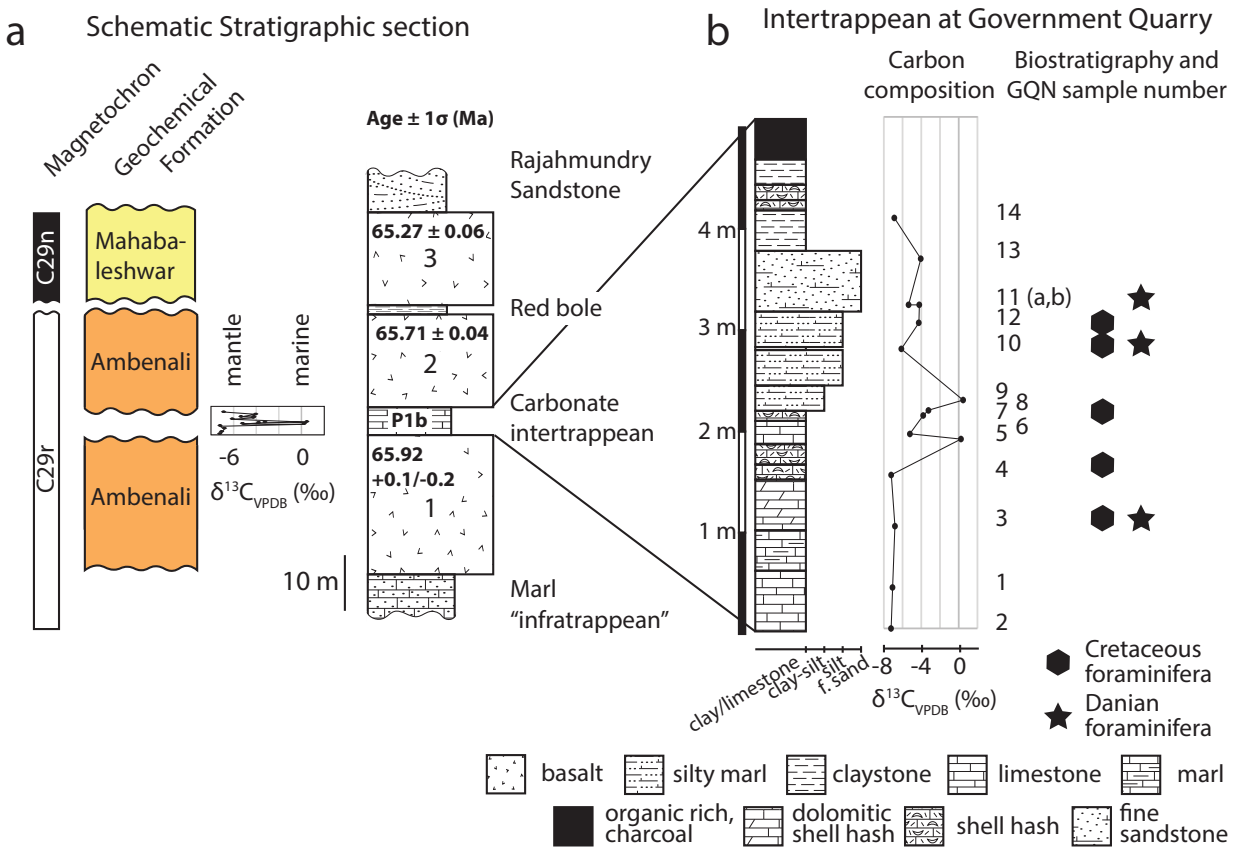

Figure 3.6: **a** Composite stratigraphic section, showing the date, magnetic polarity, biostratigraphy, and geochemical formation for each RT flow. The age shown is the ^{40}Ar/^{39}Ar date, accounting for age constraints from magetostratigraphy and geochemistry (Text S2) **b** Stratigraphic section of the carbonate intertrappean from the Government Quarry site, with expanded $\delta^{13}C_{carb}$ and biostratigraphy, including GQN sample numbers.

geochemical formations are isochronous within the MDVP.

While the exposed flows are most likely all post-Cretaceous-Paleogene boundary in age, analysis of sub-surface cores from near the mouth of the Godavari river (approximately 50 km to the south of the Rajahmundry Traps), suggests the presence of up to 8 similarly sized lava flows from the late Maastrichtian onward (Keller et al., 2011). The exact number of flows varies between cores, presumably because of complex lava flow dynamics resulting in kipukas (areas uncovered by lava) and slightly different paths for each lava flow (e.g., Reynolds, Holford, Schofield, & Ross, 2017). This type of lava flow morphology is frequently due to even slight topographic features in the underlying sediment, and results in variation of flow thickness due to ensuing inflation (Self, Keszthelyi, & Thordarson, 1998).

The age of the subsurface flows has been estimated based on biostratigraphic correlation of intertrappean sediments to planktic foraminiferal zones. The lower 3 or 4 flows have sediments between them within Zone CF1 (Keller et al., 2011, 2012), suggesting deposition within the last 110 ka of the Cretaceous (Coccioni & Premoli Silva, 2015). According to Keller et al. (2011), the upper 3 or 4 flows have intertrappean sediments which correlate to Subzones P1a and P1b of Keller, Li, and MacLeod (1996), which are roughly equivalent respectively to Zone Pα and Subzone P1a of (Berggren & Pearson, 2005). The exposed Rajahmundry Traps flows may correlate with some of these Paleocene flows within the cores, and the regional tilt to the southeast accounts for the 2.5 to 3 km of overlying sediment in the cores. These large lava flows are broadly consistent with the geochronology of the Western Ghats, although there is no geochemical data available for the subsurface flows to correlate them to specific geochemical formations.

3.4 Discussion

3.4.1 Correlation with Deccan Traps Chemostratigraphy and Implications for Rajahmundry Traps Eruptive Vents

The geochemistry of the RT has long been correlated broadly to a mantle plume source, and specifically to the Ambenali and Mahabaleshwar Formations of the Western Ghats (e.g., Baksi, 2001; Manikyamba et al., 2015). All three flows have trace element compositions broadly consistent with the Ambenali Formation (Fig. 3.5). While Flow 3 is significantly younger than the Ambenali Formation in the Western Ghats (e.g., Sprain et al., 2019), the upper Mahabaleshwar Formation has previously been found to have an Ambenali-like trace element composition (e.g., Lightfoot et al., 1990). The youngest date from the upper Mahabaleshwar Formation from the Western Ghats, which is also the youngest high-precision date from the MDVP, is $\sim$65.42 Ma (Sprain et al., 2019). However, as this date is not from the top of the Mahabaleshwar Formation, it is entirely possible the emplacement of the Mahabaleshwar Formation continued for another $\sim$150 ka until the emplacement of Flow 3 at 65.27 Ma. The Panhala Formation, which overlies the Mahabaleshwar Formation, is also geochemically similar to the upper Mahabaleshwar and Ambenali Formations (Lightfoot et al., 1990). Further work to date the boundary of the Mahabaleshwar and Panhala Formation boundary will enable a definitive formation assignment, however Mahabaleshwar is the

more parsimonious choice, as the Panhala Formation is known from only a few places within the Main Deccan Volcanic Province. The new chronostratigraphy for the RT thus suggests that the chemistry of the RT flows is consistent with the contemporaneous Western Ghats geochemical formations.

The robust correlation with main province Deccan geochemistry has long led to the conclusion that the RT basalts erupted from the same vents as the Ambenali and Mahabaleshwar Formations (e.g., Baksi, 2001; Self, Jay, et al., 2008). However, it has also been hypothesized that the RT basalts are the result of local volcanism associated with rifting, although still affiliated with Deccan magma sources (Lakshminarayana et al., 2010; Manikyamba et al., 2015). This hypothesis is driven by potential lack of a clear down-slope pathway between the main Deccan province and Rajahmundry due to tectonic uplift of the Eastern Ghats (Lakshminarayana et al., 2010). We do not think this is likely, as there are no known intrusive magma bodies, sills, or dykes of appropriate age near Rajahmundry despite extensive basement exposures (e.g., Geological Survey of India, 2000a, 2000b). This is in contrast to other Deccan sub-provinces such as the Malwa Plateau, the Mandla Lobe, and the Kutch-Saurashtra region, which each have a large number of dikes compositionally similar to the lava flows (e.g., Vanderkluysen et al., 2011). Furthermore, all three RT flows are at least 20 meters thick, requiring a higher eruptive flux than is typically associated with smaller-scale fissure volcanism (e.g., Deschamps et al., 2014). Thus, the most parsimonious explanation remains that the RT basalts originated from some of the same eruptive centers as the Western Ghats lavas and flowed $\sim$1000 km to the Rajahmundry area, even if their exact path is unknown (Fig. 3.1) (Self, Jay, et al., 2008). By contrast, there are geochemical and volcanological reasons to suspect independent eruptive centers for the other Deccan sub-provinces (e.g., Kale, Dole, Shandilya, & Pande, 2020).

Assuming the RT flows are an extension of the MDVP, the date for Flow 2 requires that large volume flows of Ambenali composition be erupted less than 100 ka prior to the C29r/C29n boundary. This is consistent with the Sprain et al. (2019) geochronologic framework for the Western Ghats, which describes a roughly uniform eruptive rate through the Deccan sequence. However, it is inconsistent with a hiatus of approximately 300 ka between the top of the Ambenali Formation and the C29r/C29n boundary, as suggested by Schoene et al. (2019). This suggests two possibilities: either the Ambenali Formation is not isochronous between the RT and the Western Ghats (and within the Western Ghats), or the hiatus inferred by Schoene et al. (2019) is not uniform throughout the Main Deccan Volcanic Province. The RT chronology cannot resolve this in isolation; however, the consistency with the dates from the Sprain et al. (2019) chronology supports the latter.

3.4.2 Timing of Rajahmundry Flows With Respect to Cretaceous-Paleogene Mass Extinction and Danian Climate Change

Flood basalt eruptions have the potential to cause climate change due to emission of SO_2 and CO_2 (e.g., Schmidt et al., 2016; Self et al., 2006). Our chronostratigraphy of the Rajahmundry Traps shows that the three exposed flows were emplaced after the Cretaceous-Paleogene boundary and are therefore unrelated to the mass extinction, regardless of any potential climate consequences

(Fig. 3.6). However, it confirms that large volume Deccan eruptions were occurring well into the Danian. It is therefore important to address whether these eruptions could have caused climate change and therefore perturbed ecosystems during the recovery interval.

Ecological community stability was highly variable for the first ∼700 ka of the Paleocene, until ∼65.3 Ma (e.g., S. A. Alvarez et al., 2019; Birch, Coxall, Pearson, Kroon, & Schmidt, 2016; Smith et al., 2018). There are several periods of climate change during this time interval, including the Danian-C2 (Dan-C2) and lower-C29n hyperthermal events (Coccioni et al., 2010; Dinarès-Turell, Westerhold, Pujalte, Röhl, & Kroon, 2014). The former is a double-peaked warming event, with total duration of approximately 100 ka and which terminated at the C29r/C29n transition, while the latter occurred approximately ∼100 ka later at ∼65.6 Ma, near the base of chron C29n (Coccioni et al., 2010, 2012; Dinarès-Turell et al., 2014; Sinnesael et al., 2019). Both are associated with small decreases (<1‰) in benthic carbon isotope composition, although the global nature of both events is debated (e.g., Barnet et al., 2019; Sinnesael et al., 2019). The RT flows all occurred within this 700-ka period of highest amplitude variability in community stability. Furthermore, Flows 1 and 2 were erupted around the same time as the Dan-C2 hyperthermal event (Fig. 3.7).

To test whether the eruptive CO_2 emissions of these voluminous flows could have directly caused observable warming, we estimated the effects of these emissions on the atmosphere and ocean. To do this, we used scaling relationships from an intermediate complexity Earth system model, LOSCAR (Zeebe, 2012), to estimate the peak changes in atmospheric carbon (pCO_2) and temperature as a response to volcanogenic CO_2 input forcing (Towles, Olson, & Gnanadesikan, 2015). The LOSCAR model has been used previously to model the climate effects of Deccan Traps and North Atlantic Igneous Province CO_2 emissions (e.g., Hull et al., 2020; Zeebe, 2012).

The volcanogenic CO_2 input forcing is parameterized as a triangular shaped emission history with a specified duration and total amount emitted (Towles et al., 2015). We relate the CO_2 emissions to a volume of erupted basalt using an estimated Deccan basalt CO_2 content of 0.5 weight percent, or 14 Tg CO_2 per km^3 (e.g., Capriolo et al., 2020; Self et al., 2006). We used the change in atmospheric pCO_2 for each emissions history to calculate the consequent change in atmospheric temperature using a given equilibrium climate sensitivity (°C per pCO_2 doubling, see Zeebe (2012) Equation 51). We then estimated the temperature change in the deep ocean using the scaling relationship between atmospheric and ocean temperature changes for a given emission scenario from Towles et al. (2015). This process enabled us to estimate the temperature change in the deep ocean caused by volcanic CO_2 emissions for a variety of eruption sizes and durations. We can also assess the roles of different initial atmospheric pCO_2 concentrations and equilibrium climate sensitivity values. In the early Paleocene, background pCO_2 is estimated to be ∼300-600 ppm (Milligan, Royer, Franks, Upchurch, & McKee, 2019), and equilibrium climate sensitivity in the ice-free early Paleocene is estimated to be 3°C per pCO_2 doubling (Royer, 2016).

We find that it is difficult to cause $\geq$ 2°C warming with the volcanogenic CO_2 emissions expected for a Rajahmundry-scale Deccan eruption (∼5000 km^3), even given a sensitive set of initial conditions. Using a low initial pCO_2 concentration of 300 ppm and a high climate sensitivity of 4 °C per pCO_2 doubling, 2°C of warming corresponds with ∼100,000 km^3 basalt erupted within at most a few (1-3) thousand years (Fig. 3.8 a). An eruptive pulse of this size shortly before the

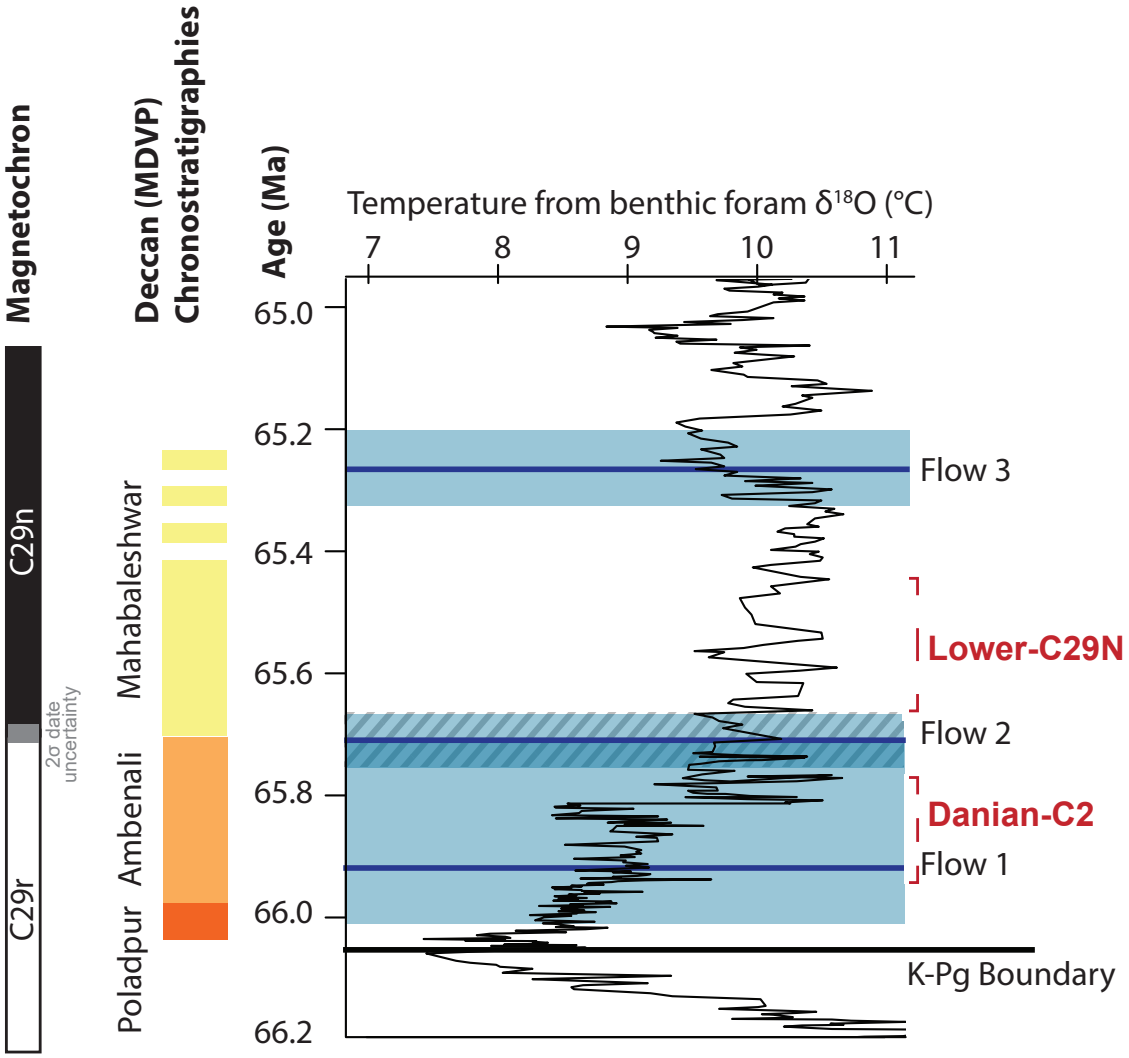

Figure 3.7: The age (with 1σ uncertainty shaded) of each RT flow plotted with deep ocean temperature from J. Barnet et al. (2019), as well as magnetostratigraphy and Deccan chronostratigraphy. The approximate age range of the Danian-C2 and Lower-C29n hyperthermals based on constraints from J. Barnet et al. (2019), Coccioni et al. (2010), and Sinnesaelet al. (2019). Magnetostratigraphy is from Sprain et al. (2018), and the timescale for the temperature record is adjusted so the C29r/C29n boundary is isochronous through all data presented (Text S3). Deccan chronostratigraphy is from Sprain et al. (2019), combined with magnetostratigraphic constraints (Text S2). Top of the solid Mahabaleshwar bar is placed at the youngest date for the Mahabaleshwar Fm (Sprain et al. 2019), although the top of the formation remains undated.

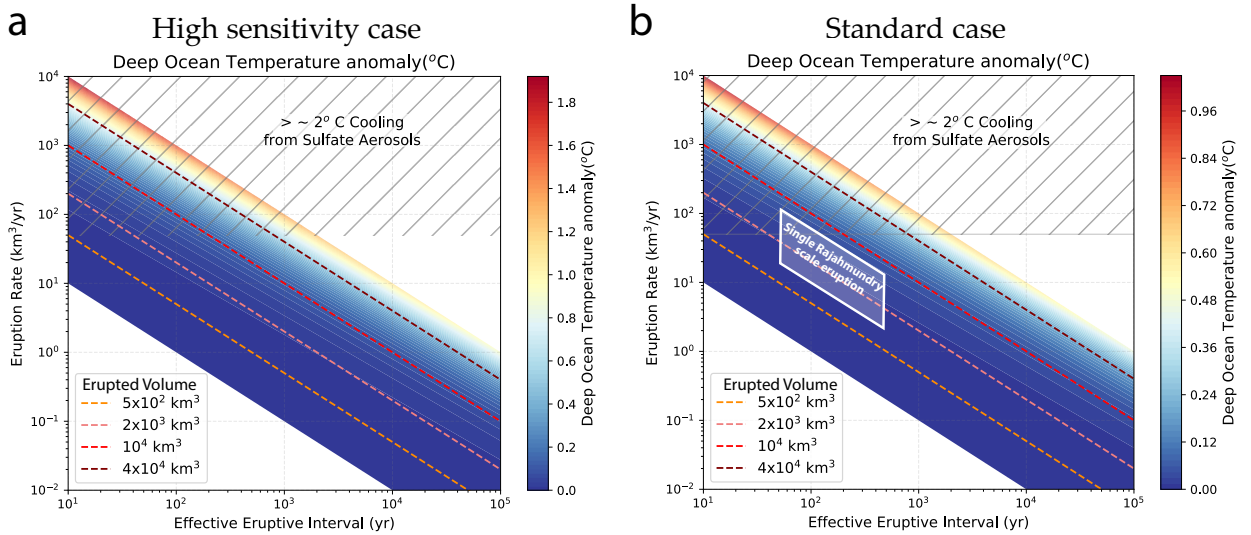

Figure 3.8: The peak warming observed in the deep ocean for varying volcanogenic CO_2 emission rates and durations. The temperatures were calculated using emissions to temperature scaling from Towles et al. (2015) for the LOSCAR carbon cycle model (Zeebe, 2012).. We assume volcanic emissions of 14 Tg CO_2 per km^3 basalt (equivalent to 0.5% CO_2 by weight, Self et al., 2006). The eruption rates for which sulfate aerosol driven cooling is expected to exceed 2°C is from Schmidt et al. (2016). In **a** we utilize the most sensitive initial conditions: a low initial pCO_2 concentration of 300 ppm, and a high equilibrium climate sensitivity of 4°C per CO_2 doubling. In **b**, we use reasonable estimates for the early Paleocene as most likely conditions: an initial pCO_2 of 450 ppm and an equilibrium climate sensitivity of 3 C per CO_2 doubling. The best estimates for an individual Rajahmundry-scale large eruption ($\sim$1000-6000 km^3 in 50-500 years) are indicated with a white parallelogram.

chron C29r/C29n boundary is inconsistent with both proposed Deccan age models for the Main Deccan Volcanic Province (Schoene et al., 2019; Sprain et al., 2019). For reference, this volume is much larger than the total volume of each of the other Deccan sub-provinces (e.g., Malwa Plateau $\sim$ 21,000 km^3, (Schöbel, de Wall, Ganerød, Pandit, & Rolf, 2014)). The required eruptive rate is also much higher than the estimates of 10 km^3/year during the pulses described in the Schoene et al. (2019) age model. Hence, magmatic CO_2 emissions associated with RT flow eruptions, or any other individual Deccan eruption, are unlikely to have directly caused significant climate warming, including the Dan-C2 and Lower-C29n warming events.

Utilizing more standard initial conditions (an initial pCO_2 of 450 ppm and climate sensitivity of 3°C per pCO_2 doubling), we expect each RT eruption to have instead caused $\sim$0.1-0.2°C of warming (Fig. 3.8 b). The extent of warming depends on the duration of each eruption, which we estimate is 50-500 years for the Deccan Traps (Fendley et al., 2019). Additionally, the upper estimate of eruptive rates suggests RT eruptions potentially caused volcanogenic sulfate aerosol

driven cooling of greater than 2°C (Fig. 3.8) (Schmidt et al., 2016; Self et al., 2006). However, given the short lifetime of sulfate aerosols in the atmosphere, this cooling would persist only during the active eruption, while elevated CO_2 could last for thousands of years (e.g., Black et al., 2018; Schmidt et al., 2016). The short duration of volcanogenic cooling means it is unlikely to be recorded in paleoclimate records of $\sim$1000-year resolution (e.g., Barnet et al., 2019; Black et al., 2018).

Other warming events typically associated with the Deccan Traps, such as the Late Maastrichtian Warming Event, also have an amplitude of warming much greater than expected based on the erupted volume of basalt (e.g., Hull et al., 2020; Sprain et al., 2019). This suggests that that the climate impact of the RT flows, and other Deccan eruptions, was potentially amplified by environmental feedbacks. For instance, the Dan-C2 event has been hypothesized to be a combined consequence of Deccan CO_2 emissions and the first 405-ka eccentricity maximum of the Paleocene (Barnet et al., 2019; Sinnesael et al., 2019). Additionally, perturbations to large carbon reservoirs, such as the ocean and terrestrial environments ($\sim$60 and $\sim$10 times more carbon than in the atmosphere respectively), can significantly affect atmospheric CO_2 concentration (e.g., Friedlingstein et al., 2019). Large volcanic eruptions can cause significant changes to these reservoirs through changes in ocean circulation and global precipitation (e.g., Black et al., 2018). These processes are challenging to parametrize and are not explicitly included in the LOSCAR model (Zeebe, 2012). Finally, the observed warming only lasts for less than 100 ka - too rapid for simple silicate weathering feedbacks to remove the added volcanogenic CO_2 from the atmosphere, even with enhanced basalt weathering (e.g., Hull et al., 2020). This suggests other environmental feedbacks may be involved in these brief hyperthermal events.

Additionally, measurements of CO_2 emissions from modern volcanic systems show that the passive (fumarolic, vent, and soil) degassing of CO_2 from intrusive magma bodies is significantly greater in magnitude ($\sim$100 x) than the amount of CO_2 released during eruptions (e.g., Fischer & Aiuppa, 2020; Mittal & Richards, 2019). If this is the case for the Deccan volcanic system, then the total quantity of CO_2 emitted may be much larger than estimated from erupted volume alone. As the total Deccan eruptive interval lasted for $\sim$ 1 Ma (e.g., Sprain et al., 2019), one may not expect a strong time dependence between the passively degassed CO_2 and the emplacement of the RT flows. However, a highly active magmatic system producing highly voluminous lava flows will likely also emplace large amounts of magma in the middle and upper crust. This process may consequently increase passive degassing concomitant with the RT eruptions.

In summary, we cannot conclusively determine if the RT eruptions caused global climate change. However, we can clearly show that eruptive CO_2 emissions were insufficient to directly cause multi-degree warming. Nevertheless, the relative timing of the RT flows suggests the Deccan Traps may have influenced marine and terrestrial ecological recovery, whether through climate change or other environmental effects (e.g., Lyson et al., 2019; Smith et al., 2018).

3.5 Conclusions

We have described a new chronostratigraphy for the exposed portion of the Rajahmundry Traps. These three Deccan lava flows are located approximately 400 km from any other known Deccan outcrop (Baksi, 2001), and nearly 1000 km to the east of the main Deccan eruptive centers in the Western Ghats. The great distance between these basalts and their hypothesized eruptive vents has led to their description as the distal ends of the longest known lava flows on Earth (Self, Jay, et al., 2008). New $^{40}Ar/^{39}Ar$ dates, magnetostratigraphy, and biostratigraphy demonstrate that all three flows exposed were emplaced in the Danian, significantly after the end-Cretaceous mass extinction. Both of the lower two flows were erupted within magnetochron C29r, with the middle flow close to the C29r/C29n transition. The uppermost flow was emplaced several hundred thousand years later, in C29n.

Our results are consistent with previous studies which place the Rajahmundry flows near the chron C29r/C29n boundary (e.g., Baksi, 2001; Knight et al., 2003). If these flows are derived from the MDVP, Flow 3 is the youngest recently dated Deccan lava flow (at 65.27 Ma), indicating that the Deccan Traps were erupting large volumes of basalt more than 700 thousand years into the Paleocene. The RT chronology confirms that the RT flows are coeval and geochemically consistent with the Western Ghats Ambenali and Mahabaleshwar chemostratigraphic formations. The middle RT flow's date, geochemistry, and magnetic polarity requires Ambenali-composition basalt to be erupted just prior to the C29n/C29r boundary. This is inconsistent with the last Ambenali composition flows erupting nearly 300 thousand years prior to the chron boundary, as has been proposed (Schoene et al., 2019). The RT chronology therefore implies that this hiatus is not uniformly present through the entire Deccan Traps, or that the Ambenali Fm. is not an isochronous unit. Resolving this inconsistency and verifying the synchronicity of the geochemical formations are thus priorities for future work.

As the timing of these flows suggests possible implications for ecological recovery, we test whether these large volume eruptions could have caused observable warming. Utilizing an intermediate complexity carbon cycle model (LOSCAR), we clearly show that eruptive CO_2 emissions were insufficient to directly cause multi-degree warming. However, environmental feedbacks (e.g., astronomical forcing) and/or non-eruptive volcanic CO_2 emissions may increase the climatic effects of the voluminous RT flows. If so, the timing of these flows suggests any disturbance may have impacted the protracted ecological recovery from the end-Cretaceous mass extinction.

3.6 Data Availability

Data tables for $^{40}Ar/^{39}Ar$ (Table S1), paleomagnetic analyses (Table S2), and carbon isotope analyses (Table S3) are available at https://doi.org/10.6084/m9.figshare.12168501.v2. Additional supplemental material is available as a file with the published version at https://doi.org/10.1029/2020GC009149. This includes images of the field sites and additional text describing the methods for Ar/Ar geochronology, convolution of magnetic reversal boundaries with dates, and age model adjustments for the Barnet et al. (2019) record.

Chapter 4

Carbon cycle recovery after the Cretaceous-Paleogene extinction: a terrestrial perspective

4.1 Introduction

The Cretaceous-Paleogene (K-Pg) mass extinction occurred $\sim$ 66 million years ago, culminating in the extinction of all non-avian dinosaurs, as well as 75% of species overall (e.g., Raup & Sepkoski, 1982). A key feature of the K-Pg extinction in the geological record is a significant perturbation in the carbon cycle, represented by a negative carbon isotope excursion in many marine records (e.g., Barnet et al., 2017; Birch et al., 2016; Esmeray-Senlet et al., 2015). The K-Pg boundary is synchronous with the Chicxulub bolide impact, which is demarcated worldwide by an iridium anomaly hosted within an impact clay layer (L. W. Alvarez, Alvarez, Asaro, & Michel, 1980). During this time interval, the Deccan Traps Large Igneous Province eruptions also released climate-altering amounts of carbon dioxide and other gases (e.g., SO_2) (e.g., Self et al., 2006; Sprain et al., 2019). The complex series of environmental and carbon cycle changes during the K/Pg mass extinction and recovery time interval is thus hypothesized to be a result of a combination of the Chicxulub impact and the Deccan Traps (e.g., L. W. Alvarez et al., 1980; Hull et al., 2020). However, each event's exact role in the mass extinction and recovery is still debated (e.g., Hull et al., 2020). One crucial part of assessing each event's relative significance is an investigation of the carbon cycle, since the carbon cycle integrates over many important ecological and environmental processes. As the mass extinction is a substantial perturbation, we need to carefully test the underlying assumptions in our conceptual understanding of the carbon cycle and evaluate whether they hold during this event.

The global carbon cycle comprises carbon fixation and respiration by terrestrial and marine plant and animal life, as well as abiotic sources and sinks of carbon, including volcanism, weathering, and inorganic and organic carbon burial (e.g., Friedlingstein et al., 2019). The carbon cycle is balanced between the terrestrial, atmosphere, and marine reservoirs, with each acting as a source

and a receptor for large fluxes of carbon of varying isotope compositions. Relatively small changes in this balance can significantly affect the environment and climate (e.g., atmospheric pCO_2). Changing the carbon cycle fluxes also affects the carbon isotope composition of each reservoir because different carbon species have different isotopic compositions ($\delta^{13}C$, in ‰). For instance, organic carbon is tens of ‰ lighter than inorganic carbon (carbonate) (e.g., Lerman & Clauer, 2014). A decrease in primary productivity and thus organic carbon fixation will decrease the amount of light organic carbon removed from the atmosphere or ocean, causing a lower $\delta^{13}C$ in these reservoirs. The relative mass of each reservoir and inter-reservoir fluxes control how quickly each reservoir responds to external environmental perturbations.

Among the three main carbon reservoirs (atmosphere, ocean, land), the atmosphere is the smallest with the sum of its fluxes from the marine and terrestrial reservoirs equivalent to 25% of the total atmospheric reservoir mass. The size of the atmospheric carbon reservoir controls the concentration of carbon dioxide in the atmosphere (pCO_2). Thus changes in this reservoir directly affect the global temperature and climate. As the atmosphere responds quickly to carbon cycle perturbations due to its small reservoir size, the fluxes of carbon between terrestrial or marine environments and the atmosphere quickly influence and respond to changes in pCO_2 and climate.

Fluctuations in terrestrial and marine organic carbon fixation (via primary productivity) change how much isotopically lighter organic carbon is added to or removed from the atmosphere, and hence alter the carbon isotope composition of the atmosphere ($\delta^{13}C_{CO_2}$). A decrease in primary productivity, such as during a mass extinction, would correspond to a decrease in atmosphere $\delta^{13}C_{CO_2}$. As primary productivity increased again, so too would atmosphere $\delta^{13}C_{CO_2}$. Similarly, the atmosphere will respond to changes in the amount of carbonate precipitation in the ocean (via the marine reservoir). As carbonate is generally isotopically heavier than the atmosphere, changing these fluxes has the reverse effect, i.e., a decrease in carbonate precipitation would cause an increase in atmosphere $\delta^{13}C_{CO_2}$. Atmospheric $\delta^{13}C_{CO_2}$is also affected by geogenic sources of carbon, such as volcanogenic CO_2 emissions. Thus, atmospheric $\delta^{13}C_{CO_2}$ is an integrated signal of volcanogenic CO_2, primary productivity, marine carbonate precipitation, and other carbon cycle processes, and is consequently an important constraint when evaluating the mechanisms of environmental change (e.g., Hull et al., 2020; Tipple, Meyers, & Pagani, 2010).

Unfortunately, it is impossible to directly measure atmospheric composition in the geologic past beyond the ice core bubble record and in rare cases such as bubbles in evaporites. Instead, carbon isotope composition of marine carbonates, usually benthic foraminifera ($\delta^{13}C_{cc}$), is used to estimate atmospheric carbon isotope composition (e.g., Tipple et al., 2010; Barral, Gomez, Legendre, & Lécuyer, 2017). This is based on assuming isotopic near-equilibrium between the marine and atmosphere reservoirs, with constant corrections for disequilibrium processes and export productivity between the surface and deep ocean. Additional constraints come from terrestrial carbon isotope records from either organic material ($\delta^{13}C_{org}$) or pedogenic carbonate nodules (e.g., Arens & Jahren, 2000; Huang, Retallack, Wang, & Huang, 2013). Terrestrial organic material is generally buried plant tissue; hence the carbon represents photosynthetically fixed atmospheric CO_2. This direct assimilation (without intermediate pools such as marine dissolved inorganic carbon) is a key strength of the terrestrial proxy. However, this record does have the added complexity

that environmental parameters such as pCO_2 and hydroclimate can affect photosynthetic carbon isotope discrimination. In general, terrestrial and marine carbon isotope records agree on timing and duration of excursions in the Paleogene, although the amplitude is sometimes greater in the terrestrial records (Abels et al., 2012). This difference has been attributed to coeval increases in pCO_2 and hence photosynthetic carbon isotope discrimination (Abels et al., 2012; Schubert & Jahren, 2012, 2013).

The trends in the terrestrial and marine carbon isotope records are very different across the K-Pg boundary. In the marine realm, the abrupt biotic extinction in the marine realm coincides with a sharp decrease in carbon isotope composition ($\sim$ 2 ‰) in planktonic foraminifera and bulk marine carbonate records. This negative excursion is attributed to a decline in export productivity in the surface ocean, which partially collapsed the biological pump, eliminating the surface to deep carbon isotope gradient (e.g., Birch et al., 2016). The complete recovery of the biological pump and carbon isotope gradient $\sim$1.8 Ma later reflects the recovery of surface marine ecosystems and productivity after the extinction (Esmeray-Senlet et al., 2015; Birch et al., 2016). These marine bulk carbonate carbon isotope records are key to our understanding of the K-Pg extinction and recovery within the marine realm. However, it is not clear that all atmospheric carbon isotope changes will be discernible in marine records due to the complex export productivity changes. Moreover, the carbon isotope excursions recorded in marine carbonate records have different durations and amplitudes, as the export productivity changes are heterogeneous throughout the ocean (Hull & Norris, 2011; Sepúlveda et al., 2019).

Terrestrial carbon isotope records are an important additional constraint on atmospheric composition during this time period. As opposed to marine records, existing terrestrial $\delta^{13}\mathrm{C}$ records have been interpreted as only containing a brief negative $\sim$ 2 ‰ excursion which lasts $\leq$ 5 - 10 ka (Arens & Jahren, 2000; Arens et al., 2014) . The brevity of the excursion in the terrestrial realm has led to the hypothesis that atmospheric $\delta^{13}\mathrm{C}_{CO_2}$ rebounded to Maastrichtian values almost immediately after the K-Pg boundary, reflecting a rapid recovery in global primary productivity and hence burial of organic carbon (e.g., Renne et al., 2013). As neither benthic nor bulk marine $\delta^{13}\mathrm{C}_{cc}$ records return to pre-boundary values this rapidly, this hypothesis requires significant disequilibrium somewhere between marine carbonates, the atmosphere, and terrestrial plants (Arens & Jahren, 2000).

This disequilibrium presents a significant challenge for our understanding of carbon cycle dynamics, particularly within conceptual and computational models used to evaluate environmental change across the K-Pg extinction and recovery. This is because models generally require equilibrium between the marine and atmospheric pools and imply equilibrium with the terrestrial pool as well (e.g., LOSCAR, Zeebe, 2012). Changes in the concentration of dissolved inorganic carbon (DIC) and the smaller reservoir of marine organic carbon, are intrinsically linked with environmental parameters such as ocean pH and marine primary productivity, while processes like terrestrial carbon fixation and burial are generally not explicitly modeled. For example, LOSCAR parameterizes atmosphere $\delta^{13}\mathrm{C}_{CO_2}$ as being a constant offset from $\delta^{13}\mathrm{C}_{DIC}$. If the reservoirs are in equilibrium, fluctuations in terrestrial organic carbon burial will affect the atmosphere $\delta^{13}\mathrm{C}_{CO_2}$, and hence are also reflected in the composition of marine DIC and carbonates (e.g., Komar &

Zeebe, 2017). However, if the terrestrial, marine, and atmosphere reservoirs are not in equilibrium, the model analyses may present an incomplete or biased picture.

This potentially incomplete understanding is particularly important for the K-Pg interval, as the primary productivity in terrestrial environments may be dramatically reduced during the mass extinction. These primary productivity changes can significantly and rapidly ($\sim$ 1000 years) affect the size of the terrestrial reservoir, as the terrestrial reservoir is small and $\sim$ 5-10% of the reservoir mass is exchanged annually according to modern global carbon budgets (Friedlingstein et al., 2019). Although the modern terrestrial reservoir is $\sim$10 times smaller than the marine reservoir (which is mostly DIC), $\sim$1.3 times more carbon is exchanged yearly between the atmosphere and terrestrial reservoirs than between the atmosphere and ocean reservoirs (Friedlingstein et al., 2019). Consequently, fluctuations in productivity and organic carbon burial will both affect and respond to changes in atmospheric pCO_2, and will be reflected in atmosphere $\delta^{13}C_{CO_2}$ (e.g., Hein, Usman, Eglinton, Haghipour, & Galy, 2020; Komar & Zeebe, 2017).

These changes are almost entirely excluded from our current understanding, including models of environmental changes, across the K-Pg extinction and recovery (e.g., Hull et al., 2020; Keller et al., 2018). This is in part because our understanding of the terrestrial record remains incomplete, due to several problems with existing terrestrial $\delta^{13}C_{org}$ records. In particular, the lack of high-resolution chronologic constraints is a significant issue. There are multiple terrestrial organic and carbonate carbon isotope records across the K-Pg boundary, especially from the Williston Basin in North America. However, the primary stratigraphic age control in these sections is typically the K-Pg boundary, identified via Ir-anomaly or palynology. Consequently, it is difficult to assess and compare the relationship between these records and those in the marine realm, (e.g., Arens & Jahren, 2000, 2002; Therrien, Eberth, Braman, & Zelenitsky, 2007; Gilmour et al., 2013; Arens et al., 2014; Jerrett, Price, Grimes, & Dawson, 2015). Additionally, most of these terrestrial records span at most a few tens of meters of stratigraphy. Based on chronostratigraphic constraints from Renne et al. (2013) and Sprain et al. (2015, 2018), these records likely extended at most tens to a few hundreds of thousands of years post-extinction. Therefore, the interval which corresponds to most of the long recovery interval in $\delta^{13}C_{cc}$ is mostly unknown from the terrestrial $\delta^{13}C_{org}$ record. Moreover, the proposed terrestrial excursion is generally neither statistically significant nor unique (Grandpre et al., 2013).

It is necessary to reexamine terrestrial carbon isotope composition across the K-Pg mass extinction and into the Paleocene to understand atmospheric carbon isotope composition across the extinction and carbon cycle recovery interval. To do this, we create and examine a new high-resolution terrestrial $\delta^{13}C_{org}$ record over a $\sim$ 1.5 million year period spanning the extinction event, from 66.4 to 64.8 Ma, with robust geochronologic constraints. Our new record is the first long-duration high-resolution record of terrestrial $\delta^{13}C_{org}$ which extends through both the late Maastrichtian and the first $\sim$1 million years of ecological and carbon cycle recovery.

In order to assess changes in $\delta^{13}C_{CO_2}$, we first compile all existing long-duration ($\geq$ 100 ka) terrestrial $\delta^{13}C$ records from this time interval and identify consistent features. We then compare the terrestrial record to marine bulk and benthic carbonate carbon isotope composition from open ocean marine records from IODP 1262 and 1209 (Walvis Ridge and Shatsky Rise) and a shelf

marine $\delta^{13}C_{cc}$ record from Gubbio (Barnet et al., 2019; Hull et al., 2020; Sinnesael et al., 2019). Terrestrial $\delta^{13}C_{org}$ records are also affected by changes in atmospheric CO_2 concentration (pCO_2), and hydroclimate, because plant carbon isotope discrimination can respond to these conditions. To assess the role of these environmental conditions, we use models to calculate the required pCO_2 or precipitation changes to cause the observed differences between the terrestrial $\delta^{13}C_{org}$ and marine $\delta^{13}C_{cc}$ records (e.g., Kohn, 2010; Schubert & Jahren, 2013). We compare these estimates to a compilation of existing pCO_2 records with robust chronologic constraints. Finally, we suggest the most likely trends in atmosphere $\delta^{13}C_{CO_2}$ and assess the implications for the global carbon cycle during this tumultuous period of Earth history.

4.2 Geologic Setting

The Hell Creek and Tullock Member of the Fort Union formations in the NE Montana part of the Williston Basin are some of the best-studied terrestrial Cretaceous-Paleogene boundary sections worldwide, including a chronostratigraphic framework with both magnetostratigraphy and radioisotopically dated volcanic tephra layers (Fastovsky & Bercovici, 2016; Sprain et al., 2015, 2018). The Cretaceous-Paleogene boundary in northeastern Montana comprises an impact ejecta claystone and iridium anomaly within the "Iridium Z" (or IrZ) coal seam, in addition to being marked by an extinction event in terrestrial flora and fauna (L. W. Alvarez, 1983). A volcanic tephra layer within a few centimeters of the claystone (known as the Nirvana bentonite) has been radioisotopically dated in several sites yielding a pooled date of 66.052 $\pm$ 0.008 Ma (Sprain et al., 2018). The formational boundary between the Hell Creek and Fort Union is approximately, though not precisely, coincident with the K-Pg boundary (e.g., Fastovsky & Bercovici, 2016).

In this region, the chronostratigraphy comprises named coal seams with dated tephra layers within them. These coals are (from oldest to youngest) the Null, IrZ, MCZ, HFZ, Y, X, W, V, and U. This study's age model is based on the ages of all these coals excluding the X and V. While each of these coals is not always laterally continuous, we utilize dates from tephras which have in most cases been chemically correlated using Pb isotopes or ages (Ickert et al., 2015; Sprain et al., 2015, 2018). All the studied localities are composed of fluvial and floodplain deposits, mainly claystones to siltstones with occasional crossbedded sandstones and lignite seams. To minimize chronostratigraphic uncertainty, we have chosen localities over a relatively small geographic area, close to sites with absolute chronology, (Fig. 4.1, Table 4.1) and with as few sandstone channel deposits as possible, as they may scour into underlying sediments.

4.2.1 Site Descriptions

Iridium Hill Annex and Nirvana: For detailed descriptions, please see Chapter 1.

Biscuit Basin: Magnetostratigraphy from LeCain, Clyde, Wilson, and Riedel (2014), radioisotopic dates from Sprain et al., (2015). Biscuit Butte, the highest point of Biscuit Basin, contains dated U, V, and W coals as well as the chrons C29n/C28r and C28r/C28n magnetic reversals (LeCain et al., 2014; Sprain et al., 2015). Biscuit Basin lies to the northwest of Biscuit Butte and

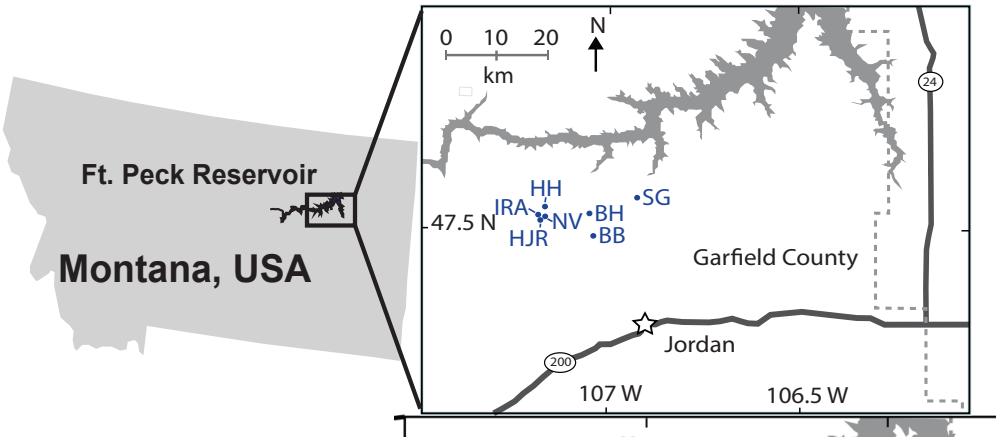

Figure 4.1: Map of Williston basin localities. IRA: Iridium Hill Annex, HH: Hell Hollow, NV: Nirvana, HJR: Herpijunk Rise, BH: Bone Hollow, BB: Biscuit Butte/Basin, SG: Smurphy's Guess

contains outcroppings of the W and Y coals. The stratigraphy between the U and W coals is clear. However, the slope becomes shallower and persistent vegetation makes sampling difficult towards the base of the section. The Y coal and a few meters of section above are exposed in several gullies. The Y coal contains a 6 cm thick tephra layer in this location, the presence of which enables its correlation to the upper Y coal at the nearby Garbani locality, which also has an unusually thick tephra layer dated by Sprain et al., (2015).

Hell Hollow: The Hell Hollow locality is approximately 2 km to the NE from Nirvana butte, and also nearby the Iridium Hill Annex and Herpijunk sites. We analyze the interval between the HFZ and the upper Y coal, which spans the chron C29r/C29n magnetic reversal as constrained by magnetostratigraphy and radioisotopic dates (Sprain et al., 2015, 2018). **Herpijunk Rise:** The Herpijunk area is a butte complex immediately to the south/southeast of Iridium Hill Annex. The highest part of the butte contains the W coal, identified by its thickness ($\sim$ 2 m) and abundance of tephra layers (10+), including a diagnostic coarsely crystalline, white, tephra colloquially known as the "Sugar Ash" which appears both at Herpijunk Rise and Biscuit Butte (Noorbergen et al., 2017; Sprain et al., 2015). The base of the butte, known as Herpijunk Promontory, contains the IrZ coal and impact clay layer, which has an Ir anomaly of 11.7 ng/g in Smit and Van Der Kaars (1984). The HFZ coal is approximately 17 m above the IrZ coal, and it has been dated here (Renne et al., 2013, site referred to as "nearby Hauso Flats"). We analyze the portion of the butte between the HFZ coal and the W.

Bone Hollow: Bone Hollow is a locality approximately 8 km to the east of Nirvana that includes several late Cretaceous vertebrate fossil localities, as well as the Hell Creek-Tullock boundary (Arens et al., 2014). The top of the section is near the formational contact. Detailed stratigraphic information, as well as the $\delta^{13}C_{org}$ data, is from Arens et al., (2014). We place the Cretaceous-Paleogene boundary at the Hell Creek/Fort Union formational contact and estimate the

Table 4.1: Coordinates of localities in NE Montana, and references describing their chronostratigraphy

Site	Coordinates (WGS84)	Key Chronology references
Nirvana	47°31′37.14″N, 107°11′10.98″W	Sprain et al., (2015, 2018) Ickert et al., (2013)
Ir. Hill Annex (Hauso Flats)	47°31′36.23″N 107°12′36.76″W	Fendley et al., (2019) Sprain et al., (2015; 2018)
Hell Hollow	47°32′23.16″N, 107°10′16.62″W	Sprain et al., (2015; 2018)
Smurphy's Guess	47°33′0.9″N, 106°54′45.3″W	Arens et al., (2014)
Bone Hollow	47°32′8.0″N, 107°4′58.0″W	Arens et al., (2014)
Herpijunk Rise	top (W): 47°31.322′N 107°11.643′W base (HFZ): 47°31.502′N 107°11.987′W	Renne et al., (2013) Smit & Van Der Kaars, (1984)
Biscuit Basin	top (U): 47°29′11.52″N, 107°4′4.47″W middle (W): 47°29′35.07″N 107°4′15.37″W base (Y): 47°29′31.68″N 107°4′3.66″W	Lecain et al., (2014) Sprain et al., (2015)

total time represented by the section using a sediment accumulation rate calculated at the Thomas Ranch locality. We use the Thomas Ranch locality, as it is the closest Cretaceous locality to have chronostratigraphic constraints (Sprain et al., 2018). The Thomas Ranch section contains the chron C30n/C29r boundary and two dated tephra layers $\sim$ 23 m apart within the MCZ and Null coals (Sprain et al., 2018). At the Nirvana locality, there are 2 m of section between the MCZ and the K-Pg boundary within the IrZ coal. Assuming the same is true at Thomas Ranch, despite the lack of IrZ coal, we estimate there is $\sim$ 21 m of Cretaceous section at Thomas Ranch, which yields a sediment accumulation rate of $\sim$ 9 cm/ka. Using this sediment accumulation rate, we calculate that the 27 m of section at Bone Hollow represents $\sim$ 300 ka.

Smurphy's Guess: Smurphy's Guess is located $\sim$ 20 km E/NE of Nirvana and, like Bone Hollow, stretches a few tens of meters below the Hell Creek-Tullock contact. The detailed stratigraphy and $\delta^{13}C_{org}$ is from Arens et al., (2014). We use the sediment accumulation rate calculated from the Thomas Ranch locality to estimate that the 21 m of section represents approximately 240 ka. This duration may be an underestimate, as one study interpreted Smurphy's Guess to contain lacustrine deposits, which may have lower sediment accumulation rates than the river channel dominated Thomas Ranch locality (Bailey, Cohen, & Kring, 2005).

4.3 Methods

4.3.1 Carbon isotope analyses

Samples from Iridium Hill Annex, Nirvana, Hell Hollow, Herpijunk, and Biscuit Basin were collected from trenches exposing visibly unweathered rock, wrapped in aluminum foil, and placed into plastic bags. Samples that contained any roots or traces of modern plant/fungal material were not analyzed. Stratigraphic sections were recorded simultaneously with sample collection.

Samples were crushed to a fine powder using a ceramic mortar and pestle. Carbonate was removed from a 70 mg sample aliquot through acidification for 24 hours using 3 mL 1M HCl (e.g., Arens et al., 2014). The samples were then rinsed three times with 5mL MilliQ water, freeze-dried, and packed into tin capsules. They were analyzed for carbon isotope composition using a CHNOS Elemental Analyzer (Elementar, Hanau, Germany) interfaced with an IsoPrime100 mass spectrometer at the UC Berkeley Center for Stable Isotope Biogeochemistry. The calibration was based on the National Institute of Standards and Technology (Gaithersburg, MD, USA) reference materials. Long-term external precision is ± 0.10‰, and the carbon isotope composition of a laboratory quality control standard (soil material with certified low organic content from Elemental Microanalysis, Devon, UK) reproduced its accepted value of -26.66‰ with a median standard deviation of 0.03‰ (N=19). Duplicates of samples, acidified separately, had a median standard deviation of 0.09‰ (N=33).

4.3.2 Compilation of chemostratigraphic records and age models

NE Montana $\delta^{13}C_{org}$ record: For all our new records from the Williston Basin, we linearly interpolated between dates from volcanic tephra layers (Fig. 4.2). We acknowledge that the fluvial/deltaic depositional environments likely do not actually have linear sediment accumulation rates. Still, sediment accumulation rates calculated over hundreds of thousands of years are consistently 7-10 cm/ka (e.g., W to HFZ, HFZ to Null, using pooled dates from Sprain et al., 2015; 2018). The consistent sediment accumulation rates suggest that while brief ($\leq$ 10 ka) features may be distorted, longer timescale trends (10-100s of ka) are likely accurate.

IODP 1262 (Walvis Ridge) and 1209 (Shatsky Rise) $\delta^{13}C_{cc}$ records:

For the bulk carbonate isotope record ($\delta^{13}C_{cc}$) from Walvis Ridge for $\sim$ 66.4-64.8 time window from (Barnet et al., 2017, 2019), we adapt their astrochronologically tuned age model (Dinarès-Turell et al., 2014) so that the magnetochron boundaries are isochronous between 1262 and our Williston Basin record. To do this, we simply linearly expand or contract their age model to create additional tie points (see Table 4.2). This is to make sure that the records are directly comparable. In the 1262 cores, these chron boundaries have been constrained to within 30-60 cm (Bowles, 2006). We use the middle of this window as the depth (mcd) tie point. As the 1209 and 1262 age models are tied, we also recalibrate the age model for 1209 accordingly. These adjustments are also applied to the Birch et al. (2016) and S. A. Alvarez et al. (2019) records, which are from the 1262 and 1209 cores respectively. The purpose of these adjustments is to align all our chemostratigraphic records

Table 4.2: Table: Adjustments to Barnet age model. Depths are the middle of each boundary interval, from Bowles, 2006. Williston Basin (WB) ages are from Sprain et al., (2015; 2018)

Event	Core depth (mcd)	Original age (Ma)	WB age (Ma)
Chron C28r/C28n boundary	209.75	64.572	64.931
Chron C28r/C29n boundary	211.0	64.859	65.075
Chron C29r/C29n boundary	214.705	65.531	65.724
K-Pg Boundary	216.71	66.022	66.052
Chron C29r/C30n boundary	224.075	66.388	66.311

Table 4.3: Table: Stratigraphic height of chronologic tie points from the Gubbio section, and astronomically calibrated ages for the Umbria-Marche Basin (Sinnesael et al., 2016; 2019). Williston Basin (WB) ages are from Sprain et al., (2015; 2018)

Event	Strat. Height (m)	Astro. age (Ma)	WB age (Ma)
Chron C28r/C28n boundary	104.8	64.63	64.931
Chron C28r/C29n boundary	103.8	64.91	65.075
Chron C29r/C29n boundary	101.2	65.70	65.724
K-Pg Boundary	100	66.00	66.052
Chron C29r/C30n boundary	96.2	66.32	66.311

as accurately as possible, so we prioritize robust relative chronologic tie points (magnetochron boundaries). We are agnostic as to which age models are more accurate in terms of absolute age.

Gubbio section bulk carbonate $\delta^{13}C_{cc}$ record (Sinnesael et al., 2016, 2019):

For the Gubbio bulk carbonate $\delta^{13}C_{cc}$ record from Sinnesael et al. (2016, 2019), we tie the magnetic reversals and K-Pg boundary to the dates from Sprain et al. (2018) (Table 4.3). These are generally fairly similar to the astronomically calibrated chron boundary ages from this section.

Henehan et al. (2019) boron isotope pH and pCO_2 records: All dates are relative to the K-Pg boundary in the Henehan et al. (2019) composite record, which is calibrated to GTS 2012. We shift the entire record by 12 ka, moving the K-Pg boundary age from 66.04 to 66.052 Ma.

Songliao Basin paleosol carbonates $\delta^{13}C_{cc}$ and pCO_2 records (Gao et al., 2015; L. Zhang et al., 2018): The age models for each of these records is constructed using astrochronology from Wu et al. (2014) with magnetostratigraphic tie points. We use the relative age model as-is, except to shift the record such that the C29r/C30n boundary is 66.311 Ma. In Gao et al., (2015), the C29r/30n boundary is originally at 66.30 Ma, and in Zhang et al., (2015), the C29r/C30n boundary is originally at 66.398 Ma. Neither record uses the K-Pg boundary or C29r/C29n boundary as a tie point, as it is not independently identified in the core.

Boltysh Crater, Ukraine $\delta^{13}C_{org}$ record (Gilmour et al., 2013, 2014): The existing age model for the $\delta^{13}C_{org}$ record from the Boltysh crater is from cyclostratigraphy, in which the cycles have

Table 4.4: Boltysh crater age models. Ages from Sprain et al., (2015; 2018). Depths and magnetostratigraphy from Jolley et al., (2017).

Event	Depth (m)	Age (Ma)
Chron boundary (if C28r/C28n)	300	64.931
Chron boundary (if C29r/C29n)		65.724
K-Pg Boundary	581	66.052

Table 4.5: Table: Northern Pyrenean Basin age model. Ages from Sprain et al., (2015; 2018)

Event	Stratigraphic Height (m)	Age (Ma)
Chron C28r/C28n boundary	112	64.931
Chron C28r/C29n boundary	65	65.075
Chron C29r/C29n boundary	60	65.724
K-Pg Boundary	42.5	66.052

been interpreted to be 20 thousand year precession cycles. Based on this estimate of time duration, a magnetic polarity reversal near the top of the core was interpreted as the chron C29r/C29n boundary. These time estimates result in an extremely high sediment accumulation rate for this lacustrine system, in which $\sim$ 280 m of sediment were deposited in $\sim$ 330 ka (85 cm/ka). We reinterpret the chron boundary to represent the C28r/C28n boundary (64.931 Ma, Sprain et al., 2015). In this case, the sediment accumulation rate is a more moderate 20 cm/ka, and the observed cycles would be reinterpreted as 100 ka eccentricity cycles. The carbon isotope stratigraphy in the latter case is more similar to our new Montana record. The new chronostratigraphic tie points are presented in Table 4.4.

Northern Pyrenean Basin, France (Maufrangeas et al., 2020): To create a tentative age model for this record close to the K-Pg boundary, we assume linear sediment accumulation rates between magnetochron boundaries, using the K-Pg boundary and chron boundaries as tie points (Table 4.5). While this age model is inexact for chron C29r and C29n, the record is relatively low resolution in that interval.

Colombia $\delta^{13}C_{org}$ record (Carvajal-Ortiz, Mora, & Jaramillo, 2009): This record comprises two correlated records from the Catatumbo and Cesar-Rancheria Basins in Colombia. Their age models used pollen biozones as chronologic tie points (Jaramillo et al., 2005). To make this record directly comparable to our new record, we simply shifted the Colombian record such that the K-Pg boundary moved from 65 Ma to 66.052 Ma.

Beerling, Lomax, Royer, Upchurch, and Kump (2002) pCO_2 data: For the North Dakota data, we estimate ages using the average distance between the Chron C29r/C30n boundary and the K-Pg boundary in North Dakota (Peppe, Evans, & Smirnov, 2009), along with chron boundary ages (Sprain et al., 2018). For Bighorn Basin sites (LJH localities), the samples' age is unconstrained

Table 4.6: Table: Stomatal pCO_2 estimates used - top of Hell Creek Formation is assumed to be K-Pg boundary

Site	meters to K-Pg	Age (Ma)	References
DMNH 566 (ND)	-33	66.38	Peppe et al. (2009); Johnson (2002)
DMNH 1489 (ND)	-32	66.37	Peppe et al. (2009); Johnson (2002)
Clear Creek S. (CO)	0	66.052	Izett (1990)
LJH 7423 (MT)	5	65.5±0.5	Lyson et al. (2019); Wing, Alroy, and Hickey (1995)
LJH 7659 (WY)	5	65.5±0.5	Lyson et al. (2019); Wing et al. (1995)

except to within the Puercan North American Land Mammal Age. We use approximate Puercan age boundaries from Lyson et al. (2019) to assign an age to these localities, with an uncertainty of 0.5 Ma (Table 4.6).

We do not use data points outside of the 66.4 to 64.8 Ma interval. For Site 2360, the sample is within C28n (Raynolds et al., 2001), so it is some significant undetermined time younger than 64.931, so we do not use it. The age is also unclear for two of the older North Dakota data points, from sites DMNH 571 and 572. They are both approximately 60 m below the K-Pg boundary, placing them at least 30 m below the chron C29r/C30n contact (Peppe et al., 2009).

We do not use the Nordt, Atchley, and Dworkin (2003) pCO_2 dataset, as the chronostratigraphy for the Tornillo group is unclear during our time period of interest and contains several unconformities (e.g., Bataille, Watford, Ruegg, Lowe, & Bowen, 2016; Lehman, Wick, Beatty, Straight, & Wagner, 2018).

Steinthorsdottir, Vajda, and Pole (2016) pCO_2 data: We use the age model as is, but shift the record such that the K-Pg boundary is 66.052 Ma.

4.3.3 Calculation of $\delta^{13}C_{CO_2}$

To calculate $\delta^{13}C_{CO_2}$, we use the bulk carbonate record from IODP 1262 from Walvis Ridge in the South Atlantic (Barnet et al., 2017; 2019). We compare this result from $\delta^{13}C_{CO_2}$ calculated from IODP 1209 from Shatsky Rise in the equatorial Pacific (Hull et al., 2020).

The 1262 cores' bulk carbonate comprises calcareous nanofossils and planktic foraminifera (Zachos, Kroon, Blum, & Party, 2004). We follow a combination of the Barral et al., (2017) and Tipple et al., (2010) approaches. We use $\delta^{13}C_{cc}$ of bulk carbonate, rather than $\delta^{13}C_{cc}$ benthic foraminifera, as the latter requires correction for the surface to deep carbon isotope gradient created by the biological pump (Tipple et al., 2010). However, across the K-Pg, the biological pump partially collapses. Hence a constant correction is not appropriate (e.g., Zachos & Arthur, 1986; Esmeray-Senlet et al., 2015). Using bulk carbonate composition mitigates this issue.

To calculate $\delta^{13}C_{CO_2}$, using $\delta^{13}C_{CC}$ we must take into account fractionation between dissolved inorganic carbon (DIC) and CO_2 (ε_{DIC-CO_2}) and between $\delta^{13}C_{DIC}$ and $\delta^{13}C_{CC}$ (ε_{DIC-CC}). We

use the following equation from Tipple et al. (2010), adapted from J. Zhang, Quay, and Wilbur (1995):

$$\delta^{13}C_{CO_2(g)} = \left[\frac{(\delta^{13}C_{CC} + \varepsilon_{DIC-CC} + A) + 10^3}{\left(\varepsilon_{DIC-CO_2(g)}/10^3\right) + 1}\right] - 10^3 \tag{4.1}$$

A is a correction for disequilibrium isotope effects. In the Tipple et al., (2010) model, A is 2.8‰, due to a combination of air-sea surface disequilibrium (1±0.2), offsets due to the biological pump (1.2±0.4), subsurface bacterial oxidation or remineralization (0.6±0.3 ‰, specifically for benthic *Cibicidoides* foraminifera). As we are using bulk carbonate in our calculation, we only correct for air-sea surface disequilibrium and use an A of 1±0.2 ‰. ε_{DIC-CC} is constant with temperature and has a value of approximately -1 (Romanek, Grossman, & Morse, 1992).

We calculate ε_{DIC-CO_2} at each point, as it is dependent on sea surface temperature and DIC speciation (Zhang et al., 1995). While ε_{DIC-CO_2} can also be calculated as a weighted sum of the fractionation in each DIC species (e.g. the approach of Tipple et al., 2010), Zhang et al., (1995) also provides a net equation, which they demonstrate is more accurate, as it implicitly accounts for carbonate ion complexes and other complex behavior.

$$\varepsilon_{DIC-CO_2} = 0.0144(\pm 0.01) \times T \times f_{CO_3} - 0.107(\pm 0.002) \times T + 10.53(\pm 0.05) \tag{4.2}$$

T is sea surface temperature (°C). $f_{\mathrm{CO_3}}$ is the fraction of CO_3 within DIC and is dependent on temperature and pH (e.g., J. Zhang et al., 1995). Zhang et al., (1995) report an average total error of 0.05 ‰ for their experimental range (T between 5 and 25 °C and $f_{\mathrm{CO_3}}$ between 0.05 to 0.20). This average error is parametrized by uncertainty on each constant within the equation. We calculate $f_{\mathrm{CO_3}}$ at each time step using the concentration of CO_3 and DIC from the calculations of Henehan et al., (2019) based on their boron isotope record across this interval (available in their supplement). $f_{\mathrm{CO_3}}$ is straightforwardly calculated as:

$$f_{\mathrm{CO_3}} = \frac{[\mathrm{CO_3}]}{[DIC]} \tag{4.3}$$

The calculated $f_{\mathrm{CO_3}}$ varies between 0.026 at the K-Pg boundary and 0.132, with a $f_{\mathrm{CO_3}}$ of $\sim$ 0.065 at 66.8 Ma and 65.6 Ma. As the value of $f_{\mathrm{CO_3}}$ is the same at both 400 ka after the K-Pg extinction and 400 ka before the Late Maastrichtian Warming Event, we interpret this as a background value for this time interval. As such, we assume that $f_{\mathrm{CO_3}}$ stays at 0.065 until the end of our record (64.8 Ma).

The difference between using these variable $f_{\mathrm{CO_3}}$ values and a constant of 0.12 (Barral et al., 2017) or 0.09 (Tipple et al., 2010) is very small. The mean difference in $\delta^{13}\mathrm{C}_{CO_2}$ between calculations using a constant $f_{\mathrm{CO_3}}$ of 0.12 and varying $f_{\mathrm{CO_3}}$ based on Henehan et al. (2019) is 0.02‰. Therefore, we do not consider uncertainty on $f_{\mathrm{CO_3}}$, which is smaller than this range.

We calculate relative temperature changes using each sample's oxygen isotope composition.

$$T\,(^{\circ}C) = 16.1 - 4.64(\delta^{18}\mathrm{O}_{cc} - \delta^{18}\mathrm{O}_{sw}) + 0.09(\delta^{18}\mathrm{O}_{cc} - \delta^{18}\mathrm{O}_{sw})^2 \tag{4.4}$$

where $\delta^{18}\mathrm{O}_{cc}$ is the oxygen isotope composition of each calcite sample and $\delta^{18}\mathrm{O}_{sw}$ is seawater, for which we use -1.27‰ VSMOW for an ice-free world (e.g., Barnet et al., 2019).

However, the absolute value of benthic-derived temperature is ∼8-12°C, colder than observed K-Pg sea-surface temperatures from Argentina of ∼25-30°C (Woelders et al., 2017). Tipple et al., (2010) addressed the surface to deep temperature gradient by using data from high latitude sites near downwelling zones, minimizing the difference between surface and deep temperatures. Barral et al., (2017) uses sea-surface temperatures derived from the oxygen isotope composition of fish phosphate.

We utilize a combination approach. The bulk $\delta^{18}\mathrm{O}_{cc}$ record from IODP 1262 has similar relative temperature changes as contemporaneous TEX_{86} derived sea-surface temperature measurements from relatively nearby Argentina (Woelders et al., 2017). We use relative temperature changes from the $\delta^{18}\mathrm{O}_{cc}$, then calculate the difference between each temperature and the median $\delta^{18}\mathrm{O}_{cc}$ temperature between 66.3 and 66.4 Ma. We chose this interval as it was before the Late Maastrichtian Warming Event (e.g., Barnet et al., 2019). We then add Δ_{temp} to an estimate of sea surface temp from ∼66.3 Ma from TEX_{86} (27 degrees, Woelders et al., 2017) to create the sea surface temperature record.

For the 1209 record, we utilize a similar approach. We calculate Δ_{temp} with respect to 64.6-64.5 Ma. The 1209 bulk carbonate record does not extend more than 100 ka before the K-Pg boundary, so we could not use pre-LMWE as a reference. As we could not find a nearby coeval TEX_{86} record, we used a reference temperature of 27°C from a compilation of low-latitude latest Cretaceous TEX_{86} sea surface temperature estimates (O'Brien et al., 2017).

For each record, the $\delta^{13}\mathrm{C}_{CO_2}$ value has a 2 sigma uncertainty of ∼0.4‰, established using Monte Carlo error propagation. The records from 1209 and 1292 generally overlap, and their 2 sigma uncertainty windows are nearly identical (Fig. 4.7). Going forward, we compare the $\delta^{13}\mathrm{C}_{org}$ record to the $\delta^{13}\mathrm{C}_{CO_2}$ derived from the 1262 cores only, as it extends farther into the Cretaceous.

4.3.4 Calculation of $\Delta^{13}\mathrm{C}_{plant}$

$\Delta^{13}\mathrm{C}_{plant}$ is the difference between the carbon isotope composition of the atmosphere and that of plant material. This parameter represents the amount of fractionation during photosynthetic carbon fixation. It is defined as:

$$\Delta_{\mathrm{plant}} = \frac{\delta^{13}\mathrm{C}_{\mathrm{CO_2}} - \delta^{13}\mathrm{C}_{\mathrm{org}}}{1 + \delta^{13}\mathrm{C}_{org}/1000} \tag{4.5}$$

We linearly interpolate our new $\delta^{13}\mathrm{C}_{CO_2}$ to establish values and uncertainty at each time point of our $\delta^{13}\mathrm{C}_{org}$ record. As the $\delta^{13}\mathrm{C}_{CO_2}$ record is of a comparable or higher resolution through time, the linear interpolation does not meaningfully increase uncertainty.

4.3.5 pCO_2 estimate

We estimate the pCO_2 change required to explain the observed changes in $\Delta^{13}C_{plant}$. We do this using the proxy proposed by Schubert and Jahren (2012), utilizing the most recent formulation from Cui, Schubert, and Jahren (2020). We have simplified the algebraic expression slightly by creating a factor we designate X_1, then arranging the equations to solve for the change in pCO_2 (ΔpCO_2). X_1 is similar in concept to the originally proposed $\Delta(\Delta^{13}C)$ (e.g., Cui & Schubert, 2016).

$$\Delta^{13}C_{CO_2} = \delta^{13}C_{CO_{2(t=0)}} - \delta^{13}C_{CO_{2(t)}} \tag{4.6}$$

$$X_1 = \delta^{13}C_{org(t=0)} - \delta^{13}C_{org(t)} - \Delta^{13}C_{CO_2} - \varepsilon \tag{4.7}$$

$$\Delta pCO_2 = pCO_{2(t)} - pCO_{2(t=0)} \tag{4.8}$$

$$pCO_{2(t)} = \frac{X_1\left[(A+BC)^2 + pCO_{2(t=0)} \times B\,(A+BC)\right] + pCO_{2(t=0)} \times A^2B}{-X_1B\left[(A+BC) + pCO_{2(t=0)} \times B\right] + A^2B} \tag{4.9}$$

$$\Delta pCO_2 = \frac{X_1\left[(A+BC) + pCO_{2(t=0)} \times B\right]^2}{-X_1B\left[(A+BC) + pCO_{2(t=0)} \times B\right] + A^2B} \tag{4.10}$$

where A, B, and C are curve fitting parameters (A=28.26, B=0.22 ± 0.028, (Schubert & Jahren, 2012; Cui & Schubert, 2016)). C is solved for at every Monte Carlo step (Cui & Schubert, 2016). ε (Eqn 7) here is a parameter for any non-pCO_2 related changes in $\Delta^{13}C_{plant}$, such as changing plant assemblages (e.g. angiosperm dominated to gymnosperm dominated) (e.g., Cui et al., 2020). As North American ecosystems during this period are angiosperm dominated before and after the K-Pg, we set ε to 0 (e.g., Spicer & Collinson, 2014).

$$C = \frac{4.4 \times (A)}{(A-4.4) \times (B)} \tag{4.11}$$

Conceptually, A is the fractionation done by the plants (can vary between 30 and 26 for C3). Note that this is different from A, the disequilibrium correction in the $\delta^{13}C_{CO_2}$ calculation. Epsilon is the offset between different plant tissues (e.g., between lipid and leaf). As we always examine bulk organic material, we allow epsilon = 0. This is an oversimplification, as plant assemblages are changing over the K-Pg boundary. However, it is not quantitatively clear how to account for this. Hence, part of the rapid shift in $\Delta^{13}C_{plant}$ at the K-Pg boundary is possibly partly due to plant species changes.

We calculate the change in pCO_2, using different initial pCO_2 values of 800, 600, and 400 ppm. We do not incorporate uncertainty on initial pCO_2, rather we show the results for a range of potential initial values. For initial $\delta^{13}C_{p(t=0)}$ and $\delta^{13}C_{CO_{2(t=0)}}$, we use the median values between 66.3 and 66.4 Ma of $\delta^{13}C_{org}$ (-24.7 ± 0.35‰) and $\delta^{13}C_{CO_2}$ (-4.6 ± 0.23‰) respectively.

Table 4.7: Table: Uncertainty incorporated into Monte Carlo uncertainty analysis

Parameter	1 σ uncertainty	Source
Eqn 1: Air-sea surface disequilibrium (A)	± 0.2	Tipple et al., (2010)
Eqn 2: Coefficients for ε_{DIC-CO_2}	± 0.01, ± 0.002, ± 0.05	Zhang et al., (1995)
Eqn 5: Analytical on $\delta^{13}C_{org}$	± 0.1‰	This study
Eqn 9/10: Curve-fitting parameter B	± 0.028	Cui et al. (2020)

4.3.6 pCO_2 recalibration

We recalibrated the paleosol carbonate derived pCO_2 estimates from Zhang et al. (2018) to incorporate our new $\delta^{13}C_{CO_2}$ record. We used the same equations and uncertainty propagation used in Zhang et al. (2018, see their supplement materials for details). We note that Huang et al. (2013) utilized paleosol carbon isotope analyses from the same core and the same model to estimate pCO_2. However, while L. Zhang et al. (2018) used clumped carbonate isotope analyses to estimate temperature, Huang et al. (2013) used temperature estimates based solely on the oxygen isotope composition of the paleosol carbonate. These temperature estimates are less robust as they do not account for changes in soil water $\delta^{18}O$ (e.g., Swart, 2015). Therefore, we only use the pCO_2 estimates from Zhang et al. (2018).

4.3.7 Uncertainty propagation

We utilize Monte Carlo resampling (1000x) to propagate uncertainty through these calculations. The sources of uncertainty for each calculation are in Table 4.7. We follow a similar approach as Tipple et al., (2010) and Cui and Schubert (2016) to uncertainty propagation on $\delta^{13}C_{CO_2}$ and ΔpCO_2.

For $\Delta^{13}C_{plant}$ values, we do a LOESS fit of all 1000 MC runs (of $\Delta^{13}C_{plant}$ versus age), utilizing a window size of 20% and a second-order polynomial fit. The LOESS fit determines the trend, independent of scatter in $\delta^{13}C_{org}$ because of integration over various plant species. To determine the uncertainty on this trend, we perform a running standard deviation of the residuals (using the loess function from core R stats package, and runsd from the caTools R package (Tuszynski, 2012)).

If we utilize the same LOESS smoothing on just the $\delta^{13}C_{org}$ record, the residuals have a standard deviation of 0.7 ‰. This variability is reasonably consistent with standard deviations of 0.8 ‰ observed in leaf carbon within a plant community (Arens et al., 2002 using data from Smedley et al. (1991) and Mooney, Bullock, and Ehleringer (1989), from a temperate grassland and a tropical woodland). As a result, we believe the trend likely represents changes in environmental conditions more accurately than point to point variation.

To estimate changes in pCO_2, we use a LOESS fit (of change in pCO_2 versus age) of all 1000 MC runs with a window size of 20% and second-order polynomial fit. We use a running 5th and 95th quantile of the residuals to estimate uncertainty instead of standard deviation, as the uncertainty is

asymmetrical (loess from core R stats package, runquantile from the caTools R package (Tuszynski, 2012)).

4.4 Results and Discussion

4.4.1 Interpretation and validity of terrestrial carbon isotope records

We first examine our new $\delta^{13}C_{org}$ record, and assess its trends, variability, and relationship with depositional features (Fig. 4.2, Fig. 4.3).

Our $\delta^{13}C_{org}$ values do not show a strong relationship with carbon concentration. However, the $\delta^{13}C_{org}$ data show some lithologic biases. The $\delta^{13}C_{org}$ values in sandstones and carbonaceous shales are statistically different from those from siltstones and mudstones. These biases likely reflect slightly different carbon sources or diagenetic features in different depositional environments. Modern ecosystem studies show that the $\delta^{13}C_{org}$ of palustrine organic material (likely similar to coals and carbonaceous shales) tends to be more negative than nearby riverbanks (e.g., Hupp et al., 2018). However, this pattern does not explain the sandstone $\delta^{13}C_{org}$ values. The lower $\delta^{13}C_{org}$ in sandstones is potentially due to partial loss of carbon from dissolution, as the porosity in sandstone is much higher than other lithologies. Regardless of the causes of these biases, we include only data from siltstones and mudstones in our final record to ensure that we are not introducing offsets in the data due to different lithologies. However, we note that including them does not change the record substantially, and the trend remains the same (Fig. 4.3).

The scatter in our $\delta^{13}C_{org}$ record is fairly consistent through time, excepting a brief increase in variability coincident with the K-Pg boundary. In general, this scatter is most likely due to integration over different plant tissues and species. Our record has a standard deviation of 0.7 ‰ of residuals around a LOESS curve (20% window, second-order polynomial fit). This 0.7‰ range is shown as a red window (Fig 3). The 2 sigma uncertainty on the LOESS fit (shown as a blue window) is smaller than this range. This range in $\delta^{13}C_{org}$ of about 2 ‰ at a single time point is consistent with ranges of 2-4 % in leaf $\delta^{13}C$ within open canopy forest ecosystems Maastrichtian and Paleocene environments (Graham, Herrera, Jaramillo, Wing, & Freeman, 2019). A similar analysis of modern variation in $\delta^{13}C_{leaf}$ within modern ecosystems yielded standard deviations of 0.8 ‰ (Arens et al., 2002). We believe that, in general, single-point changes in $\delta^{13}C_{org}$ are not meaningful to interpret. However, we hypothesize that the longer-term trends represent changes in $\delta^{13}C_{CO_2}$ or environmental conditions.

We see somewhat higher variability ($\sim \pm 2$ ‰) in $\delta^{13}C_{org}$ in the $\sim$25 ka window around the K-Pg boundary. The higher variability is possibly due in part to floral species turnover or environmental changes close to the K-Pg boundary and extinction. Our LOESS fit (Fig. 4.4) suggests an immediate decrease in $\delta^{13}C_{org}$ at the boundary of < 0.5‰. This decrease likely corresponds to the brief excursion noted in other studies (e.g., Arens & Jahren, 2000). However, Grandpre et al. (2013) previously demonstrated that this excursion is not statistically significant due to the amplitude of point-to-point variability inherent in these records and the brevity of the

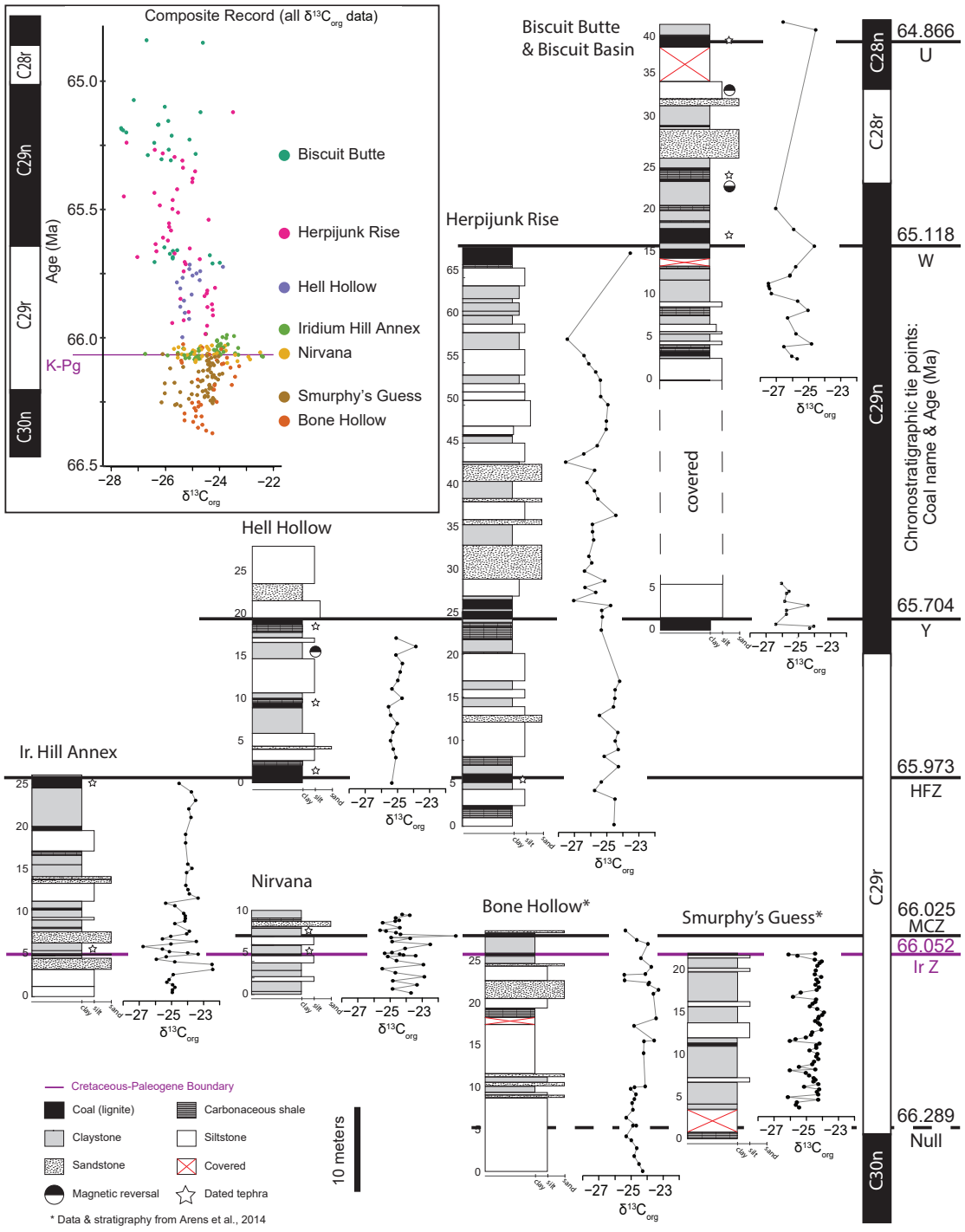

Figure 4.2: Individual $\delta^{13}C_{org}$ records from each Montana locality, including chronostratigraphic tie points. Inset plot shows composite record with localities indicated. The purple line at the Ir Z coal represents the age of the Cretaceous-Paleogene boundary.

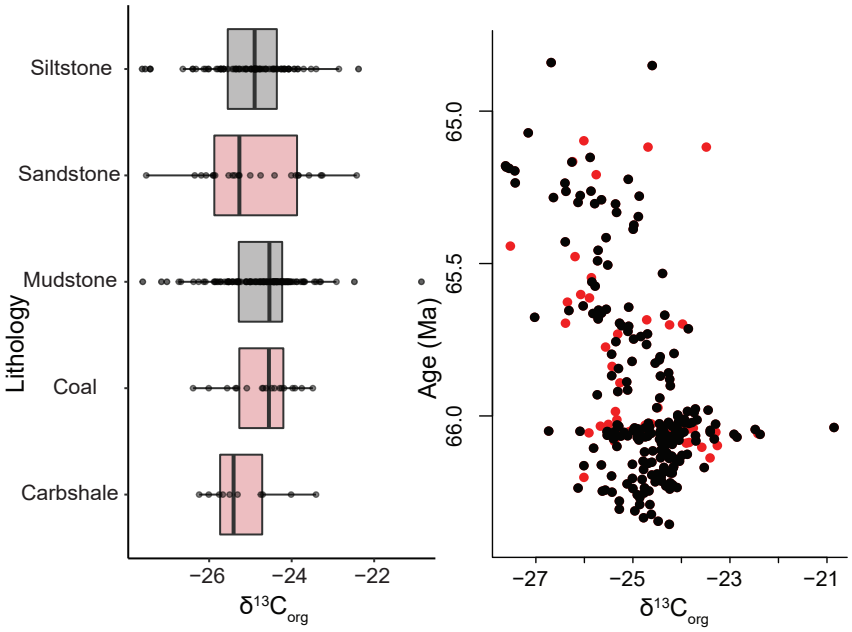

Figure 4.3: Relationship between lithology/depositional environment and $\delta^{13}C_{org}$. There is no strong relationship, however the $\delta^{13}C_{org}$ values for carbonaceous shales and sandstones are slightly lower in general. We remove all data from sandstones, carbonaceous shales, and coals (in red points), however they do not have a significant effect on the trend.

decrease. Hence, we will not extensively interpret or discuss this brief decrease, and instead, we will focus on the longer-scale trends that are more likely to be robust.

4.4.2 Global terrestrial $\delta^{13}C$ records

To test whether the trends in our $\delta^{13}C_{org}$ record are global signals, we compare our results to other existing terrestrial records of $\delta^{13}C$ ($\delta^{13}C_{org}$ and paleosol carbonate $\delta^{13}C$from the latest Cretaceous and earliest Paleocene (Fig. 4.4). None of the records exhibit a long-lived excursion that initiates at the K-Pg boundary. To aid in comparison, we plot the LOESS fit of our Montana record on top of each of the other records, with an offset to align pre-boundary values in the case of the records from China, Boltysh, and Colombia (Fig. 4.4). The $\delta^{13}C_{org}$ record from Colombia (Carvajal-Ortiz et al., 2009) displays no significant trend during this time interval. However, the other records, including ours, display similar gradual decreases in $\delta^{13}C$ over the first 500-800 ka of the Paleocene. Data from the Boltysh and Pyrenean Basin records suggest that terrestrial $\delta^{13}C_{org}$ values start increasing again by 65.3-65 Ma at the latest.

It is also particularly interesting that the paleosol carbonate record from the Songliao Basin in China also records a gradual decrease in $\delta^{13}C$, rather than an excursion precisely at the boundary (Gao et al., 2015; Huang et al., 2013; L. Zhang et al., 2018). Paleosol carbonate $\delta^{13}C$ reflects a

mixture of atmospheric carbon and carbon respired by plants and other organisms (e.g., L. Zhang et al., 2018). The lack of a sudden excursion suggests that the plants in this region did not experience an immediate drop in $\delta^{13}C_{org}$, similar to our Montana record.

The amplitude of the decrease is slightly greater in the Boltysh crater lacustrine $\delta^{13}C_{org}$ record ($\sim 4‰$ compared to $\sim 3‰$) (Fig. 4.4). This record also has a substantially larger range in $\delta^{13}C_{org}$, including values as low as $-36‰$. The large range of $\delta^{13}C_{org}$ is likely due to the local lacustrine environment, which incorporates carbon from algae as well as C3 plants from the surrounding forests (Jolley et al., 2017). Lake algae and other phytoplankton have highly variable carbon isotope composition, with $\delta^{13}C$ generally in modern environments between -25 and -35 ‰ (Vuorio, Meili, & Sarvala, 2006).

We note that the Boltysh crater record has high $\delta^{13}C_{org}$ variability at the K-Pg boundary, including several more positive $\delta^{13}C_{org}$ values. According to radioisotopic dates on the impact breccias, the Boltysh crater impact occurred only a few thousand years before the K-Pg boundary. The K-Pg boundary portion of the section is directly on top of impact suevites (Gilmour et al., 2013; Jolley, Gilmour, Gurov, Kelley, & Watson, 2010; Kelley & Gurov, 2002). We do not interpret these positive values in a paleoenvironmental context, as the original authors suggest the high variability during this interval is a result of the "nugget effect," due to very low carbon concentration (< 300 ppm) in this interval (Jolley et al., 2010).

The record from the Northern Pyrenean Basin, France, is the most similar to our new record. The environment of deposition is also fluvial to floodplain sediments, and the absolute value and variability of $\delta^{13}C_{org}$ are similar overall (Maufrangeas et al., 2020). However, it is difficult to compare the records' trends, as the French record has relatively low resolution during the interval of overlap. When we plot the French record with the LOESS fit from our Hell Creek record (no offset), the trends are compatible. Both records display roughly constant values during the latest Maastrichtian and a gradual decrease during the early Paleocene (Fig. 4.4).

The paucity of data in the chron C28r portion of our Montana record does not permit analysis of the increase in $\delta^{13}C_{org}$. In order to include this portion of the recovery interval, we created a composite record which includes the C28r portion of the France $\delta^{13}C_{org}$ record. We chose this record because it is the most similar in terms of environmental setting . The beginning and end of C28r is known from magnetostratigraphy in both locations, so there is no relative age uncertainty between these portions of our records.

4.4.3 Trends in terrestrial and marine $\delta^{13}C$ across the K-Pg boundary

These records suggest that the brief negative excursion proposed by Arens and Jahren (2000) should not be the primary feature analyzed by interpretations of terrestrial $\delta^{13}C$ during this time interval. Instead, a more prolonged excursion is a robust feature that is consistent between records around the globe. Hence, there is no longer reason to interpret terrestrial $\delta^{13}C$ records as requiring a rapid recovery of carbon cycle dynamics, including global primary productivity.

We find several key global trends in terrestrial $\delta^{13}C$ records across the K-Pg boundary. Between 66.3 Ma and the extinction, $\delta^{13}C$ gradually increases, similar to the trend in marine records (Fig

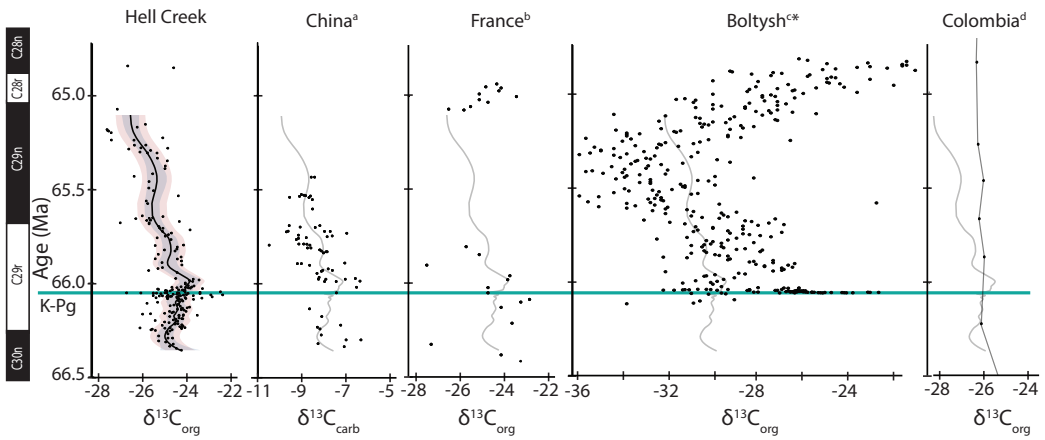

Figure 4.4: Global compilation of terrestrial $\delta^{13}\mathrm{C}$ records of $\geq$100 ka duration with age constraints. Records are from a: Gao et al. (2015); L. Zhang et al. (2018), b: Maufrangeas et al. (2020), c:Gilmour et al. (2013) with adjusted age model (Section 3.2),), d: (Carvajal-Ortiz et al., 2009). The LOESS fit from our new Hell Creek record is superimposed on each record, offset to best align with the Maastrichtian data in each record. The France record is presented with the original LOESS curve (no offset).

4.5). There is no consistent excursion precisely at the K-Pg boundary. Instead, a gradual decrease begins ca. 50 ka post-extinction in our Hell Creek record. It is not clear from the other records whether this decrease begins coincident with the boundary or slightly after, as our Hell Creek record is the only study locality with a clearly defined K-Pg boundary impact clay layer and Ir anomaly. The gradual decrease reached a nadir near the end of chron C29n, at $\sim$ 65.25 M, after which $\delta^{13}\mathrm{C}$ increased back to late Maastrichtian values by early chron C28n, $\sim$ 64.8 Ma.

While our new terrestrial $\delta^{13}\mathrm{C}$ record is more similar to marine records than previously thought (based on the previously available data), the $\delta^{13}\mathrm{C}$ excursion at the K-Pg boundary in terrestrial environments is still quite different from the excursion observed in marine environments. In particular, the terrestrial $\delta^{13}\mathrm{C}$ record does not follow the same pattern as open ocean bulk carbonate: a sudden excursion followed by increasing $\delta^{13}\mathrm{C}$ within $\sim$ 100 ka. Instead, the change in $\delta^{13}\mathrm{C}$ is similar to benthic records until ca. the C29r/C29n boundary. During chron C29n, the terrestrial $\delta^{13}\mathrm{C}$ continues to decrease while benthic $\delta^{13}\mathrm{C}$ stays roughly constant.

The differences between terrestrial and marine records are apparent even when using different LOESS windows (Fig. 4.6). A smaller LOESS window of 10% makes some smaller-scale features more evident. Potentially interesting features include a slight increase during the first half of chron C29r, which is roughly parallel to the increasing trend in bulk and benthic $\delta^{13}\mathrm{C}_{cc}$. More high-resolution terrestrial records during this time interval are necessary to clarify whether these smaller-scale trends are global.

We propose two potential mechanisms that could lead to differences between marine carbonate

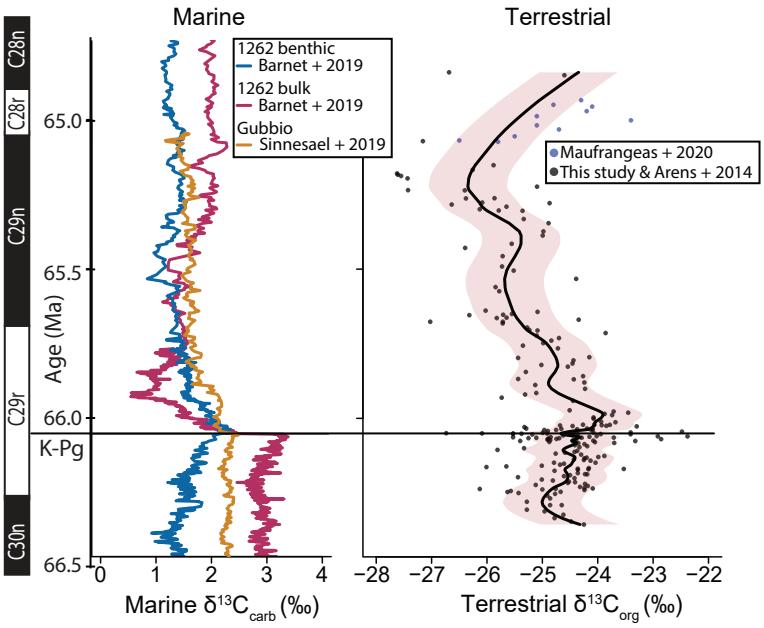

Figure 4.5: Comparison of the new composite terrestrial $\delta^{13}C_{org}$ record with marine $\delta^{13}C_{cc}$ records from open ocean cite 1262 (Walvis Ridge, Barnet et al., 2019) and shelf marine (Gubbio, Italy, Sinnesael et al., 2019). Age models for all records have been adjusted such that each magnetochron boundaryand the K-Pg boundary are isochronous throughout all records.

$\delta^{13}C$ and terrestrial $\delta^{13}C_{org}$. Firstly, it is possible that plants, in aggregate, are changing how they are fractionating carbon, due to changing environmental conditions. Alternatively, the land-atmosphere-ocean carbon cycle could not be entirely in equilibrium during this interval. This disequilibrium could be because of limited exchange of carbon between the ocean and atmosphere or atmosphere and terrestrial reservoirs, or because atmospheric $\delta^{13}C_{CO_2}$ is highly spatially heterogeneous between marine and continental regions. We will first test the first possibility - that plant carbon isotope fractionation is fluctuating due to changing environmental parameters.

4.4.4 Calculation of $\delta^{13}C_{CO_2}$ from marine $\delta^{13}C_{cc}$

To test whether changing carbon isotope discrimination in plants could have caused the differences between terrestrial and bulk marine $\delta^{13}C$ records, we first must estimate $\delta^{13}C_{CO_2}$ based on the marine records.

Underlying this calculation of $\delta^{13}C_{CO_2}$ is the assumption that marine dissolved inorganic carbon (DIC) and atmospheric carbon dioxide are in equilibrium during this entire time interval. Therefore, we use the isotopic composition of bulk carbonate instead of benthic foraminifera. The partial collapse of the biologic pump during the first $\sim$ 700 ka of the Paleocene results in a significant decrease in the surface to deep carbon isotope gradient. When calculating $\delta^{13}C_{CO_2}$ from

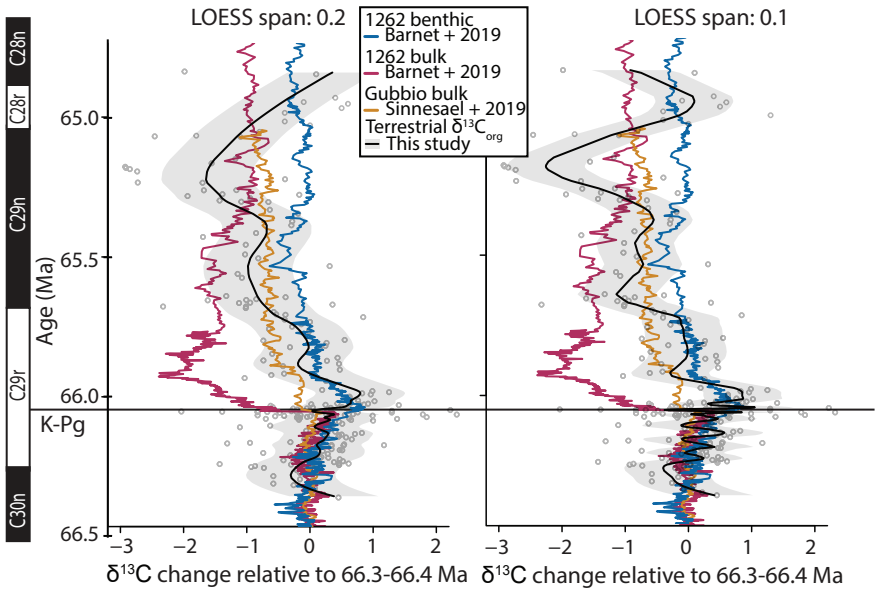

Figure 4.6: Change in δ^{13}C relative to 66.4-66.3 Ma median value for shelf marine bulk carbonate (Gubbio, Sinnesael et al., 2019), open ocean bulk and benthic carbonate (Walvis Ridge, Barnet et al., 2019), and terrestrial bulk organic carbon (this study). We use two LOESS window sizes: a span of 0.2 (20% of data points) and 0.1 (10%). In both cases, the long-term trend is the same. However, the smaller LOESS window makes some smaller-scale features more distinct.

benthic foraminifera $\delta^{13}C_{cc}$, this gradient is assumed to be constant, and would therefore result in an incorrect offset during this time interval (Esmeray-Senlet et al., 2015; Tipple et al., 2010).

We calculate $\delta^{13}C_{CO_2}$ using bulk carbonate isotope composition from the IODP 1209 and 1262 core records (Barnet et al., 2019; Hull et al., 2020). The two resulting $\delta^{13}C_{CO_2}$ curves are consistent, and well within uncertainty of each other (Fig. 4.7). The calculated $\delta^{13}C_{CO_2}$ is nearly a consistent offset to the bulk carbonate isotope data. As such, a significant negative excursion in $\delta^{13}C_{CO_2}$ coincides with the K-Pg boundary, and $\delta^{13}C_{CO_2}$ continues to decrease for $\sim$100 ka. $\delta^{13}C_{CO_2}$ then slowly increases over the next several hundred thousand years. In marine records, this increases the offset between bulk and benthic records and suggests increasing recovery of the biological pump (e.g., Birch et al., 2016).

This estimate of $\delta^{13}C_{CO_2}$ is broadly consistent with the Tipple et al. (2010) and Barral et al. (2017) compilation records for the Cenozoic and Cretaceous respectively. There is an offset of about 1.5-2 ‰ between Barral et al. (2017)'s late Maastrichtian $\delta^{13}C_{CO_2}$ value of -6.6 ‰ and ours of -5 to -4.5 ‰. This offset is due in part to different temperature estimates Barral et al. (2017) estimates 20°C, derived from oxygen isotope composition of marine phosphates, we estimate 27°C from TEX_{86}), and in part to our choice of disequilibrium correction (A of 1 $\pm$0.2 ‰). Our estimate of $\delta^{13}C_{CO_2}$ of -5.5 ‰ in the early Paleocene after the K-Pg boundary interval ($\sim$ 65.2 - 64.8 Ma)

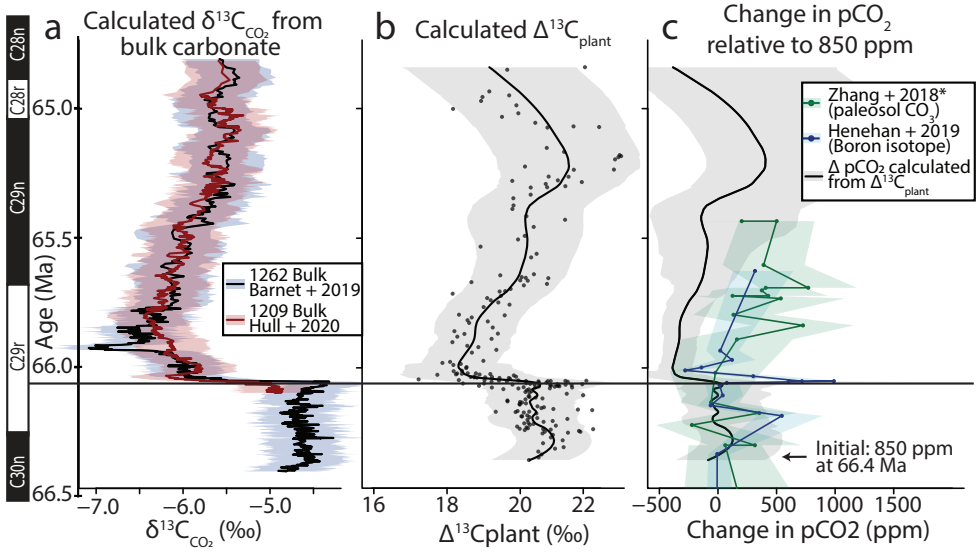

Figure 4.7: **a)** Calculated $\delta^{13}C_{CO_2}$ using open ocean bulk carbonate $\delta^{13}C_{cc}$ records. This assumes that the DIC pool is in equilibrium with the atmosphere, and that the $\delta^{13}C_{cc}$ records are globally representative. **b)** Calculated $\Delta^{13}\mathrm{C}_{plant}$, using the our new terrestrial $\delta^{13}C_{org}$ record and the calculated $\delta^{13}C_{CO_2}$ in a). **c)** Comparison of the change in pCO_2 observed in proxy records with the amount required to cause the changes in the calculated $\Delta^{13}\mathrm{C}_{plant}$ curve.

is consistent with Tipple et al., (2010)'s estimate for $\sim$ 64 Ma (also -5.5 ‰).

4.4.5 $\Delta^{13}\mathrm{C}_{plant}$ across the K-Pg boundary

If there were no change to how plants fractionate carbon, i.e. if $\Delta^{13}C_{plant}$ is constant, then the $\delta^{13}C_{org}$ record would be consistently offset from the $\delta^{13}C_{CO_2}$ record. $\Delta^{13}\mathrm{C}_{plant}$, defined in Eqn 5, is conceptually the difference at each point between $\delta^{13}\mathrm{C}_{org}$ and $\delta^{13}\mathrm{C}_{CO_2}$, and we calculate $\Delta^{13}\mathrm{C}_{plant}$ using our new $\delta^{13}\mathrm{C}$ records. For C3 plants in modern environments, $\Delta^{13}\mathrm{C}_{plant}$ is generally around 15-25 ‰ (Cornwell et al., 2018). It reflects net carbon isotope discrimination, which comprises photosynthesis ($\sim$28‰), diffusion ($\sim$4.4‰), and the ratio of partial pressure of CO_2 in the chloroplast (frequently termed c_i or p_c), or to pCO_2 in the atmosphere (in this context frequently termed c_a or p_a) (e.g., Cornwell et al., 2018; Cui & Schubert, 2016). This c_i/c_a term is dynamic, and depends on plant physiological responses to water stress, changes in atmospheric pCO_2, soil pH, and other environmental stressors (e.g., Cornwell et al., 2018; Kohn, 2010; Schubert & Jahren, 2013).

$\Delta^{13}\mathrm{C}_{plant}$ increases with increasing pCO_2, and this relationship has been used as a proxy for pCO_2 in the geologic past (e.g., Hare, Loftus, Jeffrey, & Ramsey, 2018; Schubert & Jahren, 2012). However, others have proposed a stronger dependence on precipitation (e.g., Kohn, 2010; Schlanser et al., 2020). Studies of modern $\Delta^{13}\mathrm{C}_{plant}$ show quantitative relationships with each of

these variables (Cornwell et al., 2018; Kohn, 2010). We use these relationships to evaluate the environmental changes required to create the observed changes in $\Delta^{13}C_{plant}$.

4.4.6 pCO_2 records & precipitation changes

As pCO_2 and precipitation changes can influence $\Delta^{13}C_{plant}$, we compile existing pCO_2 records with chronologic constraints, and estimates of precipitation.

pCO_2 records: We compile several records of pCO_2 calculated using a variety of methods, all of which have good chronologic constraints. Our requirement of robust chronologic constraints precludes the use of the Nordt et al. (2003) dataset of paleosol carbonates from the Tornillo Group (Big Bend National Park, Texas). The Tornillo group has significant chronostratigraphic uncertainty, due to disagreement on the placement of several unconformities (Nordt et al., 2003; Lehman et al., 2018; Bataille et al., 2016). We plot several data points from stomatal proxies from Beerling et al. (2002), with recalibrated pCO_2 values from Barclay and Wing (2016) and Milligan et al. (2019), and additional stomata-based data from Steinthorsdottir et al. (2016). In general, the uncertainty on age placement is not negligible, because of a lack of age constraints in some cases beyond the magnetochron or North American Land Mammal Age. Note that we plot both the Milligan et al. (2019) recalibrated value and the Barclay and Wing (2016) recalibrated value for two of the points. We also plot the pCO_2 records from L. Zhang et al. (2018) based on $\delta^{13}C$ of paleosol carbonate nodules, and Henehan et al. (2019), based on boron isotope composition of marine planktic foraminifera. In these cases, we do not plot uncertainty on ages, as there is no uncertainty relative to our other records because we have recalibrated each age model to fit the K-Pg boundary and chron boundaries of Sprain et al. (2018). We have recalibrated the L. Zhang et al. (2018) pCO_2 values using our new $\delta^{13}C_{CO_2}$ record. All error bars and shaded regions represent 1σ uncertainty.

It is remarkable how well the L. Zhang et al. (2018) and Henehan et al. (2019) records agree, considering the relatively large uncertainty on each, and that they are derived from completely independent proxies. However, the stomata-based estimates indicate pCO_2 values of 350-450 ppm, several hundred ppm lower than the other estimates based on paleosol carbonate and foraminiferal boron isotope composition (Fig. 4.6). It is difficult to reconcile these lower values with the high global temperatures in the Cretaceous (O'Brien et al., 2017). As a rough estimate of whether the higher pCO_2 estimates are reasonable, we use the two records, along with a deep ocean temperature record, to estimate climate sensitivity during this time interval. Climate sensitivity (ECS) is the temperature change expected per doubling of pCO_2, such that:

$$\Delta T\,(^{\circ}C) = ECS \times \frac{\ln\left(pCO_{2(t)}/pCO_{2(t=0)}\right)}{\ln(2)} \tag{4.12}$$

Climate sensitivity is an essential parameter for climate models that calculate global temperature changes due to changing pCO_2. Climate sensitivity in the Mesozoic and Cenozoic is estimated to be $\sim$3-6°C, with some estimates as high as 6.6°C at the Paleocene-Eocene Thermal Maximum (e.g., Farnsworth et al., 2019; Zhu, Poulsen, & Tierney, 2019). Estimates of modern climate

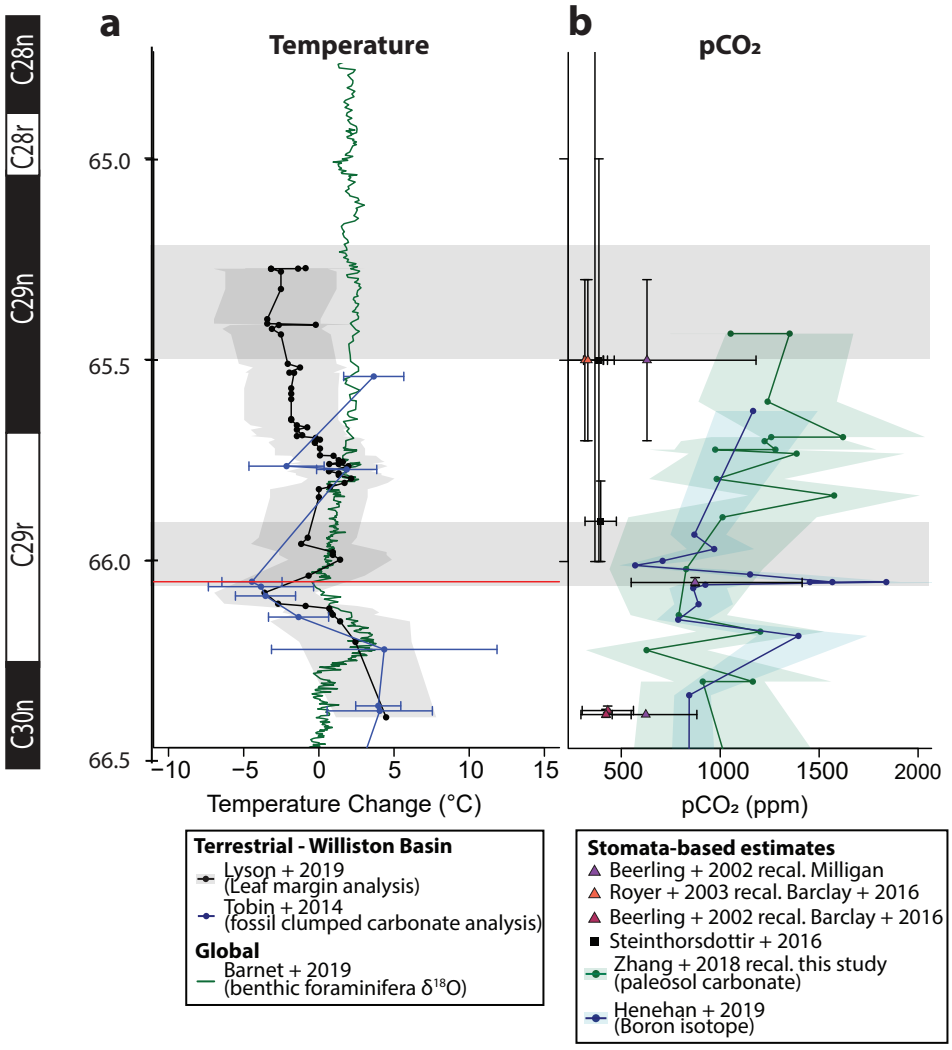

Figure 4.8: a) Temperature records from the Williston basin compared with a benthic oxygen isotope temperature record (potentially a more globally integrated signal). b) Compilation of global pCO_2 data with good chronologic constraints.

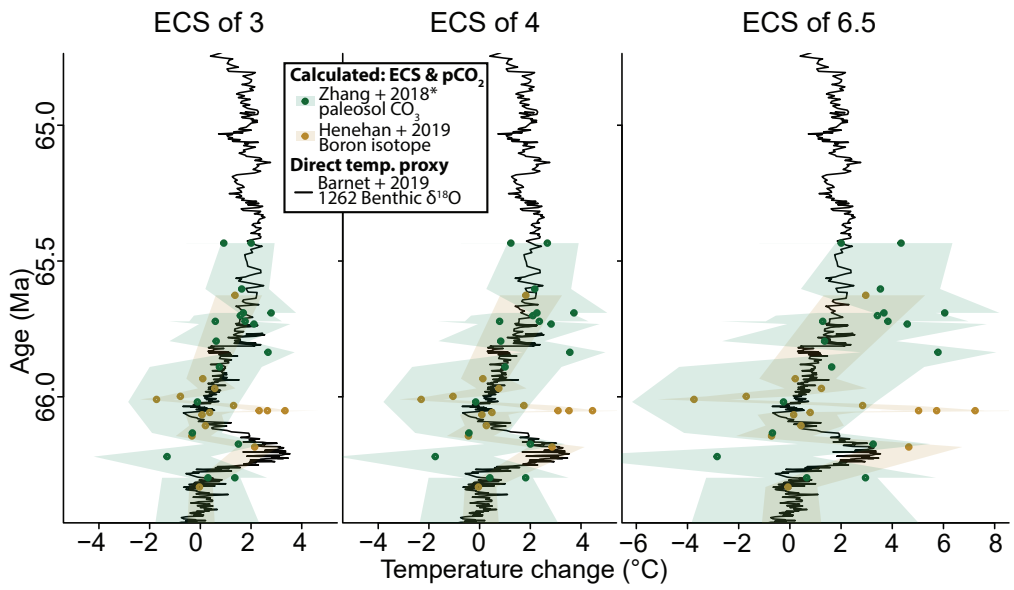

Figure 4.9: Comparison of the actual temperature change observed in a benthic foraminifer oxygen isotope record (Barnet et al., 2019) with the estimated temperature changing using each pCO_2 record and a given equilibrium climate sensitivity (ECS).

sensitivity using CMIP6 models range from 1.8 to 5.6 (Meehl et al., 2020). To evaluate our pCO_2 data, we use an initial pCO_2 of 850 ppm, approximately the value of both records before the Late Maastrichtian Warming Event (LMWE, ∼66.3 Ma in our age model). We compare the temperature change estimated using each pCO_2 record with the actual temperature change in the deep ocean, as represented by single-species benthic foraminifera $\delta^{18}O$ from IODP 1262 (Barnet et al., 2019, Section 3.2). The temperature change was calculated with respect to the median temperature in the 100 ka before the LMWE (8.13 °C).

We plot the estimated temperature changes calculated using both pCO_2 records, for climate sensitivities of 3,4, and 6.5 (Fig. 4.9). An ECS value of $\sim$ 4 °C is the most consistent with the observed temperature changes. 3°C is also fairly consistent, especially when applied to the Zhang et al. (2018) dataset. These ECS values are compatible with the expected values for the Danian and Maastrichtian of $\sim$ 4 to 5 (Farnsworth et al., 2019). A full analysis of climate sensitivity and the environmental parameters that affect it is beyond this study's scope. However, we note that an S of 4°C works equally well both before and after the mass extinction, especially for the Henehan et al. (2019) dataset. Therefore, climate sensitivity is not required to substantially change across the K-Pg boundary, as has been previously suggested (Farnsworth et al., 2019). The compatibility of the pCO_2 and temperature records highlights the necessity of ensuring consistency between age models when evaluating parameters like climate sensitivity. It also suggests that these higher pCO_2 values are more likely to be accurate than the lower stomata-based estimates.

In order to compare these pCO_2 changes with those required to cause the observed changes in

$\Delta^{13}C_{plant}$, we estimate the latter using the relationship between pCO_2 and $\Delta^{13}C_{plant}$ hypothesized by Schubert and Jahren (2012), as updated by Cui et al. (2020) (Section 3.5). In this model, pCO_2 increases cause an increase in $\Delta^{13}C_{plant}$. This relationship is corroborated by data from the past few hundred years, which suggests that $\Delta^{13}C_{plant}$ is currently increasing simultaneously with anthropogenic pCO_2 increases (Keeling et al., 2017). The results of this analysis compared with the estimates of pCO_2 from L. Zhang et al. (2018)and Henehan et al. (2019) demonstrates that the observed pCO_2 decrease after the boundary is not long-lasting enough to consistently explain the lower $\Delta^{13}C_{plant}$, which does not return to Maastrichtian values until $\sim$ 65.5 Ma.

Precipitation: we do not have records of paleoprecipitation across the K-Pg boundary. However, plant species assemblages suggest high precipitation (mean annual precipitation >1000 mm/yr) conditions in both the late Maastrichtian and early Paleocene in North America as well as China (Hao et al., 2010; Spicer & Collinson, 2014). Model analyses suggest similar values of $\sim$ 800 - 1400 mm/yr in Montana and southeastern France, the places of origin of the $\delta^{13}C_{org}$ records we utilize (Bardeen, Garcia, Toon, & Conley, 2017). Precipitation potentially dramatically decreased in the immediate aftermath of the Chicxulub impact; however, it likely increased to late Maastrichtian values within a few years (Bardeen et al., 2017).

Studies of the relationship between modern plant $\Delta^{13}C_{plant}$ and mean annual precipitation suggest that $\Delta^{13}C_{plant}$ linearly increases as precipitation increases logarithmically (Cornwell et al., 2018; Kohn, 2010). The slope of this relationship is close to 1, indicating that a change in $\Delta^{13}C_{plant}$ of $\sim$2‰ requires a change in mean annual precipitation (MAP) of nearly two orders of magnitude (Cornwell et al., 2018). With an initial MAP of $\sim$1000 mm/a precipitation would need to decrease to $\sim$10 mm/a at the K-Pg boundary and then slowly increase over the next 500 ka in order to cause the observed changes in $\Delta^{13}C_{plant}$. While the sudden change in $\Delta^{13}C_{plant}$ at the K-Pg boundary may be in part due to a dramatic decrease in precipitation, there is no evidence to suggest significantly decreased global precipitation lasted for longer than a few years. In particular, there are no significant lithology differences noted at the boundary that would suggest a decrease in precipitation. Instead, the abundant coal seams suggest more precipitation than 10 mm/a (Fig. 4.2). Additionally, leaf vein density increases across the K-Pg boundary, a feature that generally increases in wetter environments (Blonder, Royer, Johnson, Miller, & Enquist, 2014).

In conclusion, we find that environmental changes likely did not cause the differences in pattern between the terrestrial and marine $\delta^{13}C$ records. Instead, there was likely disequilibrium between the open ocean surface DIC pool, the atmosphere, and terrestrial plants.

4.5 Integrated view of carbon cycle recovery from K-Pg

4.5.1 Pre-K-Pg ($\sim$66.4-66.052 Ma)

This interval in the lead up to the K-Pg extinction experienced the Late Maastrichtian Warming Event (LMWE), in which there were several degrees of warming globally (e.g., Barnet et al., 2017; Hull et al., 2020; Wilf, Johnson, & Huber, 2003). This warming event is discernible in records of deep-sea temperature change as well as those from the Williston Basin (Barnet et al., 2017; Lyson

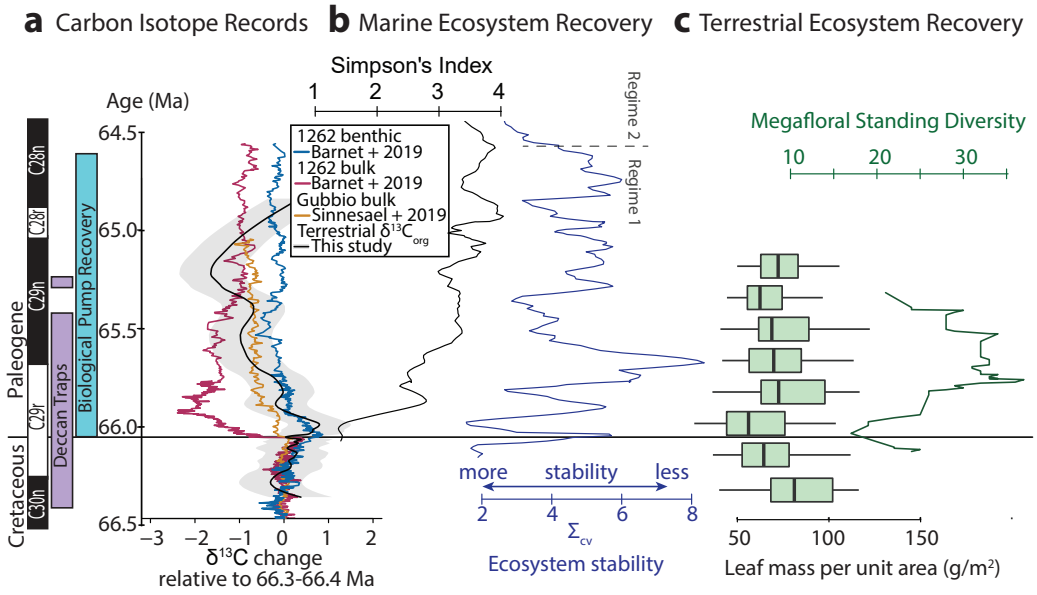

Figure 4.10: **a)** Change in δ^{13}C relative to 66.3-66.4 Ma, for terrestrial and marine records. The interval of main phase Deccan Traps eruptions and biological pump recovery are indicated by bars (Ch. 2 of this thesis, Birch et al., 2016; Sprain et al., 2019) Marine ecosystem recovery metrics from the the IODP 1209 core (S. A. Alvarez et al., 2019): a 150 ka moving average of community diversity (Simpson's index of evenness), and summed coefficient of variation (Σ_{CV}), which is a measure of variance in relative taxa abundance. S. A. Alvarez et al., 2019 indicates the end of high amplitude variability of ecosystem stability by the transition to Regime 2. **c)** Terrestrial ecosystem recovery metrics from the Denver Basin (Lyson et al., 2019): Leaf mass per unit area, which reflects carbon investment per leaf and photosynthetic capability, and megafloral standing diversity. The age model of each record, including biological pump recovery interval has been adjusted such that the K-Pg boundary and all magnetochron boundaries are isochronous throughout (Section 3.2).

et al., 2019; Tobin, Wilson, Eiler, & Hartman, 2014; Wilf et al., 2003). The LMWE is coincident with a slight decrease in marine carbonate δ^{13}C, superimposed on a longer-scale trend of increasing δ^{13}C. The small change in δ^{13}C associated with the LMWE is not observable in the $\delta^{13}C_{org}$ record (or in the marine-estimated $\delta^{13}C_{CO_2}$ record). However, the overall increasing trend is similar in magnitude between terrestrial and marine δ^{13}C records (Fig. 4.10).

$\Delta^{13}C_{plant}$ remains approximately constant until the K-Pg boundary. There is a slight increase in $\Delta^{13}C_{plant}$ approximately coincident with or just before the LMWE, which could be a result of the increase in pCO_2 - however, the observed pCO_2 increase ($\sim$ 500 ppm) is larger than the increase of $\sim$ 100 ppm required to produce the change in $\Delta^{13}C_{plant}$ (Fig. 4.7). Thus, the pCO_2 increase of the LMWE likely did not significantly influence plant carbon isotope discrimination. During this time interval, the overall stable δ^{13}C records suggest that the carbon cycle (and relative burial ratio of organic carbon/carbonate) was relatively unperturbed.

The LMWE corresponds with initiation of a decrease in plant diversity and leaf mass per unit area in the Denver Basin (Fig. 4.10). The decline in leaf mass per unit area suggests that deciduousness increased, and photosynthetic capacity per leaf decreased (e.g., Blonder et al., 2014; Lyson et al., 2019; Spicer & Collinson, 2014). The LMWE is coincident with the onset of main-phase Deccan volcanism (Barnet et al., 2019; Sprain et al., 2019; Schoene et al., 2019). While Deccan CO_2 release is invoked as a potential cause of the LMWE, the relatively constant $\delta^{13}C$ records suggest that the LMWE was not caused by a thermogenic release of light organic carbon, which would have caused a distinct carbon isotope excursion. This process has been invoked for warming caused by other Large Igneous Provinces and has recently been proposed for the Deccan Traps (e.g., Burgess, Muirhead, & Bowring, 2017; Eddy et al., 2020; Svensen et al., 2009). Hence, if caused by the Deccan Traps, the LMWE was more likely a result of the release of magmatically derived carbon, which would cause only a small amplitude change in $\delta^{13}C_{CO_2}$, as magmatic carbon and atmospheric carbon have similar isotopic compositions (Hull et al., 2020; Sprain et al., 2019). The latest Maastrichtian was a dynamic interval, with changing climate and plant assemblages (Spicer & Collinson, 2014). However, the overall stable $\delta^{13}C$ records suggest that the carbon cycle was relatively unperturbed.

4.5.2 Immediate aftermath (66.052-65.9 - first 150 ka)

The K-Pg extinction resulted in immediate and severe disruption of marine ecosystems. $\delta^{13}C$ in bulk marine carbonates immediately fell by $\sim$1‰, then decreased gradually until reaching a nadir approximately 100 ka after the K-Pg boundary (Fig. 4.5). Benthic foraminiferal $\delta^{13}C$ values gradually decrease by nearly 1‰ over the $\sim$150 ka post K-Pg extinction. The reduction in bulk and planktonic $\delta^{13}C$ values to similar or less than benthic $\delta^{13}C$ values requires a negative surface to deep carbon isotope gradient - a reversal of the latest Maastrichtian (e.g., Birch et al., 2016). Surface ocean pH also changes during this time interval, as indicated by the Henehan et al., (2019) record of planktonic foraminifer boron isotope composition. A transient acidification event coincides with the K-Pg boundary. It is then quickly followed by an increase in pH over the next $\sim$ 50 ka, overshooting late Maastrichtian values. The increase in the surface ocean's pH is attributed to the extinction of many calcifiers in the surface ocean, weakening that alkalinity sink (Henehan et al., 2019). It drives the pCO_2 decrease during the first 50 ka of the Paleocene. The pH then decreased, and pCO_2 increased, both returning to pre-boundary values over the following 80 ka. The combination of changes in $\delta^{13}C$ and pH surface to deep gradients is best explained by limited export productivity enhanced remineralization of organic material in the surface ocean (Esmeray-Senlet et al., 2015; Henehan et al., 2019). Further support for this conclusion comes from the highly variable ecosystem stability and low community diversity in open ocean marine environments (Fig. 4.10, S. A. Alvarez et al. (2019)).

These changes in export productivity were not globally homogeneous. Several shelf marine $\delta^{13}C$ records show a slightly different pattern than open ocean records, with an initial rebound from the negative excursion within 50 ka (Esmeray-Senlet et al., 2015; Sepúlveda et al., 2019). Then, $\sim$100 ka later, shelf marine $\delta^{13}C$ begins to decrease again (e.g., Coccioni et al., 2012;

Sinnesael et al., 2016). The differences between the shelf and open ocean $\delta^{13}C$ patterns may reflect different recovery dynamics between these environments, resulting in a heterogeneous ocean $\delta^{13}C$ composition (Esmeray-Senlet et al., 2015; Hull & Norris, 2011; Sepúlveda et al., 2019). This heterogeneity means that the $\delta^{13}C_{CO_2}$ calculated using open ocean bulk carbonate is likely not representative of the atmosphere, as a fundamental assumption in the calculation is that ocean DIC is in isotopic equilibrium globally.

Other than a possible very brief decrease in terrestrial $\delta^{13}C_{org}$ at the boundary, terrestrial $\delta^{13}C_{org}$ continues to increase for the first 50 ka after the K-Pg boundary (Fig. 4.10). $\delta^{13}C_{org}$ then falls by $\sim$ 1‰ over the next 100 ka, similar to benthic foraminiferal $\delta^{13}C_{cc}$. The brief drop in pH and rise in pCO_2 at the K-Pg boundary is likely the result of the Chicxulub impact, which also potentially decreased precipitation substantially during this short time interval (e.g., Bardeen et al., 2017; Beerling et al., 2002; Henehan et al., 2019; Milligan et al., 2019). However, pCO_2 soon decreased, and the magnitude of this decrease was possibly sufficient to cause the observed decrease in $\Delta^{13}C_{plant}$ at the K-Pg boundary (Fig. 4.7). This pCO_2 decrease possibly explains the lack of a negative excursion in terrestrial $\delta^{13}C$ during the immediate aftermath of the K-Pg extinction and Chicxulub impact. However, the difference in pattern between bulk carbonate $\delta^{13}C_{cc}$ and terrestrial $\delta^{13}C_{org}$ over the next few 100 ka cannot be explained by fluctuations in plant carbon isotope discrimination in response to pCO_2 or precipitation changes.

Another possible explanation is that during the 50 ka post-K-Pg extinction, the relative ratio of carbonate to organic carbon burial decreased due to the extinction of many marine calcifiers in the surface ocean. A decrease in the ratio of carbonate to organic carbon burial would cause an increase in atmospheric $\delta^{13}C$, due to decreased removal of isotopically heavier carbonate. However, this hypothesis is difficult to reconcile with shelf marine records, which do not show this increasing trend. As this increase in terrestrial $\delta^{13}C$ is possibly not a global trend, it requires further investigation with additional terrestrial records.

4.5.3 Early Recovery (65.9 to ∼65.5)

Between $\sim$ 65.9 Ma to 65.5 Ma, terrestrial $\delta^{13}C_{org}$ and benthic foraminiferal $\delta^{13}C_{cc}$ continue to decrease by nearly 1 ‰, while bulk marine $\delta^{13}C_{cc}$ increases (open ocean) or remains more or less constant (shelf) (Fig. 4.10). The differences between terrestrial and marine records are not easily explained using changes in pCO_2 or precipitation - as both are expected to reach or exceed pre-K-Pg values after ∼66 Ma (Bardeen et al., 2017; Henehan et al., 2019). Therefore, the different patterns require either disequilibrium processes between the surface ocean DIC pool and the atmosphere, or that the open ocean bulk carbonate $\delta^{13}C_{cc}$ values are not representative of the entire ocean. The latter is consistent with the "heterogeneous ocean" hypothesis (Esmeray-Senlet et al., 2015; Sepúlveda et al., 2019). In the high resolution open ocean records, S. A. Alvarez et al. (2019) find that although the community diversity is steadily increasing, the marine ecosystems are highly unstable with rapid changes in abundance of various nanoplankton taxa (Fig. 4.10).

While the slope is different, the decreases in both benthic foraminiferal $\delta^{13}C_{cc}$ and terrestrial $\delta^{13}C_{org}$ suggest that atmospheric $\delta^{13}C_{CO_2}$ is most likely also decreasing during this time interval,

rather than increasing like open ocean bulk carbonate $\delta^{13}C_{cc}$. The continual decrease in benthic foraminiferal $\delta^{13}C_{cc}$ is attributed to a decrease in global productivity and, therefore, in the burial of organic material relative to carbonate (e.g., Esmeray-Senlet et al., 2015). If atmospheric $\delta^{13}C_{CO_2}$ is also decreasing during this time, then it suggests that global productivity and hence organic carbon fixation has not returned to pre-K-Pg levels.

Perhaps this is unsurprising as this is a turbulent period for marine and terrestrial ecosystems (Fig. 4.10). Multiple minor hyperthermal events correspond with marine carbon isotope excursions, such as the Danian-C2 and lower chron C29n events, although it is debated if they had global effects (Barnet et al., 2019; Sinnesael et al., 2019). Additionally, a significant portion of the volume of Deccan Traps basalt is erupted during this time window, before the end of the main phase eruptions around $\sim$ 65.5 Ma, with some large eruptions occurring as late as 65.3 Ma (Fendley et al., 2020; Schoene et al., 2019; Sprain et al., 2019). Despite these environmental perturbations, ecological recovery is underway. Plant diversity increases through the end of chron C29r when it reaches pre-LMWE levels (Fig. 4.10). Terrestrial faunal recovery has also begun - maximum mammalian body mass increases until $\sim$ 65.5 Ma (Lyson et al., 2019; Smith et al., 2018) (See Fig. 4.10). Partial recovery of export productivity is indicated by a negative surface to deep carbon isotope gradient within open ocean carbon isotope records (Birch et al., 2016).

4.5.4 After 65.5 Ma

After $\sim$ 65.5 Ma benthic foraminiferal and bulk carbonate $\delta^{13}C_{cc}$ increase slightly for $\sim$250 ka, after which they are mostly constant. However, terrestrial $\delta^{13}C_{org}$ continues to decrease for another $\sim$ 250 ka until about 64.25 Ma. Due to the opposing trends between terrestrial and marine $\delta^{13}C$, the calculated $\Delta^{13}C_{plant}$ overshoots its end-Maastrichtian value. The relatively constant temperature derived from benthic foraminiferal $\delta^{18}O_{cc}$ suggests there was no significant change in pCO_2, as would be required to increase $\Delta^{13}C_{plant}$ via enhanced carbon isotope discrimination in plants at higher pCO_2 levels. The increase in marine $\delta^{13}C$ could be due to a combination of increased marine productivity in the surface ocean with increased efficacy of the biologic pump. This combination likely increased organic carbon burial relative to carbonate in the ocean. If this recovery was more pronounced in the ocean than in terrestrial ecosystems, it could partially explain the earlier initiation of $\delta^{13}C$ increase.

The increase in terrestrial $\delta^{13}C_{org}$ may begin earlier than our record indicates. This hypothesis is supported by the Boltysh crater $\delta^{13}C_{org}$ record, in which the increase begins around 65.5 Ma. However, the age model in the Boltysh section is more uncertain (Section 3.2). The $\delta^{13}C_{org}$ increase in our Montana record is relatively far from the nearest chronologic tie points at the start and end of chron C29n and closest dated tephra layers at 65.12 and 65.70 Ma (Sprain et al., 2015, 2018). Hence the exact timing of this transition relies strongly on our assumption of linear sediment accumulation rates. Regardless of exactly when the increase in $\delta^{13}C_{org}$ initiated, it persists through chron C28r.

By midway through C29n, Danian nannoplankton have significantly diversified post-K-Pg, the community structure is relatively stable, and the leaf mass per unit area of terrestrial plants has returned to pre-LMWE levels (Lyson et al., 2019; S. A. Alvarez et al., 2019). These metrics

support the assertion of increasing primary productivity, and the corresponding increase of burial of organic carbon relative to carbonate, suggested by the increases in terrestrial and marine $\delta^{13}C$. Some measure of stability has likely been achieved in the global carbon cycle, and the biological pump recovers within $\sim$ 200 ka, by early chron C28n (Fig. 4.10).

4.6 Conclusions

The carbon isotope composition of atmospheric carbon ($\delta^{13}C_{CO_2}$) across the end-Cretaceous mass extinction is an essential constraint in our understanding of climate and ecological changes during the extinction and recovery intervals. The patterns both pre- and post-K-Pg boundary in benthic foraminiferal and terrestrial $\delta^{13}C$ are similar until the end of chron C29r, suggesting actual atmospheric $\delta^{13}C_{CO_2}$ values followed a similar trend. This pattern includes a gradual decrease in $\delta^{13}C$ after the K-Pg boundary, which is significantly different from the sudden negative excursion recorded in open ocean marine bulk carbonate $\delta^{13}C_{cc}$.

The differences between terrestrial and open ocean marine bulk carbonate $\delta^{13}C$ are unlikely to have been caused by changes in plant carbon isotope discrimination due to changing environmental conditions. We compiled pCO_2 records and precipitation estimates from around the K-Pg boundary, and compared them to estimates of the pCO_2 or precipitation changes required to cause the different trends between terrestrial $\delta^{13}C_{org}$ and the $\delta^{13}C_{CO_2}$ calculated using open ocean bulk carbonate $\delta^{13}C_{cc}$. As a result of this discrepancy, we hypothesize that the isotopic composition of the open ocean surface DIC pool was not in isotopic equilibrium during this time interval. The sudden excursion in open ocean bulk carbonate $\delta^{13}C_{cc}$ records may mask any changes in $\delta^{13}C_{CO_2}$.

The terrestrial $\delta^{13}C$ records do not support a rapid ($<$100 ka post-K-Pg boundary) recovery of the carbon cycle and global primary productivity. Instead, benthic foraminiferal and terrestrial $\delta^{13}C$ values continue to decrease until at least 65.5 Ma, suggesting that the carbon cycle likely did not fully recover until after 65 Ma when terrestrial $\delta^{13}C$ returns to pre-boundary values. The slow recovery in primary productivity and organic carbon burial before $\sim$ 65.5 Ma is supported by the ongoing marine and terrestrial ecosystem recovery through this time interval (S. A. Alvarez et al., 2019; Lyson et al., 2019). This slow recovery could be due in part to the eruption of the $\sim$75% of the Deccan Traps between the K-Pg boundary and $\sim$65.5 Ma, creating inhospitable climate conditions (Hull et al., 2020; Richards et al., 2015; Schmidt et al., 2016; Sprain et al., 2019).

Chapter 5

Conclusion

In this thesis I have investigated the effects of the Deccan Traps large igneous province eruptions around the Cretaceous-Paleogene mass extinction and recovery.

Chapter one evaluated the potential of these eruptions to cause climate and ecological changes to be very close to the extinction event by creating high-resolution mercury concentration records. These show that mercury concentration increases indicative of Deccan eruptions occurred both before and after the Cretaceous-Paleogene boundary, including within tens of thousands of years around the mass extinction. I used a global mercury box model to estimate the CO_2 and SO_2 emissions that likely corresponded with the mercury release required to produce the observed concentration changes. These mercury emissions could have coincided with eruptions with magma output fluxes of 50-250 km^3/a, lasted 100-500 years, and occurred at least every 10,000 years. The SO_2 emissions were sufficient to cause significant ($\sim$ 1-5°C cooling for the duration of each eruption. If these colder periods occurred as predicted, these frequent climate perturbations in this critical interval might have affected ecosystems.

In chapter two, I described a new chronostratigraphy for the Rajahmundry Traps, potentially the most voluminous individual Deccan Traps eruptions. I constrained the timing of these flows relative to the Cretaceous-Paleogene mass extinction through radioisotopic dating, magnetostratigraphy, and biostratigraphy. My data has shown that each known Rajahmundry eruption occurred after the mass extinction, during the recovery interval. As the timing of these eruptions suggests they could have affected ecological recovery, I used a carbon cycle model to test whether these eruptions could have caused climate warming. These results showed that eruptive CO_2 emissions likely did not cause multi-degree warming, though SO_2 emitted likely caused cooling. However, Earth-system feedbacks could have amplified the climate effects of Deccan eruptions, causing carbon cycle perturbations.

In chapter 3, I investigated the long-term carbon cycle dynamics around the mass extinction and recovery intervals. The carbon isotope composition of atmospheric CO_2 is a key constraint in our understanding of climate and ecological changes during this time interval. Both biotic changes, such as the mass extinction, and abiotic events, such as the Deccan eruptions, could have changed atmospheric $\delta^{13}C_{CO_2}$. I investigated these changes using the carbon isotope composition

of terrestrial organic carbon. I found that the trends in $\delta^{13}\mathrm{C}$ were similar between benthic marine and terrestrial records through the latest Maastrichtian through the end of chron C29r. I found that while the terrestrial excursion duration is similar to the period of reduced export productivity, the shape of the excursion is quite different between terrestrial and bulk marine carbonate $\delta^{13}\mathrm{C}$. These differences suggest the open-ocean DIC pool and the atmosphere were in partial disequilibrium. Additionally, my data demonstrate that the carbon cycle did not recover fully until after $\sim$ 65 Ma. The slow carbon cycle recovery could be partially due to the ongoing Deccan Traps eruptions.

Bibliography

Abels, H. A., Clyde, W. C., Gingerich, P. D., Hilgen, F. J., Fricke, H. C., Bowen, G. J., & Lourens, L. J. (2012). Terrestrial carbon isotope excursions and biotic change during Palaeogene hyperthermals. *Nature Geoscience*, *5*(5), 326–329. Retrieved from https://doi.org/10.1038/ngeo1427 doi: 10.1038/ngeo1427

Alvarez, L. W. (1983). Experimental Evidence that an Asteroid Impact Led to the Extinction of Many Species 65 Million Years Ago. *Proceedings of the National Academy of Sciences*, *80*(2), 627–642. Retrieved from http://www.jstor.org/stable/13524 doi: 10.1073/pnas.80.2.627

Alvarez, L. W., Alvarez, W., Asaro, F., & Michel, H. V. (1980, 6). Extraterrestrial Cause for the Cretaceous-Tertiary Extinction. *Science*, *208*(4448), 1095 LP - 1108. Retrieved from http://science.sciencemag.org/content/208/4448/1095.abstract doi: 10.1126/science.208.4448.1095

Alvarez, S. A., Gibbs, S. J., Bown, P. R., Kim, H., Sheward, R. M., & Ridgwell, A. (2019). Diversity decoupled from ecosystem function and resilience during mass extinction recovery. *Nature*, *574*(7777), 242–245. Retrieved from https://doi.org/10.1038/s41586-019-1590-8 doi: 10.1038/s41586-019-1590-8

Amos, H. M., Jacob, D. J., Kocman, D., Horowitz, H. M., Zhang, Y., Dutkiewicz, S., ... Sunderland, E. M. (2014, 8). Global Biogeochemical Implications of Mercury Discharges from Rivers and Sediment Burial. *Environmental Science & Technology*, *48*(16), 9514–9522. Retrieved from https://doi.org/10.1021/es502134t doi: 10.1021/es502134t

Amos, H. M., Jacob, D. J., Streets, D. G., & Sunderland, E. M. (2013, 4). Legacy impacts of all-time anthropogenic emissions on the global mercury cycle. *Global Biogeochemical Cycles*, *27*(2), 410–421. Retrieved from https://doi.org/10.1002/gbc.20040 doi: 10.1002/gbc.20040

Amos, H. M., Sonke, J. E., Obrist, D., Robins, N., Hagan, N., Horowitz, H. M., ... Sunderland, E. M. (2015, 4). Observational and Modeling Constraints on Global Anthropogenic Enrichment of Mercury. *Environmental Science & Technology*, *49*(7), 4036–4047. Retrieved from https://doi.org/10.1021/es5058665 doi: 10.1021/es5058665

Archer, D., Eby, M., Brovkin, V., Ridgwell, A., Cao, L., Mikolajewicz, U., ... Tokos, K. (2009, 4). Atmospheric Lifetime of Fossil Fuel Carbon Dioxide. *Annual Review of Earth and Planetary Sciences*, *37*(1), 117–134. Retrieved from https://doi.org/10.1146/annurev.earth.031208.100206 doi: 10.1146/an-

nurev.earth.031208.100206

Arenillas, I., Arz, J., & Molina, E. (2004, 3). A new high-resolution planktic foraminiferal zonation and subzonation for the lower Danian. *Lethaia*, *37*(1), 79–95. Retrieved from https://doi.org/10.1080/00241160310005097 doi: 10.1080/00241160310005097

Arenillas, I., & Arz, J. A. (2017, 1). Benthic origin and earliest evolution of the first planktonic foraminifera after the Cretaceous/Palaeogene boundary mass extinction. *Historical Biology*, *29*(1), 25–42. Retrieved from https://doi.org/10.1080/08912963.2015.1119133 doi: 10.1080/08912963.2015.1119133

Arenillas, I., Arz, J. A., & Gilabert, V. (2017). Revalidation of the genus Chiloguembelitria Hofker: Implications for the evolution of early Danian planktonic foraminifera. *Journal of African Earth Sciences*, *134*, 435–456. Retrieved from http://www.sciencedirect.com/science/article/pii/S1464343X17302972 doi: 10.1016/j.jafrearsci.2017.07.011

Arenillas, I., Arz, J. A., & Gilabert, V. (2018). Blooms of aberrant planktic foraminifera across the K/Pg boundary in the Western Tethys: causes and evolutionary implications. *Paleobiology*, *44*(3), 460–489. doi: 10.1017/pab.2018.16

Arens, N. C., & Jahren, A. H. (2000). Carbon Isotope Excursion in Atmospheric CO2 at the Cretaceous-Tertiary Boundary: Evidence from Terrestrial Sediments. *Palaios*, *15*(4), 314–322.

Arens, N. C., & Jahren, A. H. (2002). Chemostratigraphic correlation of four fossil-bearing sections in southwestern North Dakota. *Geological Society of America Special Papers*, *361*, 75–93. doi: 10.1130/0-8137-2361-2.75

Arens, N. C., Jahren, A. H., & Kendrick, D. C. (2014). Carbon isotope stratigraphy and correlation of plant megafossil localities in the Hell Creek Formation of eastern Montana , USA. *Geological Society of America Special Papers*, *503*, 149–171. Retrieved from http://specialpapers.gsapubs.org/content/503/149.abstract doi: 10.1130/2014.2503(05).

Arinobu, T., Ishiwatari, R., Kaiho, K., & Lamolda, M. A. (1999, 8). Spike of pyrosynthetic polycyclic aromatic hydrocarbons associated with an abrupt decrease in δ13C of a terrestrial biomarker at the Cretaceous-Tertiary boundary at Caravaca, Spain. *Geology*, *27*(8), 723–726. Retrieved from http://dx.doi.org/10.1130/0091-7613(1999)027http://0.0.0.2 doi: 10.1130/0091-7613(1999)027<0723:SOPPAH>2.3.CO;2

Artemieva, N., & Morgan, J. (2017, 10). Quantifying the Release of Climate-Active Gases by Large Meteorite Impacts With a Case Study of Chicxulub. *Geophysical Research Letters*, *44*(20), 180–10. Retrieved from https://doi.org/10.1002/2017GL074879 doi: 10.1002/2017GL074879

Bagnato, E., Aiuppa, A., Parello, F., Allard, P., Shinohara, H., Liuzzo, M., & Giudice, G. (2011). New clues on the contribution of Earth's volcanism to the global mercury cycle. *Bulletin of Volcanology*, *73*(5), 497–510. Retrieved from https://doi.org/10.1007/s00445-010-0419-y doi: 10.1007/s00445-010-0419-y

Bagnato, E., Tamburello, G., Avard, G., Martinez-Cruz, M., Enrico, M., Fu, X., ... Sonke, J. E. (2014, 8). Mercury fluxes from volcanic and geothermal sources: an

update. *Geological Society, London, Special Publications*, *410*. Retrieved from http://sp.lyellcollection.org/content/early/2014/08/01/SP410.2.abstract doi: 10.1144/SP410.2

Bailey, J. V., Cohen, A. S., & Kring, D. A. (2005). Lacustrine Fossil Preservation in Acidic Environments: Implications of Experimental and Field Studies for the Cretaceous–Paleogene Boundary Acid Rain Trauma. *PALAIOS*, *20*(4), 376–389. Retrieved from https://doi.org/10.2110/palo.2003.p03-88 doi: 10.2110/palo.2003.p03-88

Baksi, A. K. (2001). The Rajahmundry Traps , Andhra Pradesh: Evaluation of their petrogenesis relative to the Deccan Traps. *Proceedings of the Indian Academy of Sciences*, *110*(4), 397–407. Retrieved from https://doi.org/10.1007/BF02702903 doi: 10.1007/BF02702903

Baksi, A. K., Byerly, G. R., Chan, L.-H., & Farrar, E. (1994, 7). Intracanyon flows in the Deccan province, India? Case history of the Rajahmundry Traps. *Geology*, *22*(7), 605–608. Retrieved from https://doi.org/10.1130/0091-7613(1994)022http://0.0.0.2 doi: 10.1130/0091-7613(1994)022<0605:IFITDP>2.3.CO;2

Barclay, R. S., & Wing, S. L. (2016). Improving the Ginkgo CO2 barometer: Implications for the early Cenozoic atmosphere. *Earth and Planetary Science Letters*, *439*, 158–171. Retrieved from http://www.sciencedirect.com/science/article/pii/S0012821X16000285 doi: doi.org/10.1016/j.epsl.2016.01.012

Bardeen, C. G., Garcia, R. R., Toon, O. B., & Conley, A. J. (2017, 9). On transient climate change at the cretaceous-paleogene boundary due to atmospheric soot injections. *Proceedings of the National Academy of Sciences*, *114*(36), E7415 LP - E7424. Retrieved from http://www.pnas.org/content/114/36/E7415.abstract doi: 10.1073/pnas.1708980114

Barnet, J., Littler, K., Kroon, D., Leng, M. J., Westerhold, T., Röhl, U., & Zachos, J. C. (2017, 12). A new high-resolution chronology for the late Maastrichtian warming event: Establishing robust temporal links with the onset of Deccan volcanism. *Geology*, *46*(2), 147–150. Retrieved from http://dx.doi.org/10.1130/G39771.1 doi: 10.1130/G39771.1

Barnet, J., Littler, K., Westerhold, T., Kroon, D., Leng, M., Bailey, I., ... Zachos, J. (2019). A High-Fidelity Benthic Stable Isotope Record of Late Cretaceous–Early Eocene Climate Change and Carbon-Cycling. *Paleoceanography and Paleoclimatology*, *34*, 672–691. doi: 10.1029/2019PA003556

Barral, A., Gomez, B., Legendre, S., & Lécuyer, C. (2017). Evolution of the carbon isotope composition of atmospheric CO2 throughout the Cretaceous. *Palaeogeography, Palaeoclimatology, Palaeoecology*, *471*, 40–47. Retrieved from http://www.sciencedirect.com/science/article/pii/S0031018216304850 doi: 10.1016/j.palaeo.2017.01.034

Bataille, C. P., Watford, D., Ruegg, S., Lowe, A., & Bowen, G. J. (2016). Chemostratigraphic age model for the Tornillo Group: A possible link between fluvial stratigraphy and climate. *Palaeogeography, Palaeoclimatology, Palaeoecology*, *457*, 277–289. Retrieved from http://www.sciencedirect.com/science/article/pii/S0031018216302152 doi: https://doi.org/10.1016/j.palaeo.2016.06.023

Beane, J. E., Turner, C. A., Hooper, P. R., Subbarao, K. V., & Walsh, J. N. (1986). Stratigraphy, composition and form of the Deccan Basalts, Western Ghats, India. *Bulletin of Volcanology*, *48*, 61–83. Retrieved from https://doi.org/10.1007/BF01073513 doi: 10.1007/BF01073513

Beerling, D. J., Lomax, B. H., Royer, D. L., Upchurch, G. R., & Kump, L. R. (2002, 6). An atmospheric pCO2 reconstruction across the Cretaceous-Tertiary boundary from leaf megafossils. *Proceedings of the National Academy of Sciences*, *99*(12), 7836 LP - 7840. Retrieved from http://www.pnas.org/content/99/12/7836.abstract doi: 10.1073/pnas.122573099

Belcher, C. M., Collinson, M. E., Sweet, A. R., Hildebrand, A. R., & Scott, A. C. (2003, 12). Fireball passes and nothing burns—The role of thermal radiation in the Cretaceous-Tertiary event: Evidence from the charcoal record of North America. *Geology*, *31*(12), 1061–1064. Retrieved from http://dx.doi.org/10.1130/G19989.1 doi: 10.1130/G19989.1

Belcher, C. M., Finch, P., Collinson, M. E., Scott, A. C., & Grassineau, N. V. (2009, 2). Geochemical evidence for combustion of hydrocarbons during the K-T impact event. *Proceedings of the National Academy of Sciences*, *106*(11), 4112–4117. Retrieved from http://www.pnas.org/content/early/2009/02/25/0813117106.abstract doi: 10.1073/pnas.0813117106

Berggren, W. A., & Pearson, P. N. (2005, 10). A revised tropical to subtropical Paleogene planktonic foraminiferal zonation. *Journal of Foraminiferal Research*, *35*(4), 279–298. Retrieved from https://doi.org/10.2113/35.4.279 doi: 10.2113/35.4.279

Bhalla, S. N. (1966). Foraminifera from the Infra-Trappean Beds of the Pangadi Area, India. *Journal of Paleontology*, *40*(2), 343–353. Retrieved from http://www.jstor.org/stable/1301666

Birch, H. S., Coxall, H. K., Pearson, P. N., Kroon, D., & Schmidt, D. N. (2016). Partial collapse of the marine carbon pump after the Cretaceous-Paleogene boundary. *Geology*, *44*(4), 287–290. Retrieved from http://geology.gsapubs.org/lookup/doi/10.1130/G37581.1 doi: 10.1130/G37581.1

Black, B. A., Neely, R. R., Lamarque, J. F., Elkins-Tanton, L. T., Kiehl, J. T., Shields, C. A., ... Bardeen, C. (2018). Systemic swings in end-Permian climate from Siberian Traps carbon and sulfur outgassing. *Nature Geoscience*, *11*, 949–954. doi: 10.1038/s41561-018-0261-y

Blandford, W. T. (1867). On the traps and intertrappean beds of western and central India. *Memoirs of the Geological Survey of India*, *6*, 137–162.

Blonder, B., Royer, D. L., Johnson, K. R., Miller, I., & Enquist, B. J. (2014, 9). Plant Ecological Strategies Shift Across the Cretaceous–Paleogene Boundary. *PLOS Biology*, *12*(9), e1001949. Retrieved from https://doi.org/10.1371/journal.pbio.1001949 doi: 10.1371/journal.pbio.1001949

Bowles, J. (2006). Data report: Revised magnetostratigraphy and magnetic mineralogy of sediments from Walvis Ridge, Leg 208. *Proceedings of the Ocean Drilling Program, Scientific Results*, *208*, 1–24.

Burgess, S. D., Muirhead, J. D., & Bowring, S. A. (2017). Initial pulse of Siberian Traps sills as the trigger of the end-Permian mass extinction. *Nature Communications*, *8*(1), 164.

Capriolo, M., Marzoli, A., Aradi, L. E., Callegaro, S., Dal Corso, J., Newton, R. J., ... Szabó, C. (2020). Deep CO2 in the end-Triassic Central Atlantic Magmatic Province. *Nature Communications*, *11*(1), 1670. Retrieved from https://doi.org/10.1038/s41467-020-15325-6 doi: 10.1038/s41467-020-15325-6

Carvajal-Ortiz, H., Mora, G., & Jaramillo, C. (2009). A molecular evaluation of bulk organic carbon-isotope chemostratigraphy for terrestrial correlations: An example from two Paleocene–Eocene tropical sequences. *Palaeogeography, Palaeoclimatology, Palaeoecology*, *277*(3), 173–183. Retrieved from http://www.sciencedirect.com/science/article/pii/S0031018209001138 doi: 10.1016/j.palaeo.2009.03.015

Chen, L., Zhang, W., Zhang, Y., Tong, Y., Liu, M., Wang, H., ... Wang, X. (2018). Historical and future trends in global source-receptor relationships of mercury. *Science of The Total Environment*, *610-611*, 24–31. Retrieved from http://www.sciencedirect.com/science/article/pii/S0048969717318855 doi: 10.1016/j.scitotenv.2017.07.182

Coccioni, R., Bancalà, G., Catanzarit, R., Fornaciari, E., Frontalini, F., Giusberti, L., ... Sprovieri, M. (2012, 10). An integrated stratigraphic record of the Palaeocene–lower Eocene at Gubbio (Italy): new insights into the early Palaeogene hyperthermals and carbon isotope excursions. *Terra Nova*, *24*(5), 380–386. Retrieved from https://doi.org/10.1111/j.1365-3121.2012.01076.x doi: 10.1111/j.1365-3121.2012.01076.x

Coccioni, R., Frontalini, F., Bancalà, G., Fornaciari, E., Jovane, L., & Sprovieri, M. (2010). The Dan-C2 hyperthermal event at Gubbio (Italy): Global implications, environmental effects, and cause(s). *Earth and Planetary Science Letters*, *297*(1), 298–305. Retrieved from http://www.sciencedirect.com/science/article/pii/S0012821X10004061 doi: 10.1016/j.epsl.2010.06.031

Coccioni, R., & Premoli Silva, I. (2015). Revised Upper Albian–Maastrichtian planktonic foraminiferal biostratigraphy and magneto-stratigraphy of the classical Tethyan Gubbio section (Italy). *Newsletters on Stratigraphy*, *48*(1), 47–90. doi: 10.1127/nos/2015/0055

Cornwell, W. K., Wright, I. J., Turner, J., Maire, V., Barbour, M. M., Cernusak, L. A., ... Santiago, L. S. (2018, 9). Climate and soils together regulate photosynthetic carbon isotope discrimination within C3 plants worldwide. *Global Ecology and Biogeography*, *27*(9), 1056–1067. Retrieved from https://doi.org/10.1111/geb.12764 doi: 10.1111/geb.12764

Cossa, D., Coquery, M., Gobeil, C., & Martin, J.-M. (1996). Mercury fluxes at the ocean margins. In W. Baeyens, R. Ebinghaus, & O. Vasiliev (Eds.), *Global and regional mercury cycles: sources, fluxes and mass balances* (pp. 229–247). Dordrecht: Springer Netherlands. doi: 10.1007/978-94-009-1780-4_11

Costa, A., Smith, V. C., Macedonio, G., & Matthews, N. E. (2014). The magnitude and impact of the Youngest Toba Tuff super-eruption. *Frontiers in Earth Science*, *2*, 16. Retrieved from https://www.frontiersin.org/article/10.3389/feart.2014.00016 doi: 10.3389/feart.2014.00016

Courtillot, V., Besse, J., Vandamme, D., Montigny, R., Jaeger, J.-J., & Cap-

petta, H. (1986). Deccan flood basalts at the Cretaceous/Tertiary boundary? *Earth and Planetary Science Letters*, *80*(3), 361–374. Retrieved from http://www.sciencedirect.com/science/article/pii/0012821X86901184 doi: https://doi.org/10.1016/0012-821X(86)90118-4

Cox, K. G., & Hawkesworth, C. J. (1985, 5). Geochemical Stratigraphy of the Deccan Traps at Mahabaleshwar, Western Ghats, India, with Implications for Open System Magmatic Processes. *Journal of Petrology*, *26*(2), 355–377. Retrieved from https://doi.org/10.1093/petrology/26.2.355 doi: 10.1093/petrology/26.2.355

Cui, Y., & Schubert, B. A. (2016). Quantifying uncertainty of past pCO2 determined from changes in C3 plant carbon isotope fractionation. *Geochimica et Cosmochimica Acta*, *172*, 127–138. Retrieved from http://www.sciencedirect.com/science/article/pii/S0016703715005694 doi: https://doi.org/10.1016/j.gca.2015.09.032

Cui, Y., Schubert, B. A., & Jahren, A. H. (2020). A 23 m.y. record of low atmospheric CO2. *Geology*. Retrieved from https://doi.org/10.1130/G47681.1 doi: 10.1130/G47681.1

Daga, R., Ribeiro Guevara, S., Pavlin, M., Rizzo, A., Lojen, S., Vreča, P., ... Arribére, M. (2016). Historical records of mercury in southern latitudes over 1600years: Lake Futalaufquen, Northern Patagonia. *Science of The Total Environment*, *553*, 541–550. Retrieved from http://www.sciencedirect.com/science/article/pii/S0048969716303242 doi: 10.1016/j.scitotenv.2016.02.114

Deschamps, A., Grigné, C., Le Saout, M., Soule, S. A., Allemand, P., Van Vliet-Lanoe, B., & Floc'h, F. (2014, 6). Morphology and dynamics of inflated subaqueous basaltic lava flows. *Geochemistry, Geophysics, Geosystems*, *15*(6), 2128–2150. Retrieved from https://doi.org/10.1002/2014GC005274 doi: 10.1002/2014GC005274

Devey, C. W., & Lightfoot, P. C. (1986). Volcanological and tectonic control of stratigraphy and structure in the western Deccan traps. *Bulletin of Volcanology*, *48*(4), 195–207. Retrieved from https://doi.org/10.1007/BF01087674 doi: 10.1007/BF01087674

Dinarès-Turell, J., Westerhold, T., Pujalte, V., Röhl, U., & Kroon, D. (2014). Astronomical calibration of the Danian stage (Early Paleocene) revisited: Settling chronologies of sedimentary records across the Atlantic and Pacific Oceans. *Earth and Planetary Science Letters*, *405*, 119–131. Retrieved from http://www.sciencedirect.com/science/article/pii/S0012821X14005330 doi: 10.1016/j.epsl.2014.08.027

Driscoll, C. T., Han, Y.-J., Chen, C. Y., Evers, D. C., Lambert, K. F., Holsen, T. M., ... Munson, R. K. (2007, 1). Mercury Contamination in Forest and Freshwater Ecosystems in the Northeastern United States. *BioScience*, *57*(1), 17–28. Retrieved from http://dx.doi.org/10.1641/B570106 doi: 10.1641/B570106

Eddy, M. P., Schoene, B., Samperton, K. M., Keller, G., Adatte, T., & Khadri, S. F. R. (2020). U-Pb zircon age constraints on the earliest eruptions of the Deccan Large Igneous Province, Malwa Plateau, India. *Earth and Planetary Science Letters*, *540*, 116249. Retrieved from http://www.sciencedirect.com/science/article/pii/S0012821X20301928 doi: doi.org/10.1016/j.epsl.2020.116249

Esmeray-Senlet, S., Wright, J. D., Olsson, R. K., Miller, K. G., Browning, J. V., & Quan, T. M. (2015, 6). Evidence for reduced export productivity following the Cretaceous/Paleogene mass extinction. *Paleoceanography*, *30*(6), 718–738. Retrieved from https://doi.org/10.1002/2014PA002724 doi: 10.1002/2014PA002724

Farnsworth, A., Lunt, D. J., O'Brien, C. L., Foster, G. L., Inglis, G. N., Markwick, P., ... Robinson, S. A. (2019, 8). Climate Sensitivity on Geological Timescales Controlled by Nonlinear Feedbacks and Ocean Circulation. *Geophysical Research Letters*, *46*(16), 9880–9889. Retrieved from https://doi.org/10.1029/2019GL083574 doi: 10.1029/2019GL083574

Fastovsky, D. E., & Bercovici, A. (2016). The Hell Creek Formation and its contribution to the Cretaceous–Paleogene extinction: A short primer. *Cretaceous Research*, *57*, 368–390. Retrieved from http://www.sciencedirect.com/science/article/pii/S0195667115300306 doi: 10.1016/j.cretres.2015.07.007

Fendley, I. M., Mittal, T., Sprain, C. J., Marvin-DiPasquale, M., Tobin, T. S., & Renne, P. R. (2019). Constraints on the volume and rate of Deccan Traps flood basalt eruptions using a combination of high-resolution terrestrial mercury records and geochemical box models. *Earth and Planetary Science Letters*, *524*, 115721. Retrieved from http://www.sciencedirect.com/science/article/pii/S0012821X19304133 doi: https://doi.org/10.1016/j.epsl.2019.115721

Fendley, I. M., Sprain, C. J., Renne, P. R., Arenillas, I., Arz, J. A., Gilabert, V., ... Mittal, T. (2020). No Cretaceous-Paleogene Boundary in Exposed Rajahmundry Traps: A Refined Chronology of the Longest Deccan Lava Flows From 40Ar/39Ar Dates, Magnetostratigraphy, and Biostratigraphy. *Geochemistry, Geophysics, Geosystems*. Retrieved from https://doi.org/10.1029/2020GC009149 doi: 10.1029/2020GC009149

Fischer, T. P., & Aiuppa, A. (2020, 3). AGU Centennial Grand Challenge: Volcanoes and Deep Carbon Global CO2 Emissions From Subaerial Volcanism—Recent Progress and Future Challenges. *Geochemistry, Geophysics, Geosystems*, *21*(3), e2019GC008690. Retrieved from https://doi.org/10.1029/2019GC008690 doi: 10.1029/2019GC008690

Fisher, R. A. (1953, 5). Dispersion on a sphere. *Proceedings of the Royal Society of London. Series A. Mathematical and Physical Sciences*, *217*(1130), 295–305. Retrieved from https://doi.org/10.1098/rspa.1953.0064 doi: 10.1098/rspa.1953.0064

Fitzgerald, W. F., & Lamborg, C. H. (2014). 11.4 - Geochemistry of Mercury in the Environment. In H. D. Holland & K. K. B. T. T. o. G. S. E. Turekian (Eds.), *Treatise on geochemistry: Second edition* (pp. 91–129). Oxford: Elsevier. Retrieved from http://www.sciencedirect.com/science/article/pii/B9780080959757009049 doi: 10.1016/B978-0-08-095975-7.00904-9

Font, E., Adatte, T., Sial, A. N., de Lacerda, L. D., Keller, G., & Punekar, J. (2016). Mercury anomaly, Deccan volcanism, and the end-Cretaceous mass extinction. *Geology*, *44*(2), 171–174. Retrieved from http://geology.gsapubs.org/lookup/doi/10.1130/G37451.1 doi: 10.1130/G37451.1

Friedli, H. R., Arellano, A. F., Cinnirella, S., & Pirrone, N. (2009, 5). Initial Estimates of Mercury Emissions to the Atmosphere from Global Biomass Burning. *Environmental Science &*

Technology, *43*(10), 3507–3513. Retrieved from https://doi.org/10.1021/es802703g doi: 10.1021/es802703g

Friedlingstein, P., Jones, M. W., O'Sullivan, M., Andrew, R. M., Hauck, J., Peters, G. P., ... Zaehle, S. (2019, 12). Global Carbon Budget 2019. *Earth System. Sci. Data*, *11*(4), 1783–1838. Retrieved from https://www.earth-syst-sci-data.net/11/1783/2019/ https://www.earth-syst-sci-data.net/11/1783/2019/essd-11-1783-2019.pdf doi: 10.5194/essd-11-1783-2019

Gao, Y., Ibarra, D. E., Wang, C., Caves, J. K., Chamberlain, C. P., Graham, S. A., & Wu, H. (2015, 4). Mid-latitude terrestrial climate of East Asia linked to global climate in the Late Cretaceous. *Geology*, *43*(4), 287–290. Retrieved from https://doi.org/10.1130/G36427.1 doi: 10.1130/G36427.1

Geological Survey of India. (2000a). *District Resource Map, East Godavari District, Andhra Pradesh.*

Geological Survey of India. (2000b). *District Resource Map, West Godavari District, Andhra Pradesh.*

Ghosh, P., Sayeed, M. R. G., Islam, R., & Hundekari, S. M. (2006). Inter-basaltic clay (bole bed) horizons from Deccan traps of India: Implications for palaeo-weathering and palaeo-climate during Deccan volcanism. *Palaeogeography, Palaeoclimatology, Palaeoecology*, *242*(1), 90–109. Retrieved from http://www.sciencedirect.com/science/article/pii/S0031018206003233 doi: https://doi.org/10.1016/j.palaeo.2006.05.018

Gibson, B. D., Ptacek, C. J., Blowes, D. W., & Daugherty, S. D. (2015). Sediment resuspension under variable geochemical conditions and implications for contaminant release. *Journal of Soils and Sediments*, *15*(7), 1644–1656. Retrieved from https://doi.org/10.1007/s11368-015-1106-6 doi: 10.1007/s11368-015-1106-6

Gilleaudeau, G. J., Voegelin, A. R., Thibault, N., Moreau, J., Ullmann, C. V., Klaebe, R. M., ... Frei, R. (2018). Stable isotope records across the Cretaceous-Paleogene transition, Stevns Klint, Denmark: New insights from the chromium isotope system. *Geochimica et Cosmochimica Acta*, *235*, 305–332. Retrieved from http://www.sciencedirect.com/science/article/pii/S0016703718302461 doi: 10.1016/j.gca.2018.04.028

Gilmour, I., Gilmour, M., Jolley, D. W., Kelley, S., Kemp, D., Daly, R., & Watson, J. (2013, 7). A high-resolution nonmarine record of an early Danian hyperthermal event, Boltysh crater, Ukraine. *Geology*, *41*(7), 783–786. Retrieved from https://doi.org/10.1130/G34292.1 doi: 10.1130/G34292.1

Gilmour, I., Jolley, D. W., Kemp, D., Kelley, S., Gilmour, M., Daly, R., & Widdowson, M. (2014, 9). The early Danian hyperthermal event at Boltysh (Ukraine): Relation to Cretaceous-Paleogene boundary events. In G. Keller & A. C. Kerr (Eds.), *Volcanism, impacts, and mass extinctions: Causes and effects* (Vol. 505, p. 0). Geological Society of America. Retrieved from https://doi.org/10.1130/2014.2505(06) doi: 10.1130/2014.2505(06)

Glaze, L. S., Self, S., Schmidt, A., & Hunter, S. J. (2017). Assessing eruption column height in ancient flood basalt eruptions.

Earth and Planetary Science Letters, *457*, 263–270. Retrieved from http://www.sciencedirect.com/science/article/pii/S0012821X14004981 doi: 10.1016/j.epsl.2014.07.043

Goulet, R. R., Holmes, J., Page, B., Poissant, L., Siciliano, S. D., Lean, D. R. S., ... Tessier, A. (2007). Mercury transformations and fluxes in sediments of a riverine wetland. *Geochimica et Cosmochimica Acta*, *71*(14), 3393–3406. Retrieved from http://www.sciencedirect.com/science/article/pii/S0016703707002645 doi: 10.1016/j.gca.2007.04.032

Graham, H. V., Herrera, F., Jaramillo, C., Wing, S. L., & Freeman, K. H. (2019, 9). Canopy structure in Late Cretaceous and Paleocene forests as reconstructed from carbon isotope analyses of fossil leaves. *Geology*, *47*(10), 977–981. Retrieved from https://doi.org/10.1130/G46152.1 doi: 10.1130/G46152.1

Grandpre, R., Schauer, A., Samek, K., Veeger, A., Ward, P., & Fastovsky, D. (2013). Testing the terrestrial δ13C Cretaceous–Paleogene (K–Pg) chemostratigraphic marker. *Palaeogeography, Palaeoclimatology, Palaeoecology*, *381-382*, 67–75. Retrieved from http://www.sciencedirect.com/science/article/pii/S0031018213001892 doi: 10.1016/j.palaeo.2013.04.015

Grasby, S. E., Sanei, H., Beauchamp, B., & Chen, Z. (2013). Mercury deposition through the Permo–Triassic Biotic Crisis. *Chemical Geology*, *351*, 209–216. Retrieved from http://www.sciencedirect.com/science/article/pii/S0009254113002283 doi: 10.1016/j.chemgeo.2013.05.022

Hao, H., Ferguson, D. K., Feng, G.-P., Ablaev, A., Wang, Y.-F., & Li, C.-S. (2010). Early Paleocene vegetation and climate in Jiayin, NE China. *Climatic Change*, *99*(3), 547–566. Retrieved from https://doi.org/10.1007/s10584-009-9728-6 doi: 10.1007/s10584-009-9728-6

Hare, V. J., Loftus, E., Jeffrey, A., & Ramsey, C. B. (2018). Atmospheric CO2 effect on stable carbon isotope composition of terrestrial fossil archives. *Nature Communications*, *9*(1), 252. Retrieved from https://doi.org/10.1038/s41467-017-02691-x doi: 10.1038/s41467-017-02691-x

Hein, C. J., Usman, M., Eglinton, T. I., Haghipour, N., & Galy, V. V. (2020). Millennial-scale hydroclimate control of tropical soil carbon storage. *Nature*, *581*(7806), 63–66. Retrieved from https://doi.org/10.1038/s41586-020-2233-9 doi: 10.1038/s41586-020-2233-9

Henehan, M. J., Ridgwell, A., Thomas, E., Zhang, S., Alegret, L., Schmidt, D. N., ... Hull, P. M. (2019, 11). Rapid ocean acidification and protracted Earth system recovery followed the end-Cretaceous Chicxulub impact. *Proceedings of the National Academy of Sciences*, *116*(45), 22500 LP - 22504. Retrieved from http://www.pnas.org/content/116/45/22500.abstract doi: 10.1073/pnas.1905989116

Hildreth, W., & Wilson, C. J. N. (2007, 5). Compositional Zoning of the Bishop Tuff. *Journal of Petrology*, *48*(5), 951–999. Retrieved from http://dx.doi.org/10.1093/petrology/egm007 doi: 10.1093/petrology/egm007

Huang, C., Retallack, G. J., Wang, C., & Huang, Q. (2013). Paleoatmospheric pCO2 fluctuations across the Cretaceous–Tertiary boundary recorded from paleosol carbonates in NE

China. *Palaeogeography, Palaeoclimatology, Palaeoecology*, *385*, 95–105. Retrieved from http://www.sciencedirect.com/science/article/pii/S0031018213000096 doi: 10.1016/j.palaeo.2013.01.005

Hull, P. M., Bornemann, A., Penman, D. E., Henehan, M. J., Norris, R. D., Wilson, P. A., ... Zachos, J. C. (2020, 1). On impact and volcanism across the Cretaceous-Paleogene boundary. *Science*, *367*(6475), 266 LP - 272. Retrieved from http://science.sciencemag.org/content/367/6475/266.abstract doi: 10.1126/science.aay5055

Hull, P. M., & Norris, R. D. (2011, 9). Diverse patterns of ocean export productivity change across the Cretaceous-Paleogene boundary: New insights from biogenic barium. *Paleoceanography*, *26*(3). Retrieved from https://doi.org/10.1029/2010PA002082 doi: 10.1029/2010PA002082

Ickert, R. B., Mulcahy, S. R., Sprain, C. J., Banaszak, J. F., & Renne, P. R. (2015). Chemical and Pb isotope composition of phenocrysts from bentonites constrains the chronostratigraphy around the Cretaceous-Paleogene boundary in the Hell Creek region, Montana. *Geochemistry, Geophysics, Geosystems*, *16*(8), 2743–2761. doi: 10.1002/2015GC005898

Izett, G. A. (1990, 1). The Cretaceous/Tertiary boundary interval, Raton Basin, Colorado and New Mexico, and its content of shock-metamorphosed minerals; Evidence relevant to the K/T boundary impact-extinction theory. In G. A. Izett (Ed.), *The cretaceous/tertiary boundary interval, raton basin, colorado and new mexico, and its content of shock-metamorphosed minerals; evidence relevant to the k/t boundary impact-extinction theory* (Vol. 249, p. 0). Geological Society of America. Retrieved from https://doi.org/10.1130/SPE249-p1 doi: 10.1130/SPE249-p1

Jay, A. E. (2005). *Volcanic architecture of the Deccan Traps, western Maharashtra, India: an integrated chemostratigraphic and paleomagnetic study* (Unpublished doctoral dissertation). The Open University.

Jay, A. E., & Widdowson, M. (2008, 1). Stratigraphy, structure and volcanology of the SE Deccan continental flood basalt province: implications for eruptive extent and volumes. *Journal of the Geological Society*, *165*(1), 177–188. Retrieved from https://doi.org/10.1144/0016-76492006-062 doi: 10.1144/0016-76492006-062

Jerrett, R. M., Price, G. D., Grimes, S. T., & Dawson, A. T. (2015, 11). A paleoclimatic and paleoatmospheric record from peatlands accumulating during the Cretaceous-Paleogene boundary event, Western Interior Basin, Canada. *GSA Bulletin*, *127*(11-12), 1564–1582. Retrieved from https://doi.org/10.1130/B31166.1 doi: 10.1130/B31166.1

Johnson, K. R. (2002, 9). Megaflora of the Hell Creek and lower Fort Union Formations in the western Dakotas: Vegetational response to climate change, the Cretaceous-Tertiary boundary event, and rapid marine transgression. In J. H. Hartman, K. R. Johnson, & D. J. Nichols (Eds.), *The hell creek formation and the cretaceous-tertiary boundary in the northern great plains: An integrated continental record of the end of the cretaceous* (Vol. 361, p. 0). Geological Society of America. Retrieved from https://doi.org/10.1130/0-8137-2361-2.329 doi: 10.1130/0-8137-2361-2.329

Jolley, D. W., Daly, R. J., Ebinghaus, A., Kemp, D. B., Gilmour, I., Mac Niocaill, C., & Kelley,

S. P. (2017, 6). Centennial to decadal vegetation community changes linked to orbital and solar forcing during the Dan-C2 hyperthermal event. *Journal of the Geological Society*, *174*(6), 1019–1030. Retrieved from https://doi.org/10.1144/jgs2017-022 doi: 10.1144/jgs2017-022

Jolley, D. W., Gilmour, I., Gurov, E., Kelley, S., & Watson, J. (2010, 9). Two large meteorite impacts at the Cretaceous-Paleogene boundary. *Geology*, *38*(9), 835–838. Retrieved from https://doi.org/10.1130/G31034.1 doi: 10.1130/G31034.1

Kale, V. S., Dole, G., Shandilya, P., & Pande, K. (2020, 6). Stratigraphy and correlations in Deccan Volcanic Province, India: Quo vadis? *Geological Society of America Bulletin*, *132*(3-4), 588–607. Retrieved from https://doi.org/10.1130/B35018.1 doi: 10.1130/B35018.1

Keeling, R. F., Graven, H. D., Welp, L. R., Resplandy, L., Bi, J., Piper, S. C., . . . Meijer, H. A. J. (2017, 9). Atmospheric evidence for a global secular increase in carbon isotopic discrimination of land photosynthesis. *Proceedings of the National Academy of Sciences*, *114*(39), 10361 - 10366. Retrieved from http://www.pnas.org/content/114/39/10361.abstract doi: 10.1073/pnas.1619240114

Keller, G., Adatte, T., Bhowmick, P. K., Upadhyay, H., Dave, A., Reddy, A. N., & Jaiprakash, B. C. (2012). Nature and timing of extinctions in Cretaceous-Tertiary planktic foraminifera preserved in Deccan intertrappean sediments of the Krishna–Godavari Basin, India. *Earth and Planetary Science Letters*, *341-344*, 211–221. Retrieved from http://www.sciencedirect.com/science/article/pii/S0012821X12003056 doi: 10.1016/j.epsl.2012.06.021

Keller, G., Adatte, T., Gardin, S., Bartolini, A., & Bajpai, S. (2008). Main Deccan volcanism phase ends near the K-T boundary: Evidence from the Krishna-Godavari Basin, SE India. *Earth and Planetary Science Letters*, *268*(3-4), 293–311. doi: 10.1016/j.epsl.2008.01.015

Keller, G., Bhowmick, P. K., Upadhyay, H., Dave, A., Reddy, A. N., Jaiprakash, B. C., & Adatte, T. (2011). Deccan volcanism linked to the Cretaceous-Tertiary boundary mass extinction: New evidence from ONGC wells in the Krishna-Godavari Basin. *Journal of the Geological Society of India*, *78*(5), 399–428. Retrieved from https://doi.org/10.1007/s12594-011-0107-3 doi: 10.1007/s12594-011-0107-3

Keller, G., Li, L., & MacLeod, N. (1996). The Cretaceous/Tertiary boundary stratotype section at El Kef, Tunisia: how catastrophic was the mass extinction? *Palaeogeography, Palaeoclimatology, Palaeoecology*, *119*(3), 221–254. Retrieved from http://www.sciencedirect.com/science/article/pii/0031018295000097 doi: 10.1016/0031-0182(95)00009-7

Keller, G., Mateo, P., Punekar, J., Khozyem, H., Gertsch, B., Spangenberg, J., . . . Adatte, T. (2018). Environmental changes during the Cretaceous-Paleogene mass extinction and Paleocene-Eocene Thermal Maximum: Implications for the Anthropocene. *Gondwana Research*, *56*, 69–89. doi: 10.1016/j.gr.2017.12.002

Kelley, S. P., & Gurov, E. (2002, 8). Boltysh, another end-Cretaceous impact. *Meteoritics & Planetary Science*, *37*(8), 1031–1043. Retrieved from https://doi.org/10.1111/j.1945-5100.2002.tb00875.x doi: 10.1111/j.1945-5100.2002.tb00875.x

Kirschvink, J. L. (1980, 9). The least-squares line and plane and the analysis of palaeomagnetic data. *Geophysical Journal International*, *62*(3), 699–718. Retrieved from https://doi.org/10.1111/j.1365-246X.1980.tb02601.x doi: 10.1111/j.1365-246X.1980.tb02601.x

Kita, I., Yamashita, T., Chiyonobu, S., Hasegawa, H., Sato, T., & Kuwahara, Y. (2016, 5). Mercury content in Atlantic sediments as a new indicator of the enlargement and reduction of Northern Hemisphere ice sheets. *Journal of Quaternary Science*, *31*(3), 167–177. Retrieved from https://doi.org/10.1002/jqs.2854 doi: 10.1002/jqs.2854

Knight, K. B., Renne, P. R., Halkett, A., & White, N. (2003). 40Ar/39Ar dating of the Rajahmundry Traps, Eastern India and their relationship to the Deccan Traps. *Earth and Planetary Science Letters*, *208*(1-2), 85–99. doi: 10.1016/S0012-821X(02)01154-8

Kohn, M. J. (2010, 11). Carbon isotope compositions of terrestrial C3 plants as indicators of (paleo)ecology and (paleo)climate. *Proceedings of the National Academy of Sciences*, *107*(46), 19691 LP - 19695. Retrieved from http://www.pnas.org/content/107/46/19691.abstract doi: 10.1073/pnas.1004933107

Komar, N., & Zeebe, R. E. (2017). Redox-controlled carbon and phosphorus burial: A mechanism for enhanced organic carbon sequestration during the PETM. *Earth and Planetary Science Letters*, *479*, 71–82. Retrieved from http://www.sciencedirect.com/science/article/pii/S0012821X17305071 doi: 10.1016/j.epsl.2017.09.011

Krivolutskaya, N. A., & Kedrovskaya, T. B. (2020). Structure and Composition of the Nadayansky Lava Flow: an Example of the Homogeneity of Lava Flows of the Siberian Trap Province. *Geochemistry International*, *58*(4), 363–376. Retrieved from https://doi.org/10.1134/S0016702920040047 doi: 10.1134/S0016702920040047

Lakshminarayana, G., Manikyamba, C., Khanna, T. C., Kanakdande, P. P., & Raju, K. (2010). New observations on Rajahmundry Traps of the Krishna-Godavari Basin. *Journal of the Geological Society of India*, *75*(6), 807–819. doi: 10.1007/s12594-010-0071-3

Lamborg, C. H., Hammerschmidt, C. R., Bowman, K. L., Swarr, G. J., Munson, K. M., Ohnemus, D. C., ... Saito, M. A. (2014). A global ocean inventory of anthropogenic mercury based on water column measurements. *Nature*, *512*, 65. Retrieved from http://dx.doi.org/10.1038/nature13563 http://10.0.4.14/nature13563 https://www.nature.com/articles/nature13563 doi: 10.1038/nature13563

LeCain, R., Clyde, W. C., Wilson, G. P., & Riedel, J. (2014). Magnetostratigraphy of the Hell Creek and lower Fort Union Formations in northeastern Montana. *2. Through the End of the Cretaceous in the Type Locality of the Hell Creek Formation in Montana and Adjacent Areas - 1. Geological Society of America Special Papers*, *503*(04), 137–147. Retrieved from http://specialpapers.gsapubs.org/content/503/137.abstract doi: 10.1130/2014.2503(04)

Lee, J.-Y., Marti, K., Severinghaus, J. P., Kawamura, K., Yoo, H.-S., Lee, J. B., & Kim, J. S. (2006). A redetermination of the isotopic abundances of atmospheric Ar. *Geochimica et Cosmochimica Acta*, *70*(17), 4507–4512. Retrieved from

http://www.sciencedirect.com/science/article/pii/S0016703706018679 doi: 10.1016/j.gca.2006.06.1563

Lehman, T. M., Wick, S. L., Beatty, H. L., Straight, W. H., & Wagner, J. R. (2018, 8). Stratigraphy and depositional history of the Tornillo Group (Upper Cretaceous–Eocene) of West Texas. *Geosphere*, *14*(5), 2206–2244. Retrieved from https://doi.org/10.1130/GES01641.1 doi: 10.1130/GES01641.1

Lerman, A., & Clauer, N. (2014). 9.16 - Stable Isotopes in the Sedimentary Record. In H. D. Holland & K. K. B. T. T. o. G. S. E. Turekian (Eds.), (pp. 437–481). Oxford: Elsevier. Retrieved from http://www.sciencedirect.com/science/article/pii/B9780080959757007166 doi: 10.1016/B978-0-08-095975-7.00716-6

Lightfoot, P. C., Hawkesworth, C. J., Devey, C. W., Rogers, N. W., & Calsteren, P. W. C. V. A. N. (1990, 10). Source and Differentiation of Deccan Trap Lavas: Implications of Geochemical and Mineral Chemical Variations. *Journal of Petrology*, *31*(5), 1165–1200. Retrieved from https://doi.org/10.1093/petrology/31.5.1165 doi: 10.1093/petrology/31.5.1165

Lugato, E., Smith, P., Borrelli, P., Panagos, P., Ballabio, C., Orgiazzi, A., ... Jones, A. (2018, 11). Soil erosion is unlikely to drive a future carbon sink in Europe. *Science Advances*, *4*(11), eaau3523. Retrieved from http://advances.sciencemag.org/content/4/11/eaau3523.abstract doi: 10.1126/sciadv.aau3523

Lyson, T. R., Miller, I. M., Bercovici, A. D., Weissenburger, K., Fuentes, A. J., Clyde, W. C., ... Chester, S. G. B. (2019, 11). Exceptional continental record of biotic recovery after the Cretaceous–Paleogene mass extinction. *Science*, *366*(6468), 977 LP - 983. Retrieved from http://science.sciencemag.org/content/366/6468/977.abstract doi: 10.1126/science.aay2268

MacLeod, K. G., Quinton, P. C., Sepúlveda, J., & Negra, M. H. (2018, 5). Postimpact earliest Paleogene warming shown by fish debris oxygen isotopes (El Kef, Tunisia). *Science*. Retrieved from http://science.sciencemag.org/content/early/2018/05/23/science.aap8525 doi: 10.1126/science.aap8525

Mahoney, J. J. (1988). Deccan Traps. In J. D. Macdougall (Ed.), *Continental flood basalts* (pp. 151–194). Dordrecht: Springer Netherlands. doi: 10.1007/978-94-015-7805-9_5

Malarkodi, N., Keller, G., Fayazudeen, P. J., & Mallikarjuna, U. B. (2010). Foraminifera from the early Danian intertrappean beds in Rajahmundry quarries, Andhra Pradesh. *Journal of the Geological Society of India*, *75*(6), 851–863. Retrieved from https://doi.org/10.1007/s12594-010-0066-0 doi: 10.1007/s12594-010-0066-0

Mallick, S., Bardhan, S., Das, S. S., Paul, S., & Goswami, P. (2014). Naticid drilling predation on gastropod assemblages across the K–T boundary in Rajahmundry, India: New evidence for escalation hypothesis. *Palaeogeography, Palaeoclimatology, Palaeoecology*, *411*, 216–228. Retrieved from http://www.sciencedirect.com/science/article/pii/S0031018214003460 doi: https://doi.org/10.1016/j.palaeo.2014.07.001

Manikyamba, C., Ganguly, S., Santosh, M., Saha, A., & Lakshminarayana, G. (2015). Geo-

chemistry and petrogenesis of Rajahmundry trap basalts of Krishna-Godavari Basin, India. *Geoscience Frontiers*, *6*(3), 437–451. doi: 10.1016/j.gsf.2014.05.003

Mathieu, J. A., Hatté, C., Balesdent, J., & Parent, (2015, 6). Deep soil carbon dynamics are driven more by soil type than by climate: a worldwide meta-analysis of radiocarbon profiles. *Global Change Biology*, *21*(11), 4278–4292. Retrieved from https://doi.org/10.1111/gcb.13012 doi: 10.1111/gcb.13012

Maufrangeas, A., Leleu, S., Loisy, C., Roperch, P., Jolley, D., Vinciguerra, C., & Nguyen-Thuyet, O. (2020, 5). Stratigraphy of the Paleocene continental sedimentary succession of the northern Pyrenean basin (Corbières, southern France) using δ13Corg isotopes. *Journal of the Geological Society*, 2019–084. Retrieved from http://jgs.lyellcollection.org/content/early/2020/05/07/jgs2019-08 doi: 10.1144/jgs2019-084

McDonough, W. F., & Sun, S.-s. (1995). The composition of the Earth. *Chemical Geology*, *120*(3), 223–253. Retrieved from http://www.sciencedirect.com/science/article/pii/0009254194001404 doi: https://doi.org/10.1016/0009-2541(94)00140-4

McFadden, P. L., & McElhinny, M. W. (1990, 12). Classification of the reversal test in palaeomagnetism. *Geophysical Journal International*, *103*(3), 725–729. Retrieved from https://doi.org/10.1111/j.1365-246X.1990.tb05683.x doi: 10.1111/j.1365-246X.1990.tb05683.x

Meehl, G. A., Senior, C. A., Eyring, V., Flato, G., Lamarque, J.-F., Stouffer, R. J., . . . Schlund, M. (2020, 6). Context for interpreting equilibrium climate sensitivity and transient climate response from the CMIP6 Earth system models. *Science Advances*, *6*(26), eaba1981. Retrieved from http://advances.sciencemag.org/content/6/26/eaba1981.abstract doi: 10.1126/sciadv.aba1981

Milligan, J. N., Royer, D. L., Franks, P. J., Upchurch, G. R., & McKee, M. L. (2019, 3). No Evidence for a Large Atmospheric CO2 Spike Across the Cretaceous-Paleogene Boundary. *Geophysical Research Letters*, *46*(6), 3462–3472. Retrieved from https://doi.org/10.1029/2018GL081215 doi: 10.1029/2018GL081215

Mittal, T., & Richards, M. A. (2019). Volatile Degassing From Magma Chambers as a Control on Volcanic Eruptions. *Journal of Geophysical Research: Solid Earth*, *124*(8), 7869–7901. Retrieved from 10.1029/2018JB016983 doi: 10.1029/2018JB016983

Mooney, H. A., Bullock, S. H., & Ehleringer, J. R. (1989, 6). Carbon Isotope Ratios of Plants of a Tropical Dry Forest in Mexico. *Functional Ecology*, *3*(2), 137–142. Retrieved from http://www.jstor.org/stable/2389294 doi: 10.2307/2389294

Mukherjee, S., Bardhan, S., Mallick, S., Paul, S., & Das, S. S. (2013, 10). Intense Naticid drilling predation on Turritelline gastropods from below the K-T boundary at Rajahmundry, India. *PALAIOS*, *28*(10), 683–696. Retrieved from https://doi.org/10.2110/palo.2013.p13-007r doi: 10.2110/palo.2013.p13-007r

Noorbergen, L. J., Abels, H. A., Hilgen, F. J., Robson, B. E., Jong, E., Dekkers, M. J., . . . Kuiper, K. F. (2017, 7). Conceptual models for short-eccentricity-scale climate control on peat formation in a lower Palaeocene fluvial system, north-eastern Montana (USA).

Sedimentology, *65*(3), 775–808. Retrieved from https://doi.org/10.1111/sed.12405 doi: 10.1111/sed.12405

Nordt, L., Atchley, S., & Dworkin, S. (2003). Terrestrial evidence for two greenhouse events in the latest Cretaceous. *GSA today*, *13*(12), 4–9.

O'Brien, C. L., Robinson, S. A., Pancost, R. D., Sinninghe Damsté, J. S., Schouten, S., Lunt, D. J., ... Wrobel, N. E. (2017). Cretaceous sea-surface temperature evolution: Constraints from TEX86 and planktonic foraminiferal oxygen isotopes. *Earth-Science Reviews*, *172*, 224–247. Retrieved from http://www.sciencedirect.com/science/article/pii/S0012825217303859 doi: https://doi.org/10.1016/j.earscirev.2017.07.012

Ogg, J. G. (2012). Chapter 5 - Geomagnetic Polarity Time Scale. In F. M. Gradstein, J. G. Ogg, M. D. Schmitz, & G. M. B. T. T. G. T. S. Ogg (Eds.), *The geologic time scale 2012* (pp. 85–113). Boston: Elsevier. Retrieved from http://www.sciencedirect.com/science/article/pii/B9780444594259000056 doi: 10.1016/B978-0-444-59425-9.00005-6

Olsson, R. K., Berggren, W. A., Hemleben, C.-i., & Huber, B. T. (1999). Atlas of Paleocene planktonic foraminifera. *Smithsonian contributions to Paleobiology*.

Olund, S. D., DeWild, J. F., Olson, M. L., & Tate, M. T. (2004). *Methods for the preparation and analysis of solids and suspended solids for total mercury* (- ed.; Tech. Rep.). Retrieved from http://pubs.er.usgs.gov/publication/tm5A8 doi: 10.3133/tm5A8

Papale, P. (2018). Global time-size distribution of volcanic eruptions on Earth. *Scientific Reports*, *8*(1), 6838. Retrieved from https://doi.org/10.1038/s41598-018-25286-y doi: 10.1038/s41598-018-25286-y

Peppe, D. J., Evans, D. A. D., & Smirnov, A. V. (2009, 1). Magnetostratigraphy of the Ludlow Member of the Fort Union Formation (Lower Paleocene) in the Williston Basin, North Dakota. *GSA Bulletin*, *121*(1-2), 65–79. Retrieved from https://doi.org/10.1130/B26353.1 doi: 10.1130/B26353.1

Percival, L. M. E., Jenkyns, H. C., Mather, T. A., Dickson, A. J., Batenburg, S. J., Ruhl, M., ... Woelders, L. (2018, 10). Does large igneous province volcanism always perturb the mercury cycle? Comparing the records of Oceanic Anoxic Event 2 and the end-Cretaceous to other Mesozoic events. *American Journal of Science*, *318*(8), 799–860. Retrieved from http://www.ajsonline.org/content/318/8/799.abstract doi: 10.2475/08.2018.01

Percival, L. M. E., Witt, M. L. I., Mather, T. A., Hermoso, M., Jenkyns, H. C., Hesselbo, S. P., ... Ruhl, M. (2015). Globally enhanced mercury deposition during the end-Pliensbachian extinction and Toarcian OAE: A link to the Karoo–Ferrar Large Igneous Province. *Earth and Planetary Science Letters*, *428*, 267–280. Retrieved from http://www.sciencedirect.com/science/article/pii/S0012821X15004276 doi: 10.1016/j.epsl.2015.06.064

Potter, C. S., Randerson, J. T., Field, C. B., Matson, P. A., Vitousek, P. M., Mooney, H. A., & Klooster, S. A. (1993, 9). Terrestrial ecosystem production: A process model based on global satellite and surface data. *Global Biogeochemical Cycles*, *7*(4), 811–841. Retrieved

from https://doi.org/10.1029/93GB02725 doi: 10.1029/93GB02725

Raup, D. M., & Sepkoski, J. J. (1982, 3). Mass Extinctions in the Marine Fossil Record. *Science*, *215*(4539), 1501 LP - 1503. Retrieved from http://science.sciencemag.org/content/215/4539/1501.abstract doi: 10.1126/science.215.4539.1501

Raynolds, R. G. H., Johnson, K. R., Arnold, L. R., Farnham, T. M., Fleming, R. F., Hicks, J. F., ... Wilson, M. D. (2001). *The Kiowa Core, a continuous drill core through the Denver Basin bedrock aquifers at Kiowa, Elbert County, Colorado* (Tech. Rep.). doi: 10.3133/ofr01185

Renne, P. R., Balco, G., Ludwig, K. R., Mundil, R., & Min, K. (2011). Response to the comment by WH Schwarz et al. on "Joint determination of 40K decay constants and 40Ar/40K for the Fish Canyon sanidine standard, and improved accuracy for 40Ar/39Ar geochronology" by PR Renne et al.(2010). *Geochimica et Cosmochimica Acta*, *75*(17), 5097–5100. doi: 10.1016/j.gca.2011.06.021

Renne, P. R., Cassata, W. S., & Morgan, L. E. (2009). The isotopic composition of atmospheric argon and 40ar/39ar geochronology: Time for a change? *Quaternary Geochronology*, *4*(4), 288–298.

Renne, P. R., Deino, A. L., Hilgen, F., Kuiper, K. F., Mark, D. F., Mitchell, W. S., ... Smit, J. (2013). Time scales of critical events around the Cretaceous-Paleogene boundary. *Science (New York, N.Y.)*, *339*(6120), 684–7. Retrieved from http://www.ncbi.nlm.nih.gov/pubmed/23393261 doi: 10.1126/science.1230492

Renne, P. R., Mundil, R., Balco, G., Min, K., & Ludwig, K. R. (2010). Joint determination of 40K decay constants and 40Ar/40K for the Fish Canyon sanidine standard, and improved accuracy for 40Ar/39Ar geochronology. *Geochimica et Cosmochimica Acta*, *74*(18), 5349–5367. Retrieved from http://www.sciencedirect.com/science/article/pii/S0016703710003571 doi: 10.1016/j.gca.2010.06.017

Renne, P. R., & Norman, E. B. (2001, 2). Determination of the half-life of 37Ar by mass spectrometry. *Physical Review C*, *63*(4), 47302. Retrieved from https://link.aps.org/doi/10.1103/PhysRevC.63.047302 doi: 10.1103/PhysRevC.63.047302

Reynolds, P., Holford, S., Schofield, N., & Ross, A. (2017, 11). Three-Dimensional Seismic Imaging of Ancient Submarine Lava Flows: An Example From the Southern Australian Margin. *Geochemistry, Geophysics, Geosystems*, *18*(11), 3840–3853. Retrieved from https://doi.org/10.1002/2017GC007178 doi: 10.1002/2017GC007178

Richards, M. A., Alvarez, W., Self, S., Karlstrom, L., Renne, P. R., Manga, M., ... Gibson, S. A. (2015). Triggering of the largest Deccan eruptions by the Chicxulub impact. *Bulletin of the Geological Society of America*, *127*(11-12), 1507–1520. doi: 10.1130/B31167.1

Romanek, C. S., Grossman, E. L., & Morse, J. W. (1992). Carbon isotopic fractionation in synthetic aragonite and calcite: Effects of temperature and precipitation rate. *Geochimica et Cosmochimica Acta*, *56*(1), 419–430. Retrieved from http://www.sciencedirect.com/science/article/pii/0016703792901426 doi: 10.1016/0016-7037(92)90142-6

Royer, D. L. (2016, 6). Climate Sensitivity in the Geologic Past. *Annual Review of Earth and Planetary Sciences*, *44*(1), 277–293. Retrieved from https://doi.org/10.1146/annurev-earth-100815-024150 doi: 10.1146/annurev-earth-100815-024150

Sahu, H. S., Raab, M. J., Kohn, B. P., Gleadow, A. J. W., & Bal, K. D. (2013). Thermal history of the Krishna–Godavari basin, India: Constraints from apatite fission track thermochronology and organic maturity data. *Journal of Asian Earth Sciences*, *73*, 1–20. Retrieved from http://www.sciencedirect.com/science/article/pii/S1367912013002381 doi: 10.1016/j.jseaes.2013.04.028

Sanei, H., Grasby, S. E., & Beauchamp, B. (2012). Latest Permian mercury anomalies. *Geology*, *40*(1), 63–66. Retrieved from http://geology.gsapubs.org/cgi/doi/10.1130/G32596.1 doi: 10.1130/G32596.1

Schlanser, K., Diefendorf, A. F., Greenwood, D. R., Mueller, K. E., West, C. K., Lowe, A. J., ... Peppe, D. J. (2020). On geologic timescales, plant carbon isotope fractionation responds to precipitation similarly to modern plants and has a small negative correlation with pCO2. *Geochimica et Cosmochimica Acta*, *270*, 264–281. Retrieved from http://www.sciencedirect.com/science/article/pii/S0016703719307318 doi: 10.1016/j.gca.2019.11.023

Schmidt, A., Skeffington, R. A., Thordarson, T., Self, S., Forster, P. M., Rap, A., ... Carslaw, K. S. (2016). Selective environmental stress from sulphur emitted by continental flood basalt eruptions. *Nature Geoscience*, *9*(1), 77–82. Retrieved from http://www.nature.com/doifinder/10.1038/ngeo2588 doi: 10.1038/ngeo2588

Schöbel, S., de Wall, H., Ganerød, M., Pandit, M. K., & Rolf, C. (2014). Magnetostratigraphy and ^{40}Ar–^{39}Ar geochronology of the Malwa Plateau region (Northern Deccan Traps), central western India: Significance and correlation with the main Deccan Large Igneous Province sequences. *Journal of Asian Earth Sciences*, *89*, 28–45. Retrieved from http://www.sciencedirect.com/science/article/pii/S1367912014001540 doi: 10.1016/j.jseaes.2014.03.022

Schoene, B., Eddy, M. P., Samperton, K. M., Keller, C. B., Keller, G., Adatte, T., & Khadri, S. F. R. (2019, 2). U-Pb constraints on pulsed eruption of the Deccan Traps across the end-Cretaceous mass extinction. *Science*, *363*(6429), 862 LP - 866. Retrieved from http://science.sciencemag.org/content/363/6429/862.abstract doi: 10.1126/science.aau2422

Schubert, B. A., & Jahren, A. H. (2012). The effect of atmospheric CO2 concentration on carbon isotope fractionation in C3 land plants. *Geochimica et Cosmochimica Acta*, *96*, 29–43. Retrieved from http://www.sciencedirect.com/science/article/pii/S0016703712004504 doi: https://doi.org/10.1016/j.gca.2012.08.003

Schubert, B. A., & Jahren, A. H. (2013). Reconciliation of marine and terrestrial carbon isotope excursions based on changing atmospheric CO2 levels. *Nature Communications*, *4*(1), 1653. Retrieved from https://doi.org/10.1038/ncomms2659 doi: 10.1038/ncomms2659

Schulte, P., Alegret, L., Arenillas, I., Arz, J. A., Barton, P. J., Bown, P. R., ... Willumsen, P. S. (2010). The Chicxulub Asteroid Impact and Mass Extinction at the Cretaceous-Paleogene Boundary. *Science*, *327*(5970), 1214–1218. Retrieved from http://www.sciencemag.org/cgi/doi/10.1126/science.1177265 doi: 10.1126/science.1177265

Self, S., Blake, S., Sharma, K., Widdowson, M., & Sephton, S. (2008). Sulfur and chlorine in Late Cretaceous Deccan magmas and eruptive gas release. *Science*, *319*(March), 1654–1657. doi: 10.1126/science.1152830

Self, S., Jay, A. E., Widdowson, M., & Keszthelyi, L. P. (2008). Correlation of the Deccan and Rajahmundry Trap lavas: Are these the longest and largest lava flows on Earth? *Journal of Volcanology and Geothermal Research*, *172*(1-2), 3–19. doi: 10.1016/j.jvolgeores.2006.11.012

Self, S., Keszthelyi, L., & Thordarson, T. (1998, 5). The Importance of Pahoehoe. *Annual Review of Earth and Planetary Sciences*, *26*(1), 81–110. Retrieved from https://doi.org/10.1146/annurev.earth.26.1.81 doi: 10.1146/annurev.earth.26.1.81

Self, S., Schmidt, A., & Mather, T. A. (2014). Emplacement characteristics, time scales, and volcanic gas release rates of continental flood basalt eruptions on Earth. *Geological Society of America Special Papers*, *505*. doi: 10.1130/2014.2505(16)

Self, S., Widdowson, M., Thordarson, T., & Jay, A. E. (2006). Volatile fluxes during flood basalt eruptions and potential effects on the global environment: A Deccan perspective. *Earth and Planetary Science Letters*, *248*(1-2), 517–531. doi: 10.1016/j.epsl.2006.05.041

Sen, B., & Sabale, A. B. (2011). Flow-types and lava emplacement history of Rajahmundry Traps, west of River Godavari, Andhra Pradesh. *Journal of the Geological Society of India*, *78*(5), 457–467. Retrieved from https://doi.org/10.1007/s12594-011-0111-7 doi: 10.1007/s12594-011-0111-7

Sepúlveda, J., Alegret, L., Thomas, E., Haddad, E., Cao, C., & Summons, R. E. (2019, 7). Stable Isotope Constraints on Marine Productivity Across the Cretaceous-Paleogene Mass Extinction. *Paleoceanography and Paleoclimatology*, *34*(7), 1195–1217. Retrieved from https://doi.org/10.1029/2018PA003442 doi: 10.1029/2018PA003442

Sial, A., Chen, J., Lacerda, L., Frei, R., Tewari, V., Pandit, M., ... Pereira, N. (2016). Mercury enrichments and Hg isotopes in Cretaceous–Paleogene boundary successions: Links to volcanism and palaeoenvironmental impacts. *Cretaceous Research*, *66*, 60–81. Retrieved from http://linkinghub.elsevier.com/retrieve/pii/S0195667116300969 doi: 10.1016/j.cretres.2016.05.006

Sinnesael, M., De Vleeschouwer, D., Coccioni, R., Claeys, P., Frontalini, F., Jovane, L., ... Montanari, A. (2016). High-resolution multiproxy cyclostratigraphic analysis of environmental and climatic events across the Cretaceous-Paleogene boundary in the classic pelagic succession of Gubbio (Italy). *Geological Society of America Special Papers*, *524*. doi: 10.1130/2016.2524(09)

Sinnesael, M., Montanari, A., Frontalini, F., Coccioni, R., Gattacceca, J., Snoeck, C., ... Claeys, P. (2019, 9). *Multiproxy Cretaceous-Paleogene boundary event stratigraphy: An Umbria-Marche basinwide perspective* (Vol. 542). Geological Society of America Special Paper. Re-

trieved from https://doi.org/10.1130/2019.2542(07) doi: 10.1130/2019.2542(07)

Smedley, M. P., Dawson, T. E., Comstock, J. P., Donovan, L. A., Sherrill, D. E., Cook, C. S., & Ehleringer, J. R. (1991, 6). Seasonal Carbon Isotope Discrimination in a Grassland Community. *Oecologia*, *85*(3), 314–320. Retrieved from http://www.jstor.org/stable/4219516

Smit, J. (1982). Extinction and evolution of planktonic foraminifera after a major impact at the Cretaceous/Tertiary boundary. In L. T. Silver & P. H. Schultz (Eds.), *Geological implications of impacts of large asteroids and comets on the earth* (Vol. 190, pp. 329–352). Geological Society of America Special Paper. doi: 10.1130/SPE190-p329

Smit, J., & Van Der Kaars, S. (1984). Terminal Cretaceous Extinctions in the Hell Creek Area, Montana: Compatible with Catastrophic Extinction. *Science*, *223*(4641), 1177–1179. Retrieved from http://www.jstor.org/stable/1692591

Smith, S. M., Sprain, C. J., Clemens, W. A., Lofgren, D. L., Renne, P. R., & Wilson, G. P. (2018, 6). Early mammalian recovery after the end-Cretaceous mass extinction: A high-resolution view from McGuire Creek area, Montana, USA. *Geological Society of America Bulletin*, *130*(11-12), 2000–2014. Retrieved from https://doi.org/10.1130/B31926.1 doi: 10.1130/B31926.1

Smith-Downey, N. V., Sunderland, E. M., & Jacob, D. J. (2010, 7). Anthropogenic impacts on global storage and emissions of mercury from terrestrial soils: Insights from a new global model. *Journal of Geophysical Research: Biogeosciences*, *115*(G3). Retrieved from https://doi.org/10.1029/2009JG001124 doi: 10.1029/2009JG001124

Spicer, R. A., & Collinson, M. E. (2014, 9). Plants and floral change at the Cretaceous-Paleogene boundary: Three decades on. In G. Keller & A. C. Kerr (Eds.), *Volcanism, impacts, and mass extinctions: Causes and effects* (Vol. 505, p. 0). Geological Society of America. Retrieved from https://doi.org/10.1130/2014.2505(05) doi: 10.1130/2014.2505(05)

Sprain, C. J., Renne, P. R., Clemens, W. A., & Wilson, G. P. (2018, 5). Calibration of chron C29r: New high-precision geochronologic and paleomagnetic constraints from the Hell Creek region, Montana. *Geological Society of America Bulletin*, *130*(9-10), 1615–1644. Retrieved from http://dx.doi.org/10.1130/B31890.1 doi: 10.1130/B31890.1

Sprain, C. J., Renne, P. R., Vanderkluysen, L., Pande, K., Self, S., & Mittal, T. (2019, 2). The eruptive tempo of Deccan volcanism in relation to the Cretaceous-Paleogene boundary. *Science*, *363*(6429), 866 LP - 870. Retrieved from http://science.sciencemag.org/content/363/6429/866.abstract doi: 10.1126/science.aav1446

Sprain, C. J., Renne, P. R., Wilson, G. P., & Clemens, W. A. (2015). High-resolution chronostratigraphy of the terrestrial Cretaceous-Paleogene transition and recovery interval in the Hell Creek region, Montana. *Bulletin of the Geological Society of America*, *127*(3-4), 393–409. doi: 10.1130/B31076.1

Steinthorsdottir, M., Vajda, V., & Pole, M. (2016). Global trends of pCO2 across the Cretaceous–Paleogene boundary supported by the first Southern Hemisphere stomatal proxy-based pCO2 reconstruction. *Palaeogeography, Palaeoclimatology, Palaeoecology*, *464*, 143–152. Retrieved from

http://www.sciencedirect.com/science/article/pii/S0031018216300967 doi: 10.1016/j.palaeo.2016.04.033

Stoenner, R. W., Schaeffer, O. A., & Katcoff, S. (1965, 6). Half-Lives of Argon-37, Argon-39, and Argon-42. *Science*, *148*(3675), 1325 LP - 1328. Retrieved from http://science.sciencemag.org/content/148/3675/1325.abstract doi: 10.1126/science.148.3675.1325

Subbarao, K. V., & Pathak, S. (1993). Reversely Magnetized Flows, Rajahmundry, Andhra Pradesh. *Journal of the Geological Society of India*, *41*(1), 71–72. Retrieved from http://www.geosocindia.org/index.php/jgsi/article/view/67197

Svensen, H., Planke, S., Polozov, A. G., Schmidbauer, N., Corfu, F., Podladchikov, Y. Y., & Jamtveit, B. (2009). Siberian gas venting and the end-Permian environmental crisis. *Earth and Planetary Science Letters*, *277*(3), 490–500. Retrieved from http://www.sciencedirect.com/science/article/pii/S0012821X08007292 doi: doi.org/10.1016/j.epsl.2008.11.015

Swart, P. K. (2015, 8). The geochemistry of carbonate diagenesis: The past, present and future. *Sedimentology*, *62*(5), 1233–1304. Retrieved from https://doi.org/10.1111/sed.12205 doi: 10.1111/sed.12205

Swisher III, C. C., Dingus, L., & Butler, R. F. (1993). 40Ar/39Ar dating and magnetostratigraphic correlation of the terrestrial Cretaceous–Paleogene boundary and Puercan Mammal Age, Hell Creek – Tullock formations, eastern Montana. *Canadian Journal of Earth Sciences*, *30*(9), 1981–1996. Retrieved from https://doi.org/10.1139/e93-174 doi: 10.1139/e93-174

Tauxe, L., Shaar, R., Jonestrask, L., Swanson-Hysell, N. L., Minnett, R., Koppers, A. A. P., ... Fairchild, L. (2016, 6). PmagPy: Software package for paleomagnetic data analysis and a bridge to the Magnetics Information Consortium (MagIC) Database. *Geochemistry, Geophysics, Geosystems*, *17*(6), 2450–2463. Retrieved from https://doi.org/10.1002/2016GC006307 doi: 10.1002/2016GC006307

Them, T. R., Jagoe, C. H., Caruthers, A. H., Gill, B. C., Grasby, S. E., Gröcke, D. R., ... Owens, J. D. (2019). Terrestrial sources as the primary delivery mechanism of mercury to the oceans across the Toarcian Oceanic Anoxic Event (Early Jurassic). *Earth and Planetary Science Letters*, *507*, 62–72. Retrieved from http://www.sciencedirect.com/science/article/pii/S0012821X18306885 doi: 10.1016/j.epsl.2018.11.029

Therrien, F., Eberth, D. A., Braman, D. R., & Zelenitsky, D. K. (2007, 4). High-resolution organic carbon isotope record across the Cretaceous–Tertiary boundary in south-central Alberta: implications for the post-impact recovery rate of terrestrial ecosystems and use of δ13C as a boundary marker. *Canadian Journal of Earth Sciences*, *44*(4), 529–542. Retrieved from https://doi.org/10.1139/e06-109 doi: 10.1139/e06-109

Thordarson, T., & Self, S. (1996). Sulfur, chlorine and fluorine degassing and atmospheric loading by the Roza eruption, Columbia River Basalt Group, Washington, USA. *Journal of Volcanology and Geothermal Research*, *74*(1), 49–73. Retrieved from http://www.sciencedirect.com/science/article/pii/S0377027396000546 doi: https://doi.org/10.1016/S0377-0273(96)00054-6

Tipple, B. J., Meyers, S. R., & Pagani, M. (2010, 9). Carbon isotope ratio of Cenozoic CO2: A comparative evaluation of available geochemical proxies. *Paleoceanography*, *25*(3). Retrieved from https://doi.org/10.1029/2009PA001851 doi: 10.1029/2009PA001851

Tobin, T. S., Bitz, C. M., & Archer, D. (2016). Modeling climatic effects of carbon dioxide emissions from Deccan Traps Volcanic Eruptions around the Cretaceous–Paleogene boundary. *Palaeogeography, Palaeoclimatology, Palaeoecology*. Retrieved from http://linkinghub.elsevier.com/retrieve/pii/S0031018216301778 doi: 10.1016/j.palaeo.2016.05.028

Tobin, T. S., Wilson, G. P., Eiler, J. M., & Hartman, J. H. (2014). Environmental change across a terrestrial Cretaceous-Paleogene boundary section in eastern Montana, USA, constrained by carbonate clumped isotope paleothermometry. *Geology*, *42*(4), 351–354. doi: 10.1130/G35262.1

Towles, N., Olson, P., & Gnanadesikan, A. (2015, 7). Scaling laws for perturbations in the ocean–atmosphere system following large CO2 emissions. *Climate of the Past*, *11*(7), 991–1007. Retrieved from https://www.clim-past.net/11/991/2015/ https://www.clim-past.net/11/991/2015/cp-11-991-2015.pdf doi: 10.5194/cp-11-991-2015

Tuszynski, J. (2012). caTools: Tools: moving window statistics, GIF, Base64, ROC AUC, etc. R package version 1.17. 1. *URL http://CRAN. R-project. org/package= caTools.[accessed 01 April 2014]*.

Vajda, V., & McLoughlin, S. (2004, 3). Fungal Proliferation at the Cretaceous-Tertiary Boundary. *Science*, *303*(5663), 1489 - 1489. Retrieved from http://science.sciencemag.org/content/303/5663/1489.abstract doi: 10.1126/science.1093807

Vandamme, D., & Courtillot, V. (1992). Paleomagnetic constraints on the structure of the Deccan traps. *Physics of the Earth and Planetary Interiors*, *74*(3), 241–261. Retrieved from http://www.sciencedirect.com/science/article/pii/003192019290013L doi: 10.1016/0031-9201(92)90013-L

Vanderkluysen, L., Mahoney, J. J., Hooper, P. R., Sheth, H. C., & Ray, R. (2011, 1). The Feeder System of the Deccan Traps (India): Insights from Dike Geochemistry. *Journal of Petrology*, *52*(2), 315–343. Retrieved from https://doi.org/10.1093/petrology/egq082 doi: 10.1093/petrology/egq082

Vellekoop, J., Sluijs, A., Smit, J., Schouten, S., Weijers, J. W. H., Sinninghe Damste, J. S., & Brinkhuis, H. (2014). Rapid short-term cooling following the Chicxulub impact at the Cretaceous-Paleogene boundary. *Proceedings of the National Academy of Sciences*, *111*(21), 7537–7541. Retrieved from http://www.pnas.org/cgi/doi/10.1073/pnas.1319253111 doi: 10.1073/pnas.1319253111

Vonhof, H. B., & Smit, J. (1997, 4). High-resolution late Maastrichtian–early Danian oceanic 87Sr/86Sr record: Implications for Cretaceous-Tertiary boundary events. *Geology*, *25*(4), 347–350. Retrieved from https://doi.org/10.1130/0091-7613(1997)025http://0.0.0.2 doi:

10.1130/0091-7613(1997)025<0347:HRLMED>2.3.CO;2

Vuorio, K., Meili, M., & Sarvala, J. (2006, 5). Taxon-specific variation in the stable isotopic signatures (δ13C and δ15N) of lake phytoplankton. *Freshwater Biology*, *51*(5), 807–822. Retrieved from https://doi.org/10.1111/j.1365-2427.2006.01529.x doi: 10.1111/j.1365-2427.2006.01529.x

Vye-Brown, C., Self, S., & Barry, T. L. (2013). Architecture and emplacement of flood basalt flow fields: case studies from the Columbia River Basalt Group, NW USA. *Bulletin of Volcanology*, *75*(3), 697. Retrieved from https://doi.org/10.1007/s00445-013-0697-2 doi: 10.1007/s00445-013-0697-2

Watson, G. S. (1956, 8). A Test for Randomness of Directions. *Geophysical Supplements to the monthly Notices of the Royal Astronomical Society*, *7*(4), 160–161. Retrieved from https://doi.org/10.1111/j.1365-246X.1956.tb05561.x doi: 10.1111/j.1365-246X.1956.tb05561.x

Widdowson, M., Walsh, J. N., & Subbarao, K. V. (1997, 1). The geochemistry of Indian bole horizons: palaeoenvironmental implications of Deccan intravolcanic palaeosurfaces. *Geological Society, London, Special Publications*, *120*(1), 269 LP - 281. Retrieved from http://sp.lyellcollection.org/content/120/1/269.abstract doi: 10.1144/GSL.SP.1997.120.01.17

Wilf, P., Johnson, K. R., & Huber, B. T. (2003, 1). Correlated terrestrial and marine evidence for global climate changes before mass extinction at the Cretaceous–Paleogene boundary. *Proceedings of the National Academy of Sciences*, *100*(2), 599 LP - 604. Retrieved from http://www.pnas.org/content/100/2/599.abstract

Wing, S. L., Alroy, J., & Hickey, L. J. (1995). Plant and mammal diversity in the Paleocene to early Eocene of the Bighorn Basin. *Palaeogeography, Palaeoclimatology, Palaeoecology*, *115*(1), 117–155. Retrieved from http://www.sciencedirect.com/science/article/pii/003101829400109L doi: 10.1016/0031-0182(94)00109-L

Witt, M. L. I., Fischer, T. P., Pyle, D. M., Yang, T. F., & Zellmer, G. F. (2008). Fumarole compositions and mercury emissions from the Tatun Volcanic Field, Taiwan: Results from multi-component gas analyser, portable mercury spectrometer and direct sampling techniques. *Journal of Volcanology and Geothermal Research*, *178*(4), 636–643. Retrieved from http://www.sciencedirect.com/science/article/pii/S0377027308003703 doi: https://doi.org/10.1016/j.jvolgeores.2008.06.035

Woelders, L., Vellekoop, J., Kroon, D., Smit, J., Casadío, S., Prámparo, M. B., ... Speijer, R. P. (2017, 5). Latest Cretaceous climatic and environmental change in the South Atlantic region. *Paleoceanography*, *32*(5), 466–483. Retrieved from https://doi.org/10.1002/2016PA003007 doi: 10.1002/2016PA003007

Wu, H., Zhang, S., Hinnov, L. A., Jiang, G., Yang, T., Li, H., ... Wang, C. (2014). Cyclostratigraphy and orbital tuning of the terrestrial upper Santonian–Lower Danian in Songliao Basin, northeastern China. *Earth and Planetary Science Letters*, *407*, 82–95. Retrieved from http://www.sciencedirect.com/science/article/pii/S0012821X14006013 doi: 10.1016/j.epsl.2014.09.038

Zachos, J. C., & Arthur, M. A. (1986). Paleoceanography of the Cretaceous/Tertiary boundary event: inferences from stable isotopic and other data. *Paleoceanography*, *1*(1), 5–26.

Zachos, J. C., Kroon, D., Blum, P., & Party, S. S. (2004). Leg 208, Site 1262 Initial Report. *Proceedings of the Ocean Drilling Program, Initial Rep*, *208*, 77–845.

Zeebe, R. E. (2012, 1). LOSCAR: Long-term Ocean-atmosphere-Sediment CArbon cycle Reservoir Model v2.0.4. *Geoscientific Model Development*, *5*(1), 149–166. Retrieved from https://www.geosci-model-dev.net/5/149/2012/ https://www.geosci-model-dev.net/5/149/2012/gmd-5-149-2012.pdf doi: 10.5194/gmd-5-149-2012

Zhang, J., Quay, P. D., & Wilbur, D. O. (1995). Carbon isotope fractionation during gas-water exchange and dissolution of CO2. *Geochimica et Cosmochimica Acta*, *59*(1), 107–114. Retrieved from http://www.sciencedirect.com/science/article/pii/001670379591550D doi: 10.1016/0016-7037(95)91550-D

Zhang, L., Wang, C., Wignall, P. B., Kluge, T., Wan, X., Wang, Q., & Gao, Y. (2018, 1). Deccan volcanism caused coupled pCO2 and terrestrial temperature rises, and pre-impact extinctions in northern China. *Geology*, *46*(3), 271–274. Retrieved from https://doi.org/10.1130/G39992.1 doi: 10.1130/G39992.1

Zhu, J., Poulsen, C. J., & Tierney, J. E. (2019, 9). Simulation of Eocene extreme warmth and high climate sensitivity through cloud feedbacks. *Science Advances*, *5*(9). Retrieved from http://advances.sciencemag.org/content/5/9/eaax1874.abstract doi: 10.1126/sciadv.aax1874